

# Advances in Coarse Discrete Particle Methods With Industrial Applications

**Liqiang Lu<sup>1</sup>, Sofiane Benyahia**

National Energy Technology Laboratory, Morgantown, WV, United States

<sup>1</sup>Corresponding author: e-mail address: liqiang.lu@netl.doe.gov

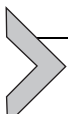
## Contents

1. Introduction	54
2. Description of Methods for Solving Fluid–Particle Flow	59
2.1 Computational Fluid Dynamics Coupled With Soft-Sphere Contact Model	60
2.2 Coarse-Grained Soft-Sphere Contact Model	69
2.3 Extension to Time-Driven Hard-Sphere Contact Model	80
3. Verification and Validation Studies	84
3.1 Verification Study of the Time-Driven Hard Sphere Model for Dense Granular Flow	85
3.2 Validation of Time-Driven Hard Sphere Model for Bubbling Fluidized Bed	89
3.3 Verification Study of Coarse-Grained Soft-Sphere and Hard-Sphere Contact Models	94
3.4 Validation of Heat Transfer in Coarse-Grained Soft-Sphere Contact Model	98
3.5 Validation of Coarse-Grained Hard-Sphere Model for Pilot-Scale CFB Riser	102
4. Application of Coarse-Grained Hard Sphere Method to Industrial Reactors	109
4.1 Simulation of a Fluidized Catalytic Cracking Regenerator	110
4.2 Simulation of a Methanol to Olefins Reactor	125
4.3 Simulation of a Rare Earth Elements Leaching Reactor	133
5. Concluding Remarks and Perspectives	143
Acknowledgments	148
Disclaimer	148
References	148

## Abstract

This chapter provides the full description of a coarse-grained discrete particle method based on a novel hard-sphere contact model for the simulation of industrial-scale fluidized bed reactors. This method is based on simple models that are easy to understand and implement in numerical codes. This technique is verified and validated for several small-scale fluidized systems where numerical data based on finer methods as well as experimental data are available. The speed of execution of this method is increased several orders of magnitudes compared to particle-based discrete methods, which allows

for thousands of seconds of flow, heat, and mass transfer simulations of industrial reactors such as fluidized catalytic cracking regenerator, Methanol to Olefins reactor, and Rare Earth Elements leaching reactor, achieved in just few days using commonly available computer resources. It is now possible for the common engineer to conduct simulations of large-scale fluid–particle reactors to understand, design, and troubleshoot, as well as optimize the performance of these complex multiphase flow systems.



## 1. INTRODUCTION

A look at the surface of Earth from space shows that it is mostly water, with dirt covering the rest of the planet if we ignore the presence of biomass. It is, therefore, evident that granular materials in all their shapes and sizes are the second most manipulated material in industry after water (Richard et al., 2005). In fact, industrial processes transform materials from their raw state to more useful and lucrative finished products. This is true not only today but also from the earliest of human civilizations. These civilizations are usually associated with our understanding of granular materials and their transformation from the Stone Age, where stone tools and weapons were made by our earliest ancestors, to early copper/bronze metallurgy, and finally to the Iron Age. Both early and current metallurgy is based on powdery ore. We, therefore, recognize that grinding is important in the processing of mining products not only because smaller powders are easier to handle and flow, but also because of the increased surface area that makes them more reactive when further chemical processing is required. Most industries, including the chemical, energy, and pharmaceutical industries, use powders at some stage of their processes. It is, therefore, important for the chemical engineer who is involved in designing and troubleshooting these plants to understand the flow of powders. The failure to thoroughly understand the behavior of solid particles in a process can lead to severe problems in start-up and unwanted downtime of solids processing plants. It is common in the literature to point to an early Rand corporation study (Merrow et al., 1981) that found the average performance of solids processing plants was only 49% of the targeted design capacity, while 84% was achieved by plants processing only gas or liquids. A more fundamental understanding of solids handling and processing is important to better design and operate these plants. This book chapter aims at providing a predictive method that is both efficient and reliable to help design and troubleshoot plants that use solid particles.

Industry usually manipulates solid powders physically and chemically in fluidized beds because the high heat and mass transfer rates they offer allow

for uniformity of temperature and products. A quote from an undergraduate chemical reactor engineering textbook perfectly summarized the high efficiency of fluidized beds: “the virtues of fluidized-bed reactor drove its competitors from the market” ([Fogler, 2009](#)). For this reason, industry has adopted the fluidized bed as the ideal fluid–solids contacting unit operation with many applications listed in the classic fluidization engineering textbook ([Kunii and Levenspiel, 1991](#)). Fluidization technology is not limited to these old applications. In fact, novel approaches to fluidization that use centrifugal force rather than just the force of gravity can open a whole new way of highly intensifying fluid–particle contacts that can occur in compact systems, which can save space and initial capital investment ([De Wilde et al., 2016](#)). Experimentally, the art of designing and scaling fluidized bed reactors is far from perfect because the hydrodynamics of fluidization change with both the system and particle sizes ([Knowlton et al., 2005](#)). This is true because of wall effects and the particle to bed diameter ratio must remain constant if all hydrodynamic scaling laws are to remain constant during scaling, which is impossible if reaction and heat transfer rates are to remain similar. Experimentation must, therefore, be augmented with mathematical modelling and numerical simulation based on computational fluid dynamics (CFD) to provide the designer with all available tools to be successful. The development and perfection of such tools, as well as their validation, are an ongoing effort. Based on this current effort, we hope that industrial practitioners contribute openly to the development and testing of new models and not be merely observers or critics of such a tremendous undertaking. This chapter offers a detailed description of a novel approach to model fluidized beds, which provides the practitioner with the ability to choose the speed and accuracy of their numerical simulation.

The continuum approach has traditionally been used to model most fluidized bed units from laboratory to industrial scales and is still currently used and actively developed by researchers and practitioners worldwide. The conservation equations of the flow of a continuum powder have been described first by Jackson’s group at Princeton University and summarized in his book ([Jackson, 2000](#)), while the first simulation of a fluidized bed is attributed to Gidaspow’s group at the Illinois Institute of Technology and described in his textbook on continuum kinetic theory description of fluidization ([Gidaspow, 1994](#)). It is known that powders are polydispersed in the sense that all their properties exhibit statistical distributions, such as size and density distributions. It is, therefore, difficult to find a powder with unique properties, such as size, density, or sphericity, to name just few physical properties. In some cases, a wide distribution of properties, such as particle

size, may be necessary to achieve the desired flow dynamics or catalytic performance of a fluidized bed reactor as explained in the literature (Grace and Sun, 1991). It is, therefore, logical to develop continuum models based on polydispersed granular kinetic theories (Garzó et al., 2007). These theories add a heavy burden on computational resources as well as a staggering level of complexity that is intimidating to most engineers. Numerical diffusion is another unwanted effect that plagues continuum theories mostly due to discretization of convective terms especially with first-order schemes (Syamlal and Benyahia, 2013). All these issues dissipate when we model powders as what they really are: discrete particles. The discrete description of granular material allows us with a single collision model to accurately predict all flow regimes from dilute particulate flows where collisions are scarce to a static pile of grains exhibiting enduring frictional contacts. The elegance of discrete element methods (usually abbreviated in the literature as DEMs) comes from the simplicity of the mathematical models and their coding in CFD. In fact, DEM is based on simple Newton's laws of motion where the acceleration of a solid body is due to forces acting on it. The formulation of contact forces between solid particles and with wall boundaries is based either on the soft-sphere model, where the overlap between particles is modeled by spring-dashpot system, or the hard-sphere model, which is based on conservation of linear and angular momentum before/after collision. As reported in the literature, further simplifications to DEM have been conducted by coarsening these models, thus lumping many real particles into computational parcels (Lu et al., 2016a; Patankar and Joseph, 2001). Other models, such as the multiphase particle-in-cell (MP-PIC), go further by ignoring the physics of discrete particle collision (Andrews and O'Rourke, 1996). The different assumptions in coarsening DEM will be explained in more detail in this chapter, which describes a coarse discrete particle method based on hard-sphere contact model.

Adopting a coarse-grained approach to conduct fluidized bed simulations increases the speed of DEM so that these predictive models can tackle large-scale reactors of interest to most industries. DEM tracks the trajectory of every particle in a system, usually a physical three-dimensional (3D) system, and their collisions with other particles and with physical boundaries, such as the walls of a reactor. The amount of particulate material in an industrial reactor is usually expressed in tons because counting the number of particles in such huge system is neither useful nor practical. Nevertheless, it is easy to estimate that number in the trillions, which contrasts with the millions of particles usually tracked in numerical simulations by

researchers in academia and industry (Xu et al., 2011). Results of one such simulation are presented in Fig. 1 showing the flow of particles in a vertical riser section of a circulating fluidized bed (CFB). The particles simulated here are polydispersed with a size ranging from about 50 to 100  $\mu\text{m}$  lifted in the riser by air at ambient conditions flowing at a superficial velocity of 1 m/s with a solids mass flux of 50  $\text{kg/m}^2 \text{s}$ . The system is hypothetical, i.e., does not exist physically, and consists of a cylinder of 0.02 m diameter and a height of 1 m with air and particles fed uniformly from the bottom and leaving freely from the open top of the riser—basically, a straight pipe without any complicated geometry. The CFD uses a uniform mesh consisting of 3.2 million cells to compute the flow of air with a particle count of about 100 million (the approximation is due to the transient nature of the flow in an open system with inlet/outlet). Fig. 1 shows a thin slice, from wall to wall, of a few particles deep in the middle of the riser. The vertical length

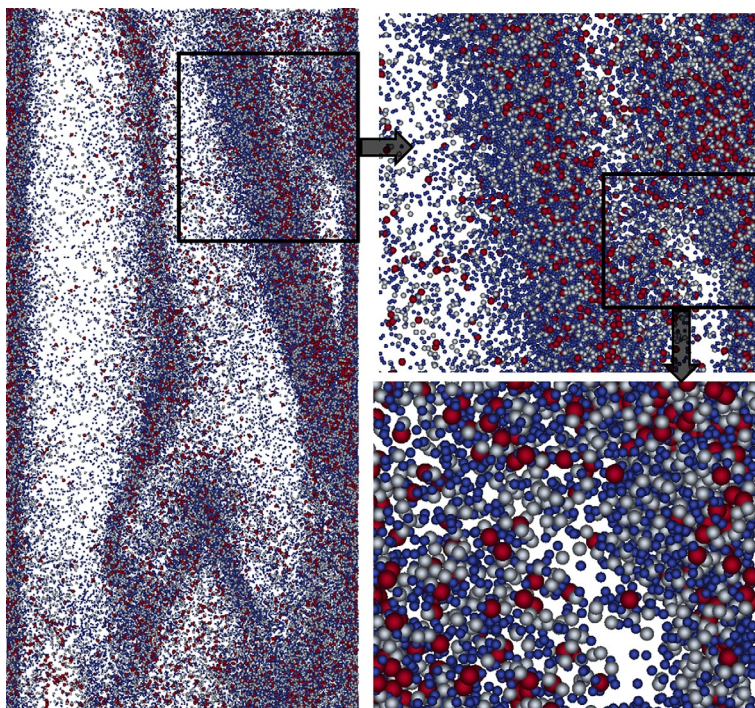


**Fig. 1** Instantaneous particle position colored by size in a thin slice of a 3D riser with two regions of interest zoomed to show flow structure details. The size of particles is to scale with respect to the riser geometry showing the full 0.02 m width of the riser and only twice that in length centered in the middle of the riser.

of this thin slice is about twice the diameter of the riser. It shows an instantaneous picture of the flow of particles in the middle section of the riser, and demonstrates, even in this small system, the existence of clusters of particles that flow downward slowly as observed experimentally (Shaffer et al., 2013), while a more dilute and fast upward flow of gas occurs at the core of the riser. This complex motion of particles can be observed in Video 1 in the online version at <https://doi.org/10.1016/bs.ache.2017.12.001> included in the supplemental material. The computation cost of conducting this numerical simulation on 256 processors is about 1 month of wall-clock time (the actual time we waited for the results) per second of simulated flow time. An industrial riser of 1 m diameter and 40 m height operating at the same condition will contain 0.1 million times more particles or 10 trillion particles. It is easy to imagine that the required resources to compute such industrial fluidized beds are prohibitive. The cost in time and resources required to conduct such simulations is a disincentive to most researchers and engineers.

The development of new predictive models requires some validation efforts to be conducted. Comparing computation results with experimental data can be fruitful to provide an idea of the predictive capabilities of the model but this is not sufficient to declare a model valid. In fact, a model is never fully valid or completely wrong. The idea is to evaluate how much uncertainty is due to major assumptions in developing any mathematical model to represent a physical reality. This physical reality is seldom well known and understood because the experimental measurements are also prone to uncertainties that can be significant. To evaluate such uncertainties, an interesting idea came from John Grace's research group at the University of British Columbia (UBC) where a "traveling" bubbling fluidized bed was designed and sent to several research groups who measured some quantities of interest under the same flow conditions for later comparing the different measurement techniques used by these research teams. The particle velocity measurements were published recently (Tebianian et al., 2016) and show some large quantitative differences even in the trends of the radial time-averaged profiles obtained with different measurement techniques (both intrusive and nonintrusive). It is clear from this sobering study that modelers who aim to obtain a perfect match with experimental data are doomed to fail. These interesting findings make it even more difficult to claim that a mathematical model that has been implemented in a CFD code is fully verified and validated (V&V). Needless to say, modelers overstepped by claiming some years back complete V&V of CFD codes, as pointed out by the same research group at UBC (Grace and Taghipour, 2004). The truth

is that both experimentalists and modelers are happy to obtain correct trends of flow quantities of interest. Significant efforts will be required to obtain quantitative assessments of errors in experimental measurements and numerical simulations of fluidized beds. Even then, those assessments may only be valid for the system studied under actual flow conditions. In our current approach of attempting to accelerate discrete particle models by adopting a coarse-grained approach, the model errors are usually assessed with respect to finer models that use fewer assumptions. We still make use of experimental data when available to compare the trends of those profiles with those obtained numerically. These comparisons are also useful to motivate industrial practitioners and engineers to adopt CFD as an important tool, among other tools, for designing and troubleshooting fluidized bed reactors.

This chapter provides the complete details of a novel coarse-grained DEM approach based on an improved time-driven hard-sphere method aimed at predicting flow dynamics in fluidized bed reactors cheaply yet accurately. The details of this approach will be described and compared with other methods available to the modelers. Some aspects of V&V of this method in our CFD open-source code will be addressed by simulating small-scale fluidized beds where previously published experimental measurements and/or detailed numerical simulation results are available, then moving to pilot-scale fluidized beds where experimental and simulation data are also available, and finally large-scale industrial reactors will be simulated and compared to published industrial data. This succession of simulations from small- to large-scale reactors is aimed at attracting the attention of modelers responsible for all design stages ranging from early reactor development to final industrial-scale reactor deployment. Thus, our main objective is to prove that CFD can be a reliable partner for the engineers and practitioners who aim at designing and troubleshooting fluidized bed systems. To fulfill this purpose, we hope to deliver a model that is not limited in range or scope but puts users in the driver's seat, relying only on users to make an informed decision on how to conduct their simulation to achieve the desired level of accuracy at an acceptable speed of execution.



## 2. DESCRIPTION OF METHODS FOR SOLVING FLUID–PARTICLE FLOW

Discrete particle simulations of fluidized beds can be traced back to the early 1990s with the pioneering work of [Tsuji et al. \(1993\)](#) using CFD–DEM, [Hoomans et al. \(1996\)](#) using the event-driven hard sphere

method (EDHS), and [Ouyang and Li \(1999\)](#) using the time-driven hard sphere model (TDHS). These methods avoid the continuum approach drawbacks by simply tracking the movement of individual particles and directly resolving particle–particle collisions. In CFD–DEM, the particles are assumed to be soft, and the collision is simulated by a linear spring-dashpot model. Note that in the general literature, the acronyms DEM and DPM are used interchangeably for all types of collision models, but it is reserved in this book chapter for soft-sphere collisions. This model is widely used because of its simplicity and capability to handle multibody collisions. However, it requires a much smaller time step to resolve particle–particle collisions. The EDHS handles particle–particle collisions using momentum conservation laws. This method is usually applied in dilute gas–solids flow where the mean free path between particle collisions is large. For dense phase flow, the collision frequency is much higher than that in dilute phase and the time interval between collisions is very small, rendering this method inefficient. The TDHS method solved this problem by allowing small overlaps between colliding particles; thus a larger time step can be used even for dense phase flows. However, TDHS still lacks the ability to handle multibody collisions and will result in unphysical overlaps for cases like particle packing. Lu et al. solved this problem by introducing a velocity correction term that aims to reduce the largest overlaps among colliding particles ([Lu et al., 2017d](#)). For industrial applications, computational parcels are simulated rather than real physical particles following a coarse-grained CFD–DEM or a coarse-grained hard sphere approach. These different approaches, along with MP-PIC, have been compared in recent research ([Lu et al., 2017a](#)). [Ge et al. \(2017\)](#) also reviewed fundamental developments and engineering applications of discrete particle simulations with a focus on multiscale structures. In this section, recent advances in these methods are summarized focusing on coarse-grained CFD–DEM and time-driven hard sphere methods.

## 2.1 Computational Fluid Dynamics Coupled With Soft-Sphere Contact Model

Pioneered by [Tsuji et al. \(1993\)](#) and [Xu and Yu \(1997\)](#), CFD–DEM has been widely used to investigate particle–fluid flows including hydrodynamics, heat transfer, and chemical reactions. The governing equations of this method are summarized in this section.

### 2.1.1 Fluid Dynamics

In CFD–DEM, the gas phase is governed by the traditional volume-averaged Navier–Stokes equations

$$\frac{\partial(\varepsilon_f \rho_f)}{\partial t} + (\nabla \cdot \varepsilon_f \rho_f \mathbf{u}_f) = 0 \quad (1)$$

$$\frac{D(\varepsilon_f \rho_f \mathbf{u}_f)}{Dt} = \nabla \cdot \bar{\bar{S}}_f + \varepsilon_f \rho_f \mathbf{g} - \mathbf{I} \quad (2)$$

where  $\varepsilon_f$  is the volume fraction of fluid,  $\rho_f$  is the density of the fluid,  $\mathbf{u}_f$  is the velocity of the fluid, and  $\mathbf{I}$  is the drag source term.  $\bar{\bar{S}}_f$  is the fluid phase stress tensor given by

$$\bar{\bar{S}}_f = -P_f \bar{I} + \bar{\tau}_f \quad (3)$$

where  $P_f$  is the fluid phase pressure and  $\bar{\tau}_f$  is the Newtonian fluid phase shear stress tensor

$$\bar{\tau}_f = 2\mu_f \bar{D}_f + \lambda_f \nabla \cdot \text{tr}(\bar{D}_f) \bar{I} \quad (4)$$

$$\bar{D}_f = \frac{1}{2} [\nabla \mathbf{u}_f + (\nabla \mathbf{u}_f)^T] \quad (5)$$

where  $\bar{D}_f$  is the strain rate tensor, and  $\mu_f$  and  $\lambda_f$  are the fluid dynamic and bulk viscosities.

The interphase momentum transfer term on fluid cell  $c$  can be calculated as

$$\mathbf{I}^c = \frac{1}{v_c} \sum_{i=1}^{N_p} \frac{1}{6} \pi d_p^3 \left( \nabla P_f(\mathbf{x}^i) + \frac{\beta^i}{1-\varepsilon_f} (\mathbf{v}_f(\mathbf{x}^i) - \mathbf{v}_p^i) \right) K(\mathbf{x}^i, \mathbf{x}_c) \quad (6)$$

where  $v_c$  is the volume of cell  $c$  and  $N_p$  is the number of particles influencing cell  $c$ .  $\beta^i$  is the drag coefficient of particle  $i$  in cell  $c$ .  $\mathbf{v}_f(\mathbf{x}^i)$  is the fluid velocity interpolated at particle  $i$  and  $K$  is the interpolation weight of particle  $i$  to cell  $c$ .

### 2.1.2 Momentum Transfer Models

The momentum exchange between the fluid phase and particles is expressed by different drag correlations. In fluidization, the motion of a particle is mainly driven by the fluid drag force countering a constant pull of the gravitational force. Thus, accurately calculating this drag force is critical to modelling the fluidization behavior. Currently, no general drag expression

can be used for all fluidization cases. The widely used drag models include empirically based models such as the Wen—Yu drag model (Wen and Yu, 1966), the Gidaspow drag model (Gidaspow, 1994), and the Syamlal—O’Brien drag model (Syamlal and O’Brien, 1987) which is based on a Richardson—Zaki type velocity—voidage correlation; drag models derived by fitting direct numerical simulation (DNS) data such as the Beetstra—Van der Hoef—Kuijpers (BVK) drag model (Beetstra et al., 2007) and the Hill—Koch—Ladd drag model (Benyahia et al., 2006); and finally drag models that include the effects of unresolved mesoscale structures such as the energy minimization multiscale (EMMS) drag model (Ge and Li, 2002; Li and Kwauk, 1994; Wang and Li, 2007; Wang et al., 2008; Yang et al., 2003) and the filtered drag model (Igci et al., 2008; Radl and Sundaresan, 2014). Due to the abundance of drag correlations derived in the literature, we will only express those used directly in this study. A full discussion on the specifics of each drag correlation and its applications falls, unfortunately, outside the scope of this work and will, thus, not be covered here. A brief discussion of some of these drag models and their different applications for discrete coarse-grained models was covered in our recent publication (Lu et al., 2017b), and the reader is encouraged to pursue different strategies to understand the profound effects these drag correlations can have on simulation results. Most of these drag correlations are based on standard drag coefficient for a single particle expressed as

$$C_{D0} = \begin{cases} \frac{24}{Re_p} \left( 1 + 0.15 Re_p^{0.687} \right) & Re_p < 1000 \\ 0.44 & Re_p \geq 1000 \end{cases} \quad (7)$$

where

$$Re_p = \frac{\epsilon_f \rho_f |\mathbf{v}_f - \mathbf{v}_p| d_p}{\mu_f} \quad (8)$$

For the Wen—Yu model, the drag coefficient is calculated as

$$\beta_{\text{Wen-Yu}} = \frac{3 \epsilon_f (1 - \epsilon_f) \rho_f |\mathbf{v}_f - \mathbf{v}_p|}{4 d_p} C_{D0} \epsilon_f^{-2.65} \quad (9)$$

For the Gidaspow model, the drag coefficient is calculated as

$$\beta_{\text{Gidaspow}} = \begin{cases} 150 \frac{(1 - \epsilon_f)^2 \mu_f}{\epsilon_f d_p^2} + 1.75 \frac{(1 - \epsilon_f) \rho_f |\mathbf{v}_f - \mathbf{v}_p|}{d_p}, & \epsilon_f \leq 0.8 \\ \frac{3 \epsilon_f (1 - \epsilon_f) \rho_f |\mathbf{v}_f - \mathbf{v}_p|}{4 d_p} C_{D0} \epsilon_f^{-2.65}, & \epsilon_f > 0.8 \end{cases} \quad (10)$$

For the Syamlal and O'Brien model, the drag coefficient is calculated as

$$\begin{aligned}\beta_{\text{Syamlal and O'Brien}} &= \frac{3 C_{\text{so}} \epsilon_f (1 - \epsilon_f) \rho_f}{4 d_p} |\mathbf{v}_f - \mathbf{v}_p| \\ C_{\text{so}} &= \left( \frac{0.63}{\nu_r} + \frac{4.8}{\sqrt{\nu_r Re_p}} \right)^2 \\ \nu_r &= 0.5 \left( A - 0.06 Re_p + \sqrt{(0.06 Re_p)^2 + 0.12 Re_p (2B - A) + A^2} \right) \quad (11) \\ A &= \epsilon_f^{4.14} \\ B &= \begin{cases} C_2 \epsilon_f^{1.28}, & \epsilon_f \leq 0.85 \\ \epsilon_f^{C_1}, & \epsilon_f > 0.85 \end{cases}\end{aligned}$$

For the BVK model, the drag coefficient is calculated as

$$\beta_{\text{BVK}} = \frac{18 \mu \epsilon_f (1 - \epsilon_f) F_{\text{BVK}}}{d_p^2} \quad (12)$$

$$\begin{aligned}F_{\text{BVK}} &= \frac{10(1 - \epsilon_f)}{\epsilon_f^2} + \epsilon_f^2 (1 + 1.5(1 - \epsilon_f)^{0.5}) \\ &\quad + \frac{0.413 Re_p}{24 \epsilon_f^2} \left[ \frac{\epsilon_f^{-1} + 3\epsilon_f(1 - \epsilon_f) + 8.4 Re_p^{-0.343}}{1 + 10^{3(1-\epsilon_f)} Re_p^{-0.5-2(1-\epsilon_f)}} \right] \quad (13)\end{aligned}$$

For the EMMS model, a heterogeneous factor is introduced to modify the Wen—Yu drag model. This factor is usually a function of voidage and slip velocity calculated in every computational cell. This function is based on gas density and viscosity, particle density and size, and operating conditions such as superficial velocity and bed size. In this chapter, the EMMS drag model is used in the simulation of a methanol to olefins (MTO) reactor (Tian et al., 2015) and is expressed as follows (Lu et al., 2016b):

$$\begin{aligned}\beta_{\text{EMMS}} &= \frac{3 \epsilon_f (1 - \epsilon_f) \rho_f}{4 d_p} |\mathbf{v}_f - \mathbf{v}_p| C_{D0} \epsilon_f^{-2.65} H_D \\ H_D &= \begin{cases} 0.1443 + \frac{1.6864}{1 + (\epsilon_f / 0.4064)^{20.4805}}, & \epsilon_f \leq 0.4924 \\ (-0.0999 + 0.9586 \epsilon_f)^{1.8008}, & 0.4924 < \epsilon_f \leq 0.9505 \\ (1649.4591 + 1648.5453 \epsilon_f)^{0.08597}, & 0.9505 < \epsilon_f \leq 1 \end{cases} \quad (14)\end{aligned}$$

The drag model for fluidized catalytic cracking (FCC) particles proposed by Gao et al. (2009) is used for the simulation of industrial FCC regenerators. This drag coefficient is expressed as

$$\beta_{\text{Gao}} = \begin{cases} 150 \frac{(1 - \varepsilon_f)^2 \mu_f}{\varepsilon_f d_p^2} + 1.75 \frac{(1 - \varepsilon_f) \rho_f |\mathbf{v}_f - \mathbf{v}_p|}{d_p}, & \varepsilon_f \leq 0.800 \\ \frac{5}{72} \frac{\varepsilon_f (1 - \varepsilon_f) \rho_f |\mathbf{v}_f - \mathbf{v}_p|}{d_p (1 - \varepsilon_f)^{0.293}} C_{D^*}, & 0.800 < \varepsilon_f \leq 0.933 \\ \frac{3}{4} \frac{\varepsilon_f (1 - \varepsilon_f) \rho_f |\mathbf{v}_f - \mathbf{v}_p|}{d_p} C_{D0} \varepsilon_f^{-2.65}, & 0.933 < \varepsilon_f \leq 0.990 \\ \frac{3}{4} \frac{\varepsilon_f (1 - \varepsilon_f) \rho_f |\mathbf{v}_f - \mathbf{v}_p|}{d_p} C_{D0}, & 0.990 < \varepsilon_f \leq 1.000 \end{cases} \quad (15)$$

where

$$C_{D^*} = \begin{cases} \frac{24}{Re_{p^*}} (1 + 0.15 Re_{p^*}^{0.687}) & Re_{p^*} < 1000 \\ 0.44 & Re_{p^*} \geq 1000 \end{cases} \quad (16)$$

$$Re_{p^*} = \frac{\varepsilon_f \rho_f |\mathbf{v}_f - \mathbf{v}_p| d_{p^*}}{\mu_f} \quad (17)$$

### 2.1.3 Solid Particle Dynamics

The Lagrangian method is used to track the motion of particles. For each solids particle, the momentum equation takes the familiar form of Newton's law of motion

$$m_p \frac{d\mathbf{v}_p}{dt} = m_p \mathbf{g} - \frac{\pi}{6} d_p^3 \nabla P_f + \frac{\beta(\mathbf{v}_f(\mathbf{x}^i) - \mathbf{v}_p)}{1 - \varepsilon_f} \frac{\pi}{6} d_p^3 + \mathbf{F}_c \quad (18)$$

$$I \frac{d\mathbf{w}_p}{dt} = \mathbf{T} \quad (19)$$

where  $m_p$  is the mass of the particle and  $d_p$  its diameter.  $\mathbf{v}_p$  is translation velocity of particle and  $\mathbf{w}_p$  is its angular velocity. The moment of inertia  $I$  is calculated by  $m_p d_p^2 / 10$ . On the right-hand side, the forces considered include the gravity force, pressure gradient force, drag force, and the contact force ( $\mathbf{F}_c$ ). The contact force is calculated by the DEM in normal ( $\mathbf{F}^n$ ) and tangential ( $\mathbf{F}^t$ ) directions and is described below.

The normal contact force acting on particle  $i$  due to its collision with particle  $j$  is calculated as

$$\mathbf{F}_{ij}^n = (-k_n \delta_n + \eta_n \dot{\delta}_n) \mathbf{n}_{ij} \quad (20)$$

where  $k_n$  is the spring stiffness,  $\delta_n$  is the thickness of the overlapped region, and the dot represents time derivative,  $\mathbf{n}_{ij}$  is a unit vector along the line of centers from  $j$  to  $i$ , and  $\eta_n$  is the damping coefficient defined as

$$\eta_n = \sqrt{2k_n m_p} \frac{\ln(1/e_p)}{\sqrt{\pi^2 + [\ln(1/e_p)]^2}} \quad (21)$$

where  $e_p$  denotes the restitution coefficient.

The tangential contact force is calculated similarly to the normal forces as

$$\mathbf{F}_{ij}^t = (-k_t \delta_t + v_t \dot{\delta}_t) \mathbf{t}_{ij} \quad (22)$$

where  $\delta_t$  is the tangential displacement. It is caused by the relative movement of colliding particles in tangential direction  $\mathbf{t}_{ij}$ , which can be calculated as

$$\mathbf{t}_{ij} = \frac{\mathbf{v}_{t,ij}}{|\mathbf{v}_{t,ij}|} \quad (23)$$

Where  $\mathbf{v}_{t,ij}$  is the tangential relative velocity. It can be calculated as

$$\mathbf{v}_{t,ij} = (\mathbf{v}_i - \mathbf{v}_j) - (\mathbf{v}_i - \mathbf{v}_j) \cdot \mathbf{n}_{ij} \mathbf{n}_{ij} \quad (24)$$

The tangential force is also limited by the finite Coulomb friction between colliding particles with a sliding friction coefficient of  $\mu$ . Thus, it is defined as

$$\mathbf{F}_{ij}^t = \min(\mathbf{F}_{ij}^t, \mu \mathbf{F}_{ij}^n) \quad (25)$$

Finally, the collision force on the tracked  $i$  particle is

$$\mathbf{F}_c = \sum_{j=1, j \neq i}^N (\mathbf{F}_{ij}^n + \mathbf{F}_{ij}^t) \quad (26)$$

As for particle rotation, the torque on each tracked  $i$  particle is calculated as

$$\mathbf{T} = \sum_{j=1, j \neq i}^N (L \mathbf{n} \times \mathbf{F}_{ij}^t) \quad (27)$$

where  $L$  is the distance from particle center to contact point.

### 2.1.4 Heat Transfer Model

Generally, the heat transfer mechanisms include convection, conduction, and radiation. In fluidized beds, the main heat transfer mechanisms for particles include particle–fluid convection, particle–fluid–particle conduction, particle–fluid–wall conduction, particle–particle contact conduction, and particle–wall contact conduction. Radiative heat transfer is not treated here because it is not of interest to this research and is, thus, deferred for future development. Thus, the conservation equation for heat transfer of particle  $i$  can be written as

$$m_i c_{p,i} \frac{dT_i}{dt} = Q_{i,\text{conv}} + Q_{i,w} + \sum_{j=1}^{K_i} Q_{i,j} \quad (28)$$

Where  $Q_{i,\text{conv}}$  is particle–fluid convection.  $Q_{i,w}$  is particle–wall conduction, which includes particle–fluid–wall conduction and particle–wall contact conduction.  $Q_{i,j}$  is particle–particle conduction, which includes particle–fluid–particle conduction and particle–particle contact conduction.

The particle–fluid convection is proportional to temperature difference, surface area, and the convective heat transfer coefficient. This convection is calculated by

$$Q_{i,\text{conv}} = h_{i,\text{conv}} \pi d_p^2 (T_f - T_i) \quad (29)$$

where the convective heat transfer coefficient  $h_{i,\text{conv}}$  is a function of the particle Nusselt number, and the correlation given by [Gunn \(1978\)](#) is used

$$\begin{aligned} Nu_i &= (7 - 10\epsilon_f + 5\epsilon_f^2)(1.0 + 0.7 Re_i^{0.2} Pr^{0.33}) \\ &+ (1.33 - 2.4\epsilon_f + 1.2\epsilon_f^2) Re_i^{0.7} Pr^{0.33} \end{aligned} \quad (30)$$

$$Nu_i = \frac{h_{i,\text{conv}} d_p}{k_f}, \quad Pr_i = \frac{\mu_f C_f}{k_f} \quad (31)$$

where  $d_p$  and  $k_f$  are the particle diameter and fluid thermal conductivity.  $Re_i$  is the local Reynolds number of particle  $i$ .  $C_f$  is the specific heat of fluid.

As shown in the following equation, particle–wall conduction includes particle–fluid–wall conduction and particle–wall collision conduction.

$$Q_{i,w} = Q_{i,w}^{\text{pfw}} + Q_{i,w}^{\text{pwc}} \quad (32)$$

For particle–fluid–wall conduction, the model introduced by [Rong and Horio \(1999\)](#) is used in this research, as shown in [Fig. 2](#). They hypothesize that each particle is surrounded by a gas layer with a constant thickness,  $\eta_{\text{len}}$ ; particle–fluid–wall heat transfer initiates when the gas layer intersects

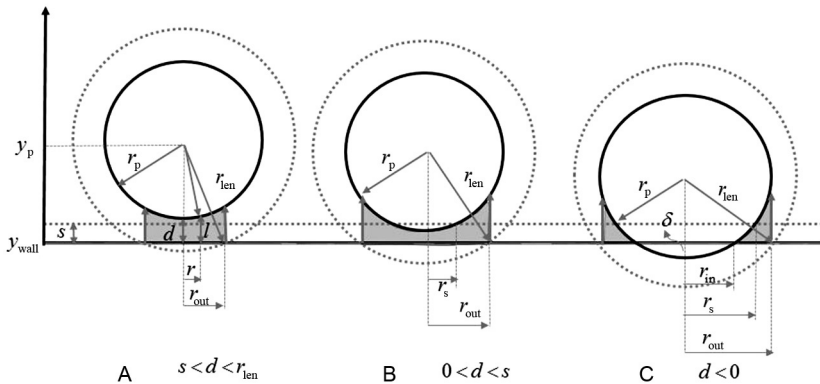


**Fig. 2** Particle–fluid–wall heat transfer model. From (A) to (C), the particle is getting closer to the wall. In case (A) only the gas layer contacts the wall and the distance is larger than  $s$ ; in case (B) the distance is smaller than  $s$ ; in case (C) the particle is in contact with wall. Modified from Lu L, Morris A, Li T, Benyahia S: Extension of a coarse grained particle method to simulate heat transfer in fluidized beds. Int J Heat Mass Transf 111:723–735, 2017c with permission for the reprinted content. Copyright (2017) Elsevier.

with the wall; heat transfer occurs across paths parallel to the axis joining the particle’s center and the wall; a uniform gas layer, with a constant thickness,  $s$ , separates the particle and the wall; the temperature is assumed to be uniform inside a particle. Thus, this term can be calculated as

$$Q_{i,w}^{\text{pfw}} = 2\pi k_g (T_w - T_i) \int_{r_{in}}^{r_{out}} \frac{r}{l} dr \quad (33)$$

where  $k_g$  is the gas thermal conductive coefficient,  $T_w$  and  $T_i$  are the temperatures of wall and particle,  $l$  is the distance between particle and wall, and the integration from  $r_{in}$  to  $r_{out}$  delineates the region of particle–fluid–wall conduction.

For the particle–wall contact conduction term, the model proposed by Batchelor and Brien (1977) is adopted here. When a particle contacts the wall, the conduction heat transfer can be calculated as

$$Q_{i,w}^{\text{pwc}} = \frac{4r_c(T_w - T_i)}{(1/k_{pi} + 1/k_w)} \quad (34)$$

where  $r_c$  is the contact radius,  $k_{pi}$  and  $k_w$  are thermal conductive coefficients of the particle and the wall,  $T_w$  and  $T_i$  are the temperatures of the wall and the particle, and  $r_c$  can be calculated by the following equation:

$$r_c = \sqrt{r_p^2 - (r_p - \delta)^2} = \sqrt{2r_p\delta - \delta^2} \quad (35)$$

Finally, for the fluid phase, the conservation equation of thermal energy is expressed as

$$\varepsilon_f \rho_f C_{pf} \left( \frac{\partial T_f}{\partial t} + \mathbf{u}_f \cdot \nabla T_f \right) = -\nabla \cdot \vec{q}_f + S_{pf} + S \quad (36)$$

where  $S_{pf}$  is the total heat transfer from solid particles and  $S$  is any other source terms, such as heat generated or consumed due to chemical reactions. The conductive heat flux is described by Fourier's law

$$\vec{q}_f = -\varepsilon_f k_f \nabla T_f \quad (37)$$

$$S_{pf} = -\frac{1}{V_{cell}} \sum_{i=1}^{N_p} Q_{i,\text{conv}} \quad (38)$$

### 2.1.5 Species Transport With Chemical Reactions

For Euler–Lagrange simulations, heterogeneous chemical reactions can be simulated with particle-scale chemical reaction kinetic models, such as the shrinking core model, where the reaction rate is a function of the particle diameter. In MFIX-DEM, all chemical reaction rates are defined by the user through the modification of a file named `usr_des_rrates.f`. In the discrete particle model, the mass, density, species fraction, and radius of each particle are tracked. The particle's mass variation due to chemical reaction is given by

$$\frac{dm_p}{dt} = \sum_{n=1}^{N_s} R_{sn} \quad (39)$$

where  $R_{sn}$  is the rate of production (or consumption) of species  $n$  in this particle and  $N_s$  is the number of species.  $m_p$  is the particle mass and it equals:

$$m_p = \sum_{n=1}^{N_s} X_{pn} m_p \quad (40)$$

The mass variation of species  $n$  due to chemical reaction is given by

$$\frac{d(X_{pn} m_p)}{dt} = R_{sn} \quad (41)$$

Using the product rule and Eq. (40), the mass fraction of species  $n$  in this particle ( $X_{pn}$ ) can be further expressed as

$$\frac{dX_{pn}}{dt} = \frac{1}{m_p} \left( R_{sn} - X_{pn} \sum_{n=1}^{N_s} R_{sn} \right) \quad (42)$$

Since the mass of particles changes due to chemical reactions, either the density or the diameter of this particle should be modified. If the density of the particle is assumed to be constant by the user, then the diameter of the particle is recalculated according to

$$d_p = \left( \frac{6m_p}{\pi\rho_p} \right)^{1/3} \quad (43)$$

On the other hand, if the particle diameter is assumed to be constant, then the density of the particle is recalculated according to

$$\rho_p = \frac{6m_p}{\pi d_p^3} \quad (44)$$

For species fraction in the fluid phase, the following continuum transport equation is solved:

$$\frac{\partial(\varepsilon_f \rho_f X_n)}{\partial t} + \nabla \cdot (\varepsilon_f \rho_f \mathbf{u}_f X_n) = \nabla \cdot (D_n \nabla X_n) + R_{fn} \quad (45)$$

where  $X_n$  is the mass fraction of fluid species  $n$ ,  $D_n$  its diffusion coefficient, and  $R_{fn}$  is the mass transfer of species  $n$  between the particles and the fluid phase, and is calculated as

$$R_{fn} = \frac{1}{V_{cell}} \sum_{i=1}^{N_k} R_{fn}^i \quad (46)$$

where  $V_{cell}$  is the volume of a CFD cell,  $N_k$  is the number of particles in this cell,  $R_{fn}^i$  is the rate of fluid phase species production (or consumption) due to heterogeneous reactions occurring between particle  $i$  and the fluid phase.

## 2.2 Coarse-Grained Soft-Sphere Contact Model

To reduce computation costs, as discussed in the introduction, the combination of the CFD–DEM method with the parcel-based method results in the coarse-grained CFD–DEM. Only computational spheres, or parcels, are tracked because all particles within a parcel follow the exact same trajectory and have identical properties that may change in time due to heat/mass transfer. [Sakano et al. \(2000\)](#) simulated a bubbling fluidized bed in which many physical particles are lumped into a computational sphere, and obtained good agreement of bubble diameters by assuming that the particles in the computational parcel are in a face-centered cubic arrangement.

Around the same time, [Patankar and Joseph \(2001\)](#) investigated the accuracy of the parcel-based method by simulating a simple sedimentation case, a gas–solids bubbling fluidized bed, and a liquid–solids fluidized bed. The predicted sedimentation results compared well with experimental data, and for bubbling fluidized bed a similar bubbling pattern is observed when using two different parcel sizes. These pioneering studies gained the attention of researchers because increasing computer speeds allows this technique to be used to investigate pilot and even industrial-scale reactors. In this section, the basic assumptions and governing equations of coarse-grained CFD–DEM are summarized, followed by discussion of recent advances in this area and extension to heat transfer.

### **2.2.1 Basic Assumptions in Coarse-Grained Soft-Sphere Contact Model**

In the coarse-grained CFD–DEM model, the averaged Navier–Stokes equations for the continuum fluid phase are solved in the same way as in traditional CFD–DEM with the notable exception that the interphase momentum ( $\mathbf{T}^{CG}$ ), heat ( $S^{CG}$ ), and mass transfers ( $R^{CG}$ ) are recalculated based on the number of real particles in a computational parcel. [Fig. 3](#) shows some basic assumptions in coarse-grained CFD–DEM where the main idea behind coarse graining is the lumping of real particles into a coarse-grained or computational parcel (CGP). The number of real particles in a CGP is represented by a statistic weight  $W$ . In this figure, we take a computational cell in an original system (physical system made of real particles) as an example to explain the assumptions and calculation method for drag force (a), heat transfer (b), chemical reactions (c), collision forces (d), and collision torques (e).

For coarse-grained CFD–DEM the fluid phase is resolved at grid scale, while the solids phase is resolved at parcel scale in the same way as in traditional CFD–DEM. All the particles in a computational cell share the same (or similar if using interpolated values) voidage, fluid velocity, temperature, and species fractions. The first major assumption in coarse-grained CFD–DEM is that all the real particles in a CGP are subjected to the same drag force. The error in this assumption is related to the number of real particles in the parcel, and to the gradient of Eulerian field values such as voidage and fluid velocity. This means that for a homogeneous flow, a much larger  $W$  (recall that  $W$  stands for number of real particles in a CGP) can be used, while for heterogeneous flows characterized by bubbles and clusters, either a smaller  $W$  or further corrections to drag force should be used. According

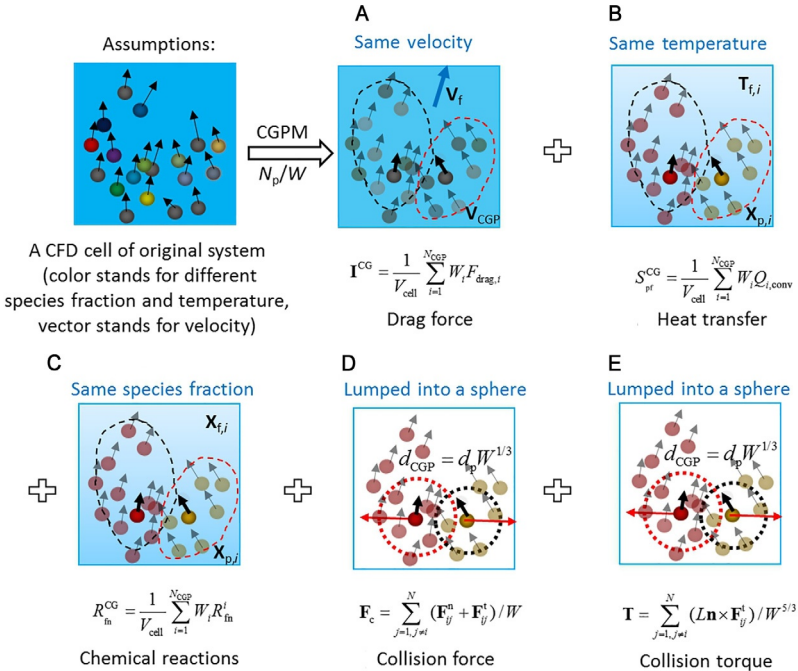


**Fig. 3** Basic assumptions in coarse-grained CFD-DEM.  $N_p$  stands for number of real particles in original system,  $W$  is the statistic weight stands for number of real particles in a coarse-grained particle,  $N_{\text{CGP}}$  is number of coarse-grained particles.

to this assumption, the momentum exchange between parcels and the fluid phase is calculated as

$$\mathbf{I}^{\text{CG}} = \frac{1}{V_{\text{cell}}} \sum_{i=1}^{N_{\text{CGP}}} W_i F_{\text{drag},i} \quad (47)$$

The second assumption in coarse-grained CFD-DEM is that all the real particles in a CGP have the same temperature. The error in this assumption is very small if the dominating heat transfer mechanism is fluid-particle convection, which is a reasonable assumption because fluidized beds are highly efficient in convecting heat since temperature gradients in the fluid phase are usually very small. Thus, the heat transfer between fluid phase and parcels is calculated as

$$S_{\text{pf}}^{\text{CG}} = \frac{1}{V_{\text{cell}}} \sum_{i=1}^{N_{\text{CGP}}} W_i Q_{i,\text{conv}} \quad (48)$$

The third assumption in coarse-grained CFD-DEM is that all the real particles in a CGP have the same species mass fractions. The error in this

assumption is similar to the previous two assumptions since species transport occurs in a similar manner as heat and momentum transport. Thus, the mass transfer between fluid and parcels is calculated as

$$R_{\text{fn}}^{\text{CG}} = \frac{1}{V_{\text{cell}}} \sum_{i=1}^{N_{\text{CGP}}} W_i R_{\text{fn}}^i \quad (49)$$

The fourth assumption in coarse-grained CFD–DEM is that all real particles in a CGP are subjected to the same collision force. This is a major assumption since the collision between particles inside the CGPs is skipped. To calculate the collision force, an imaginary sphere of same density as real particles is constructed, the diameter of which can be calculated as

$$d_{\text{CGP}} = d_p W^{1/3} \quad (50)$$

Then, the collision force on the parcels is calculated the same as in DEM and divided by statistic weight to obtain the collision force acting on a single particle in the parcel.

$$\mathbf{F}_c = \sum_{j=1, j \neq i}^{N_{\text{CGP}}} \left( \mathbf{F}_{ij}^n + \mathbf{F}_{ij}^t \right) / W \quad (51)$$

The fifth assumption in coarse-grained CFD–DEM is that all real particles in a CGP are subjected to the same collision torque. This follows the fourth assumption exactly, and the corresponding torque is calculated as

$$\mathbf{T} = \sum_{j=1, j \neq i}^{N_{\text{CGP}}} \left( L \mathbf{n} \times \mathbf{F}_{ij}^t \right) / W^{5/3} \quad (52)$$

### **2.2.2 Recent Advances in Coarse-Grained Soft-Sphere Contact Model**

Apart from the five basic assumptions expressed in the above section, there are two important considerations for coarse-grained CFD–DEM simulation: the size and collision parameters of CGP.

The selection of a parcel size is important because it determines the simulation performances in terms of accuracy and speed. The speed of a simulation is affected by computational resources that can be dedicated to an application. Some researchers in academia may be able to wait for months for simulation results, while an industrial researcher may require faster results. The accuracy of a simulation is affected by the ratio of parcel size to particle diameter. When this ratio is equal to unity, the simulation

becomes DEM-based achieving results that are of the highest possible accuracy. As this ratio increases, the speed of the simulation increases drastically but its accuracy deteriorates. Apart from an increase in speed, general criteria for selecting a value for this size ratio is not yet available. However, for systems with distinct mesoscale structures, like bubbles and clusters, the parcel size should be small enough to resolve the deformation, aggregation, and breakage of bubbles or clusters (Lu et al., 2014, 2017b). The size of bubbles and clusters can be estimated from empirical corrections or the EMMS model (Lu et al., 2014; Shi et al., 2011; Wang et al., 2008). To quantify model uncertainties due to coarsening of particles, the most accurate solution is first sought, then the uncertainty is easily determined by comparison. As an example, in two-fluid models (TFM) where the solids phase is treated as a continuum, the most accurate simulation results are obtained for a grid-independent solution. For the coarse-grained method, a “grid-independent” solution corresponds to a DEM solution where the computational parcel size is reduced to that of an individual physical particle. In small fluidized beds where the number of particles is not excessive, it is possible to quantify exactly the uncertainty associated with coarse graining. However, in large or industrial fluidized beds where the particles are quantified in tons rather than numbers, it is currently impossible to conduct DEM simulations to obtain a grid-independent solution. In this case, we propose to quantify uncertainties in fluidized beds of smaller scales, then extrapolate to larger systems to estimate the errors associated with coarsening. Such a detailed study is yet to be conducted and is left for future work. We anticipate that these errors will depend on the physics driving a particular system: for particle-particle dominated interactions (such as dense granular flows) the errors may be large, while these errors are expected to be smaller for cases where the fluid-particle drag force is dominant. In summary, the size of CGP should be larger than the particle diameter and smaller than the minimum grid-scale structures like CFD cell size, bubble size, and cluster size (Lu et al., 2014).

$$d_p \leq d_{\text{CGP}} \leq \min(d_{\text{cl,min}}, d_{\text{b,min}}, d_{\text{cell,min}}) \quad (53)$$

The collision parameters of CGP directly influence the particle-particle and particle-wall collision forces and can influence the simulation accuracy, especially in dense phase flow where collision is the dominate mechanism for particle transport. In linear spring-dashpot force model, the main collision parameters include spring constant, restitution coefficient, and friction coefficient. The same values for these three parameters were used in the

pioneering work of [Sakano et al. \(2000\)](#), and also by [Patankar and Joseph \(2001\)](#). Recently, different researchers developed a variety of scaling laws to scale these parameters from particle to parcel size based on different criteria.

[Sakai and Koshizuka \(2009\)](#) assumed the overlap and collision force between colliding parcels and the original particles to be the same. This implies that when two CGPs collide, all the real particles in one CGP are subject to binary collisions with the particles from the other colliding CGP. Thus, the spring coefficient and damping coefficient must be scaled by  $W$  times in this model. Since the friction coefficient is directly related to the repose angle, the same value is used for CGP. Thus, the three parameters are scaled according to

$$k_{n,CGP} = W k_{n,p} \quad (54)$$

$$e_{CGP} = e_p \quad (55)$$

$$\mu_{CGP} = \mu_p \quad (56)$$

[Benyahia and Galvin \(2010\)](#) estimated the errors of this method for shear flow, bubbling fluidized bed, and vertical riser flow. They proposed a modification to the restitution coefficient based on the fact that collisions between particles within the parcel are ignored. The restitution coefficient is modified as

$$\frac{\ln(e_{CGP})}{\ln(e_p)} = \sqrt{W} \quad (57)$$

[Radl et al. \(2011\)](#) proposed a different scaling law based on equal energy densities in the original and the coarse-grained system. This means that the density of the particles, as well as the translational velocity must be invariant. From the dimensionless form of the mass-spring-dashpot equation, they derived that the spring constant should be scaled by  $W^{1/3}$  times. [Thakur et al. \(2016\)](#) also validated this relationship by simulating the loading process in a frictionless granular system. This proposed scaling law is written as

$$k_{n,CGP} = W^{1/3} k_{n,p} \quad (58)$$

$$e_{CGP} = e_p \quad (59)$$

$$\mu_{CGP} = \mu_p \quad (60)$$

[Lu et al. \(2014\)](#) and [Lu et al. \(2016c\)](#) proposed a coarse-grained CFD–DEM model along with EMMS-DPM. In this method, the local EMMS

model (Wang and Li, 2007) is first used to calculate the distribution of cluster size or bubble sizes in the fluidized bed. Then, the parcel size is set to be smaller than most of the clusters or bubbles, and the CFD grid size is set to be 2–5 times the parcel size. Since there can be hundreds or thousands of real particles in a computational parcel, the EMMS drag model is also used to calculate drag forces. The process of lumping particles together reduces the collision frequency, which directly influences the energy dissipation. To account for this error, an effective restitution coefficient was proposed, based on kinetic theory of granular flow, by assuming the energy dissipation during collisions for the original system and the coarse-grained system are identical. They also found that the spring stiffness has little influence on simulation results of the CFB riser. Finally, in their model, these three parameters are scaled as

$$k_{n,CGP} = k_{n,p} \quad (61)$$

$$e_{CGP} = \sqrt{1 + (e_p^2 - 1) W^{1/3}} \quad (62)$$

$$\mu_{CGP} = \mu_p \quad (63)$$

They simulated a bubbling fluidized bed, a CFB riser, and the full loop of a CFB. The simulated bed height, pressure drop profile, solid velocity profile, and solid volume fractions compared well with experiment data and DEM results.

### 2.2.3 Extension to Heat Transfer

Convective heat transfer between particles/parcels and the fluid, the details of which were previously explained, is the most important mechanism of heat transfer in fluidized bed systems. For general multiphase flows, however, particle–fluid–wall heat conduction can also play an important role if the walls of the reactor possess high heat transfer efficiency such as a stirred tank with a cooling jacket. In coarse-grained CFD–DEM, the collision between particle and wall is calculated using  $d_{CGP}$  as the collision diameter, and the parcel to wall distance  $l$  will be different from the original system when a parcel collides with the wall. To ensure the particle–fluid–wall heat transfer is identical between the CGP system and the original system, a nondimensional form of particle–fluid–wall heat transfer for CGP is derived using particle diameter as the reference length (Lu et al., 2017c)

$$\overline{Q}_{i,w}^{\text{pfw}} = \frac{Q_{i,w}^{\text{pfw}}}{2\pi k_g (T_w - T_i) r_p} = \int_{r_{in}}^{\bar{r}_{out}} \frac{\bar{r}}{\bar{l}} d\bar{r} \quad (64)$$

The distance  $l$  will decrease as the particle moves closer to the wall, and when the particle is in contact with the wall, or  $l=0$ , a singularity will appear in this equation. This singularity is solved by assuming a minimum distance,  $s$ , between particle and wall. Thus, the integral can be converted to three nonsingular functions according to the particle–wall distance

$$\overline{Q}_{i,w}^{\text{pfw}} = \int_{\bar{r}_{in}}^{\bar{r}_{out}} \frac{\bar{r}}{\bar{l}} d\bar{r} = \begin{cases} \int_0^{\bar{r}_{out}} \frac{\bar{r}}{\bar{l}} d\bar{r} & \bar{s} < \bar{d} < \bar{r}_{len} \\ \int_0^{\bar{r}_s} \frac{\bar{r}}{\bar{s}} d\bar{r} + \int_{\bar{r}_{in}}^{\bar{r}_{out}} \frac{\bar{r}}{\bar{l}} d\bar{r} & 0 < \bar{d} < \bar{s} \\ \int_{\bar{r}_s}^{\bar{r}_{out}} \frac{\bar{r}}{\bar{s}} d\bar{r} + \int_{\bar{r}_s}^{\bar{r}_{out}} \frac{\bar{r}}{\bar{l}} d\bar{r} & \bar{d} < 0 \end{cases} \quad (65)$$

For brevity, the integration results and the geometrical relationships among  $r_s$ ,  $r_{in}$ ,  $r_{out}$ ,  $l$ , and  $r$  are not reproduced here since these details are available elsewhere (Lu et al., 2017c). The nondimensional form of particle–fluid–wall heat transfer for the original system and coarse-grained system can be written as

$$\overline{Q}_{i,w}^{\text{pfw, rp}} = f(\bar{\delta}_{rp}, \bar{r}_{len, rp}, \bar{s}_{rp}) \quad (66)$$

$$\overline{Q}_{i,w}^{\text{pfw, CGP}} = f(\bar{\delta}_{CGP}, \bar{r}_{len, CGP}, \bar{s}_{CGP}) \quad (67)$$

Therefore, the nondimensional particle–fluid–wall heat transfer is only related to the nondimensional particle wall distance, gas layer, and particle wall minimum distance. To ensure the heat conduction is the same for both systems, we must assume the nondimensional minimum distance and gas layer length are the same for the original system and coarse-grained system

$$\bar{r}_{len, CGP} = \bar{r}_{len, rp}, \quad \bar{s}_{CGP} = \bar{s}_{rp} \quad (68)$$

This relationship is also expressed graphically in Fig. 4. It can be seen that when the particle is not in contact with the wall ( $\delta_n < 0$ ), the heat transfer increases as the particle–wall distance decreases. However, when the particle contacts the wall, the heat transfer remains almost constant. Thus, we only need to ensure the same nondimensional particle–wall distance before a particle contacts the wall.

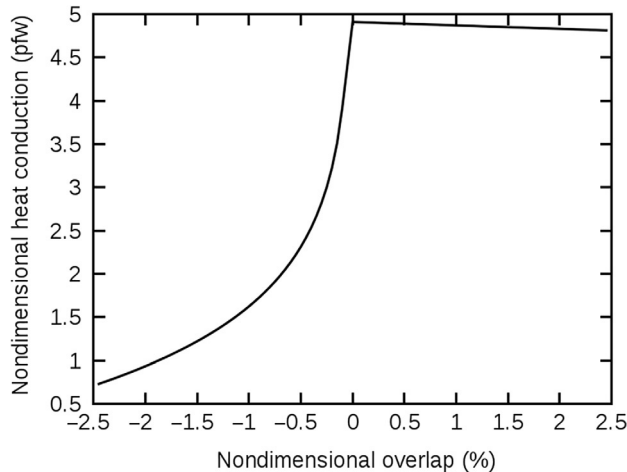


**Fig. 4** Nondimensional particle–fluid–wall heat transfer dependence on nondimensional overlap (nondimensional gas layer is set to 1.04 and nondimensional minimum distance is set to 0.001).

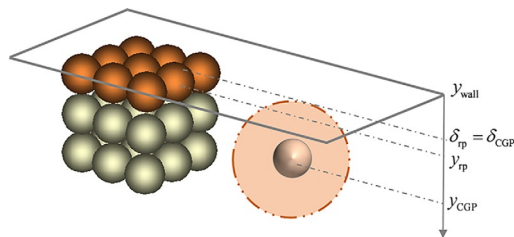


**Fig. 5** Relationship of wall distance for original and coarse-grained systems. For the original system only  $k^2$  particles (top layer orange-colored particles) are performing particle–fluid–wall heat transfer. Modified from Lu L, Morris A, Li T, Benyahia S: Extension of a coarse grained particle method to simulate heat transfer in fluidized beds. Int J Heat Mass Transf 111:723–735, 2017c with permission for the reprinted content. Copyright (2017) Elsevier.

For dimensionless particle wall distance, as shown in Fig. 5, we assume the particle center of the coarse-grained system to be identical to the averaged center of the original system. Thus, the distance to the wall is the same for both the original system and the coarse-grained system.

The CGP diameter  $d_{\text{CGP}}$  is used for both collision dynamics and particle–fluid–wall heat transfer. Thus, the relationship of dimensionless particle wall distance in the original system and the coarse-grained system is

$$\bar{\delta}_{\text{rp}} = k \bar{\delta}_{\text{CGP}} \quad (69)$$

Then, the dimensionless form particle–fluid–wall heat transfer for the coarse-grained system can be written as

$$\overline{Q}_{i,w}^{\text{pfw,CGP}} = f(k\bar{\delta}_{\text{CGP}}, \bar{r}_{\text{len,CGP}}, \bar{s}_{\text{CGP}}) \quad (70)$$

For the original system, only  $k^2$  particles (top layer orange colored particles in Fig. 5) are performing particle–fluid–wall heat transfer. Thus, the average value should be

$$\overline{Q}_{\text{avg}}^{\text{pfw,RP}} = \sum_{i=1}^W \overline{Q}_{i,w}^{\text{pfw,RP}} / W = \overline{Q}_{i,w}^{\text{pfw,RP}} / k \quad (71)$$

Considering  $\overline{Q}_{i,w}^{\text{pfw,RP}} = \overline{Q}_{i,w}^{\text{pfw,CGP}}$  and Eq. (60), we can get

$$Q_{\text{avg}}^{\text{pfw,RP}} = Q_{\text{avg}}^{\text{pfw,CGP}} / k^2 \quad (72)$$

This equation reveals that the particle–fluid–wall heat conduction in CGP method (CGPM) is  $k^2$  times larger than in the original system. To make sure that the two systems give the same result, the calculated particle–fluid–wall heat conduction in CGPM must be rescaled by a factor of  $1/k^2$ .

According to recent research (Zhou et al., 2009), in fluidized beds, particle–particle conduction through the contacting area accounts for less than 3% of the total conduction term. From an engineering point of view, this term may be neglected. However, for completeness, this conductive heat transfer model is described in Eqs. (73)–(80).

For the original system and the coarse-grained system, using Eq. (35), the colliding radius  $r_c$  can be written as

$$r_c^{\text{RP}} = \sqrt{2r_{\text{RP}}\delta_{\text{RP}} - \delta_{\text{RP}}^2} \quad (73)$$

$$r_c^{\text{CGP}} = \sqrt{2r_{\text{CGP}}\delta_{\text{CGP}} - \delta_{\text{CGP}}^2} \quad (74)$$

It is difficult to derive a precise relationship between  $\delta_{\text{RP}}$  and  $\delta_{\text{CGP}}$ . However, since the particle–wall contact conduction is small compared to particle–fluid–wall, a very simple assumption is used here. We use the maximum overlap instead of the otherwise variable overlap during the particle–wall collision. Since this collision is modeled here by a mass-spring-dashpot system, as derived in Buist et al. (2016), the maximum overlap can be expressed as

$$\delta_{\max} = \sqrt{\frac{v_0^2 m_{\text{eff}}}{k_n}} f(e) \quad (75)$$

where  $v_0$  is the initial collision velocity,  $k_n$  is the spring constant, and  $m_{\text{eff}}$  is effective mass. The expression of  $f(e)$  can be evaluated by

$$f(e) = e^{\frac{-\zeta}{\sqrt{1-\zeta^2}}} \cos^{-1}(\zeta), \quad \zeta = \frac{-\ln(e)}{\sqrt{\pi^2 + \ln(e)^2}} \quad (76)$$

Since the same spring constant  $k_n$  used in DEM is also used in our CGPM simulation, the overlap is calculated as

$$\delta_{\text{CGP}} = \delta_{\text{rp}} \sqrt{k^3} \frac{f(e_{\text{CGP}})}{f(e_{\text{rp}})} \quad (77)$$

The contact radius of the CGP is

$$r_c^{\text{CGP}} = k^{5/4} \left( \frac{f(e_{\text{CGP}})}{f(e_{\text{rp}})} \right)^{1/2} \sqrt{2r_{\text{rp}}\delta_{\text{rp}} - k^{1/2} \frac{f(e_{\text{CGP}})}{f(e_{\text{rp}})} \delta_{\text{rp}}^2} \quad (78)$$

In a DEM simulation, the particle–wall overlap is usually much smaller than the collision radius. The contact radius of the coarse-grained system can, therefore, be approximated as

$$r_c^{\text{CGP}} = k^{5/4} \left( \frac{f(e_{\text{CGP}})}{f(e_{\text{rp}})} \right)^{1/2} r_{\text{c}}^{\text{rp}} \quad (79)$$

The error introduced here due to coarsening depends on the restitution coefficient of the original system and scale ratio,  $k$ . We must also consider the particle–wall collision frequency. Thus, the equation for particle–wall contact conduction is

$$Q_{i,w}^{\text{pwc}} = \frac{Q_{\text{CGP}}^{\text{pwc}}}{k^{9/4}} \left( \frac{f(e_{\text{rp}})}{f(e_{\text{CGP}})} \right)^{1/2} \quad (80)$$

Similar to particle–wall heat conduction, the particle–particle conduction involves particle–fluid–particle conduction and particle–particle contact conduction. The relationship between the coarse-grained system and

the original system can be derived by following the same procedure as for particle–wall conduction. Considering a CGP representing  $k^3$  number of real particles, only  $k^2$  real particles on the surface can transfer heat to other CGP either through particle–fluid–particle conduction or contact conduction. Thus, the relationship derived for particle–wall conduction is still applicable to particle–particle conduction

$$Q_{\text{rp}}^{\text{pp}} = Q_{\text{rp}}^{\text{pfp}} / k^2 \quad (81)$$

$$Q_{\text{rp}}^{\text{pp}} = \frac{Q_{\text{CGP}}^{\text{pp}}}{k^{9/4}} \left( \frac{f(e_{\text{rp}})}{f(e_{\text{CGP}})} \right)^{1/2} \quad (82)$$

In a DEM simulation,  $r_c$  is usually overestimated due to the adoption of a smaller Yong's module to achieve large solids time step. Thus, it is difficult to calculate this term precisely even in DEM. Zhou et al. (2010) proposed a correction coefficient,  $c$ , to reduce this overestimation for DEM simulation with a Hertzian model. This correction has been extended to the linear spring–dashpot model in MFIX-DEM as

$$r_{c,0} = \left( \frac{k_n r_c}{k_{n,0}} \right)^{2/3} \quad (83)$$

where  $r_{c,0}$  is the reduced contact radius.  $k_n$  is the spring constant used in the simulation,  $k_{n,0}$  is the spring constant derived from Yong's modules of particles through

$$\begin{aligned} k_{n,0} &= \frac{4}{3} \sqrt{r_{\text{eff}}} E_{\text{eff}} \\ \frac{1}{r_{\text{eff}}} &= \frac{1}{r_i} + \frac{1}{r_j} \\ \frac{1}{E_{\text{eff}}} &= \frac{1 - \nu_i^2}{E_i} + \frac{1 - \nu_j^2}{E_j} \end{aligned} \quad (84)$$

where  $r_i$  and  $r_j$  are the particle radii of particles  $i$  and  $j$ .  $E_i$  and  $E_j$  are Yong's modules of particles  $i$  and  $j$ .  $\nu_i$  and  $\nu_j$  are Poisson ratios of particles  $i$  and  $j$ .

### 2.3 Extension to Time-Driven Hard-Sphere Contact Model

As will be shown later in this chapter, the main reason to investigate the hard-sphere collision model is the significant computer time savings it can achieve over the traditional soft-sphere model in DEM by allowing a larger solids time step yielding a speed-up of 20–60 times. In TDHS, CFD is used

to solve for the fluid flow on a fixed Eulerian mesh as mentioned earlier, while the motion of particles is solved by a Lagrange tracking method. The difference between TDHS and DEM is that the particle–particle interactions are modeled based on momentum conservation laws rather than a linear spring–dashpot. As proposed by [Ouyang and Li \(1999\)](#), the movement of particles in gas–solids flows is decomposed into suspension and collision processes. The suspension process accounts for external forces like gravity and interphase forces, while the collision process handles the instantaneous binary collisions.

For suspension processes, the velocities of particles are updated following Newton's law of motion

$$m_p \frac{d\mathbf{v}_p}{dt} = m_p \mathbf{g} - \frac{\pi}{6} d_p^3 \nabla P_f + \frac{\beta(\mathbf{v}_f - \mathbf{v}_p)\pi}{1 - \epsilon_f} \frac{\pi}{6} d_p^3 \quad (85)$$

where  $m_p$  is the mass of the particle,  $\mathbf{v}_p$  its velocity, and  $d_p$  its diameter. On the right-hand side, the forces considered include gravity, pressure gradient, and drag.

For collision processes, the velocities of particles are updated by instantaneous binary collisions. When particle  $i$  and  $j$  are in collision, the variation of momentum during impact is

$$\Delta \mathbf{P} = -m_e(1 + e_n) \mathbf{v}_n - \frac{2}{7} m_e(1 + e_t) \mathbf{v}_t \quad (86)$$

where  $m_e$  is the effective mass of two colliding particles and can be calculated as

$$m_e = \frac{m_i m_j}{m_i + m_j} \quad (87)$$

$\mathbf{v}_n$  and  $\mathbf{v}_t$  are relative velocity in normal and tangential directions and can be calculated as

$$\mathbf{v}_n = |\mathbf{v}_c| \mathbf{n} \quad (88)$$

$$\mathbf{v}_t = \mathbf{v}_c - \mathbf{v}_n \quad (89)$$

$$\mathbf{v}_c = \mathbf{v}_j - \mathbf{v}_i - (r_i \boldsymbol{\Omega}_i + r_j \boldsymbol{\Omega}_j) \times \mathbf{n} \quad (90)$$

$$\mathbf{n} = \frac{\mathbf{x}_i - \mathbf{x}_j}{|\mathbf{x}_i - \mathbf{x}_j|} \quad (91)$$

where  $\mathbf{x}_i$  and  $\mathbf{x}_j$  are positions of particle  $i$  and  $j$ . To consider the friction limit on tangential momentum variation, Eq. (86) is rewritten as

$$\Delta \mathbf{P} = -m_e(1 + e_n)\mathbf{v}_n + \mathbf{J}_t \quad (92)$$

$$\mathbf{J}_t = -\max \left( \frac{2}{7} m_e (1 + e_t) |\mathbf{v}_t|, \mu m_e (1 + e_n) |\mathbf{v}_n| \right) \frac{\mathbf{v}_t}{|\mathbf{v}_t|} \quad (93)$$

where  $\mu$  is sliding friction coefficient; then, the velocity of particle  $i$  and  $j$  can be updated as

$$\mathbf{v}_i = \mathbf{v}_i - \frac{\Delta \mathbf{P}}{m_i} \quad (94)$$

$$\mathbf{v}_j = \mathbf{v}_j + \frac{\Delta \mathbf{P}}{m_j} \quad (95)$$

As for particle rotation, it can be calculated as

$$\boldsymbol{\omega}_i = \boldsymbol{\omega}_i - \frac{r_i \mathbf{n} \times \mathbf{J}_t}{I_i} \quad (96)$$

$$\boldsymbol{\omega}_j = \boldsymbol{\omega}_j - \frac{r_j \mathbf{n} \times \mathbf{J}_t}{I_j} \quad (97)$$

where  $I$  is the moment of inertia and is equal to  $m_p d_p^2 / 10$ .

The grid-based neighbor list method is used for the collision detection process (Garg et al., 2012a). For each particle  $i$ , an array stores its neighbor particles. During the calculation, the program loops over all the neighbors of particle  $i$ . If they overlap while moving closer, the collision is identified and is handled by the previously described procedure. Since the collision is handled in a predefined sequence, the algorithm cannot ensure all the colliding particles separate from each other after each collision. Thus, there could be some unphysical large overlaps among particles in the dense phase where collision frequency is high. To reduce large overlaps created during the hard-sphere calculation step, a novel velocity correction procedure is carried out right after the collision process. It loops over all the particles still in collision after the traditional hard sphere collision process. This correction algorithm corrects particle velocity in such a way that the largest overlaps are reduced the most by emphasizing particles with the largest overlaps and largest colliding velocity. To achieve this reduction in overlap, this model requires two unknown parameters that can be adjusted to achieve a reasonable overall overlap. We found that these parameters can be expressed by analogy with a spring-dashpot model. This provided reasonable overlaps that were comparable to those achieved by DEM simulation. The whole algorithm is shown in Fig. 6.

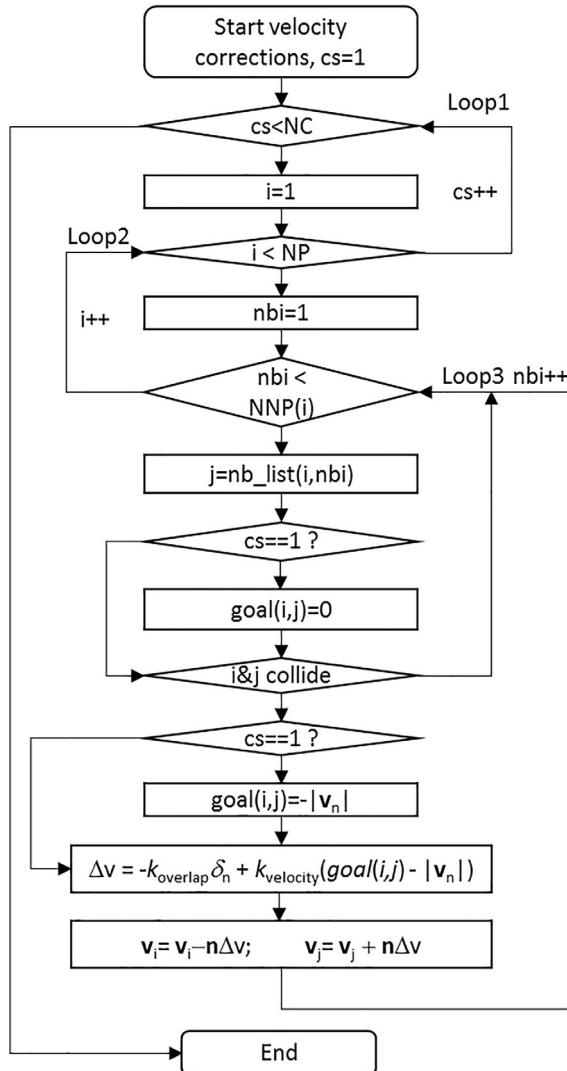


**Fig. 6** Velocity correction procedure conducted right after the collision process.

As shown in Fig. 6, Loop 1 indicates that the correction loops over user-defined maximum correction steps, NC. Loop 2 and Loop 3 indicate that for each particle, the algorithm will loop over all its neighboring particles. If a collision is detected, which means two particles are overlapping and moving toward each other, a corrected velocity is calculated. The calculated correction term is a penalty function of overlap,  $\delta_n$ , and the desired relative

velocity. It should be noted that in dense flows where many overlaps exist between particles, this algorithm is only designed to reduce the largest overlaps that will otherwise be present in the next time step. For these dense flows, the exit out of this iteration loop is usually obtained by reaching the maximum correction steps, which typically comprise a small value of 2–3 steps. The two stiffness parameters,  $k_{\text{overlap}}$  and  $k_{\text{velocity}}$ , can be selected with an analogy to soft-sphere DEM by setting  $k_{\text{overlap}} = \Delta t k_n / m_p$  and  $k_{\text{velocity}} = \Delta t \eta_n / m_p$ . Where  $k_n$  is the normal spring constant and  $\eta_n$  is the damping coefficient.

Although the CFD–TDHS method is much faster than traditional CFD–DEM by using a larger time step, it is still not fast enough for industrial- or pilot-scale problems because of the large number of particles in these systems. However, CFD–TDHS can be easily combined with the parcel-based method. Also, since the interaction between particles is modeled by momentum conservation laws, there is no need to derive the scaling laws for spring stiffness as used in DEM. The previous scaling laws for the restitution coefficient are based on the fact that the particle collision frequency is significantly reduced in the coarse-grained method; thus, these laws are still valid for the hard sphere method. To distinguish it from particle-based method, the coarse-grained hard sphere method is abbreviated as CGHS. The CGHS is validated through the simulation of a pilot-scale CFB riser, which will be discussed in [Section 3.5](#).



### 3. VERIFICATION AND VALIDATION STUDIES

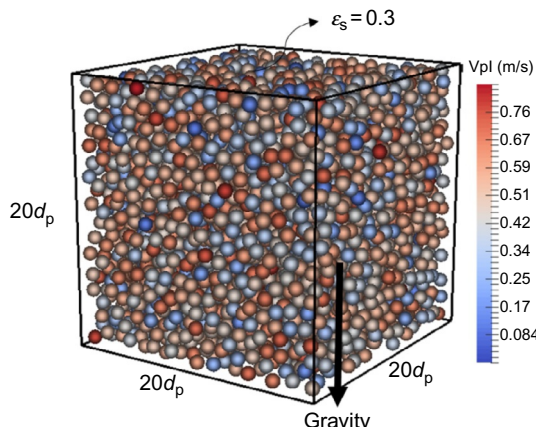
The methods discussed in [Section 2](#) are all implemented in the freely available open-source multiphase flow simulation code MFIX. The MFIX–DEM code has been involved in some verification studies ([Garg et al., 2012b](#)) as well as validations ([Li et al., 2012b](#)) and has been widely used by the multiphase flow modelling and simulation community. In this section, coarse-grained CFD–DEM, TDHS, CFD–TDHS, and CFD–CGHS are subjected to some validation studies either by comparing their predictions with available experimental data or with more precise simulation methods like CFD–DEM or DNS. The first step is verifying the ability of the TDHS method to simulate dense granular flow and particle packing. The second step also involves the V&V of CFD–TDHS by simulating a small bubbling fluidized bed and comparing the results with CFD–DEM, DNS, and experimental data. The third step is verifying the major assumption of coarse graining CFD–DEM and CFD–CGHS by simulating a small

bubbling fluidized bed and comparing the results with CFD–DEM. The fourth step is the V&V of the heat transfer models presented in this study for coarse-grained CFD–DEM by simulating a small bubbling fluidized bed and comparing the results with CFD–DEM and experimental data. Finally, the CFD–CGHS is validated by simulating a pilot-scale CFB riser where experimental data are available.

### 3.1 Verification Study of the Time-Driven Hard Sphere Model for Dense Granular Flow

The TDHS was implemented in the MFIX CFD code and verified for a simple homogeneous cooling system, particle settling case, and bubbling fluidized bed in a recent publication (Lu et al., 2017d). As explained in Section 2.3, the TDHS is unable to handle multibody collisions and will result in unphysical overlaps for dense granular flow. In this verification study, a simple particle settling system is simulated with DEM and TDHS. As shown in Fig. 7, initially, the particles are randomly distributed in the simulation box with a small random velocity or granular temperature. Then, under the pull of Earth’s gravity, the particles settle to the bottom wall of the simulation domain. The detailed simulation parameters are listed in Table 1.

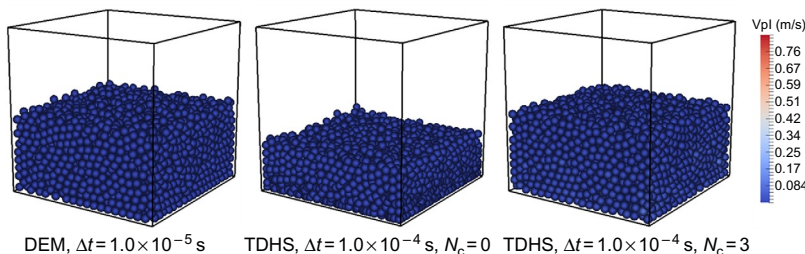
Fig. 8 compares the results of DEM, original TDHS method, and TDHS with our proposed corrections as detailed in Section 2.3. We first notice that the initial random velocity of the particles, as seen in Fig. 7, is quickly and significantly reduced due to the energy-dissipating collisions. Qualitatively, this figure shows that the original TDHS cannot predict a correct packing



**Fig. 7** Initial conditions and system geometry of particles settling under gravity.

**Table 1** Simulation Parameters of Particles Settling System

Parameter or Property	Values
Particle diameter, $d_p$ (m)	$1.0 \times 10^{-3}$
Particle density, $\rho_p$ ( $\text{kg}/\text{m}^3$ )	2500
Particle spring constant, $k_n$ ( $\text{N}/\text{m}$ )	$1.0 \times 10^2$
Particle restitution coefficient, $e_n$	0.95
Particle friction coefficient, $\mu$	0.10
Particle restitution coefficient, $e_t$	0.95
Particle wall friction coefficient, $\mu_w$	0.10
Average solid volume fraction, $\varepsilon_s$	0.30
Domain size, $W \times H \times D$	$20d_p \times 20d_p \times 20d_p$
DEM time step (s)	$1.0 \times 10^{-5}$
TDHS time step (s)	$1.0 \times 10^{-4}$ , $1.0 \times 10^{-5}$
TDHS velocity correction steps	0,3,11

**Fig. 8** Particle positions after 500 ms,  $N_c$  indicates the number of velocity corrections.

density without our proposed velocity correction term. This is because, for this settling case, the dominate contact mechanism is multibody collision, which is beyond the capability of the original TDHS. Without our proposed corrections, the particles will keep collapsing, which will cause many particles to completely overlap. However, this unphysical overlap can be reduced by the proposed velocity correction algorithm. This correction term prioritizes the separation of colliding particles with largest overlaps and largest collision velocities. This algorithm may result in small overlaps and/or a minor increase of overlaps for other particles, which was insignificant for the macroscopic results. A simple demonstration of this algorithm was conducted for a 1D simulation of three particles under gravity (Lu et al., 2017d).

We should stress the fact that predicting the wrong solids packing has a profound impact on the fluidization behavior of powders. Simply put, predicting the wrong solids packing implies the wrong value of computed drag force, which implies the wrong fluidization behavior. Therefore, reducing errors of void fraction calculation is essential for a method such as TDHS to have any practical application in fluidization.

Apart from the above qualitative analysis, we also quantitatively analyzed the influence of the number of correction steps and the computation time steps on the settling process by comparing the normalized weight center, which relates directly to the solids packing fraction. As shown in Fig. 9, for DEM simulations, the normalized weight center stabilizes around a value of 0.5 after a settling time of only about 0.06 s (recall that this simulation is conducted in a small system geometry). Considering that the initial solids volume fraction is 0.3, the final packing solids volume fraction is about 0.6, which is a reasonable value for random packing of spheres. Before this maximum packing value is reached, or before 0.06 s, the system is dominated by binary collisions and, even without any correction, the original TDHS can predict the same profile as DEM. However, after 0.06 s, the system is densely packed and dominated by multibody enduring contacts. The predicted profile obtained with the original TDHS keeps

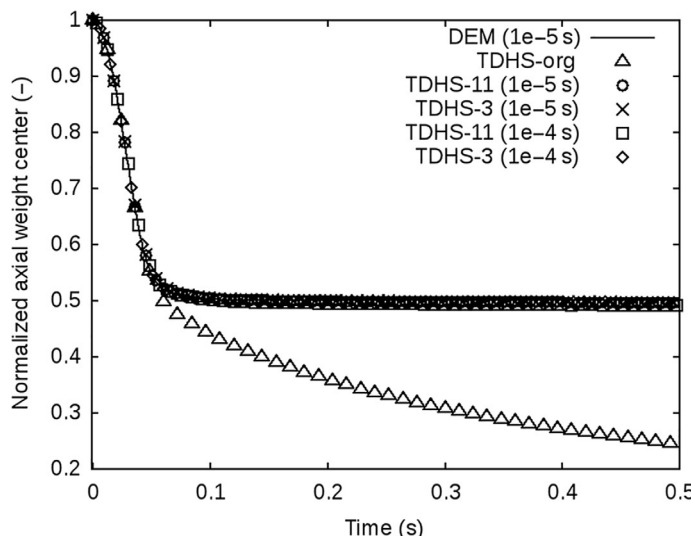


**Fig. 9** Particle normalized weight center with different number of correction and time steps. Modified from Lu L, Li T, Benyahia S: An efficient and reliable predictive method for fluidized bed simulation. *AIChE J* 63, 5320–5334, 2017d, <https://doi.org/10.1002/aic.15832> with permission for the reprinted content. Copyright (2017) Wiley.

decreasing and at 0.5 s the predicted normalized weight center is about 0.25 that of the initial value. This means the packing density is about 1.2, which is physically impossible. If our proposed velocity correction is used, then the TDHS can avoid this unphysical phenomenon and predicts a similar profile and packing value as DEM while using an order of magnitude larger computation time step. Also, the influence of the number of correction steps and computation time steps on the final packing density is small. This means that the proposed modification to the TDHS method can be used with a much larger time step than DEM, which will allow for a large increase in the simulation speed.

To further analyze the influence of the number of correction steps and computation time steps, we also compare the normalized kinetic energy of the system predicted by different methods. As shown in Fig. 10, the kinetic energy predicted by the DEM simulation can be reduced to about  $10^{-9}$  of the initial value in the system. Theoretically this value should tend to zero, and the small value obtained by DEM is mainly caused by numerical errors. For TDHS, the computation time step has a major influence on the results. For larger time steps ( $1.0 \times 10^{-4}$  s), the kinetic energy is only dissipated to about 0.001 of the initial system value. This is because the TDHS algorithm does not resolve the particle collision process as in DEM. During the correction process, the potential energy stored in overlaps is transformed to kinetic energy. Since a larger time step is used, numerical errors occur during

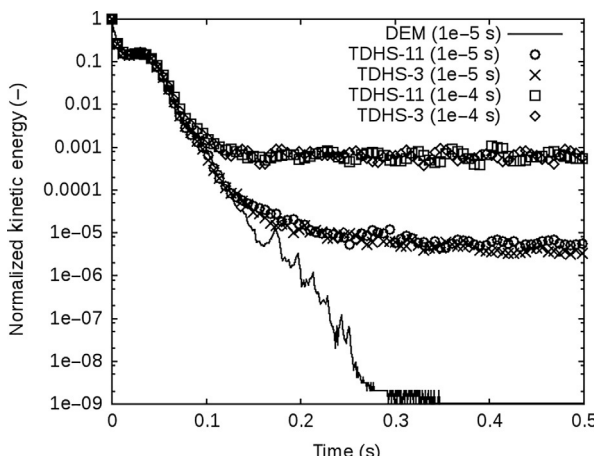


**Fig. 10** Particle normalized kinetic energy with different numbers of correction and time steps. Modified from Lu L, Li T, Benyahia S: An efficient and reliable predictive method for fluidized bed simulation. *AIChE J* 63, 5320–5334, 2017d, <https://doi.org/10.1002/aic.15832> with permission for the reprinted content. Copyright (2017) Wiley.

this transformation that generate an excess of kinetic energy. When this numerically generated energy reaches a value comparable to that dissipated by the collision process, the total kinetic energy fluctuates around a stable value. This numerical error can be significantly reduced by reducing the solids time step. As an example, decreasing the time step by an order of magnitude to a value of  $1.0 \times 10^{-5}$  s can reduce the energy dissipation to about  $10^{-5}$  of the initial system. This reduction in numerical errors with the smaller time step of the corrected TDHS method can be useful in engineering applications. For example, a larger time step may be used at the first stages of a simulation and then reduced to improve simulation results if more computational resources become available or more accurate simulation results are required. Nevertheless, it is obvious to us that the gain in speed obtained with a larger solids time step compensates for the small loss of accuracy. Another observation is that the number of correction steps exerts only a minor influence on the final results. This is because most of the large overlaps are reduced after a few corrections, and overlaps still existing after the corrections in this time step will be further reduced in the next step.

Now we may conclude that using a velocity correction algorithm significantly reduces the unphysical overlaps and that TDHS can predict results similar to results with the DEM method for dense granular flow. Thus, this method can be used to simulate dense and CFBs where multibody collisions may also play an important role in stagnation zones and dense clusters.

### 3.2 Validation of Time-Driven Hard Sphere Model for Bubbling Fluidized Bed

Although CFD–TDHS has been used to simulate gas–solids flows ([Helland et al., 2005](#); [Ouyang and Li, 1999](#)), this method lacks thorough V&V by comparing its predictions with experimental measurements and other more precise simulation methods like DEM and DNS. In this section, the V&V of CFD–TDHS is conducted through the simulation of a small fluidized bed. The time-averaged solids flux spatial distributions is compared with experimental data as well as with DNS results using the immersed boundary method (IBM) ([Tang et al., 2016](#)). The simulation domain and boundary conditions are shown in [Fig. 11](#). Initially, the particles are randomly generated in the whole physical domain. A settling period follows, to allow the particles to pack under the force of gravity at the bottom of the bed, then the fluidized bed simulation starts. During this simulation, air flows uniformly into the reactor at the bottom of the bed with a superficial velocity of 2.4 m/s, while the outlet located at the top of the bed is set at a constant atmospheric pressure of 101 kPa. The system geometry consists also of left,

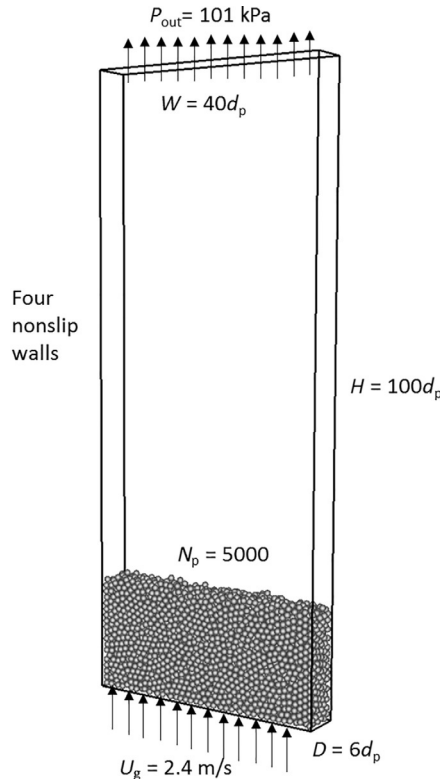


**Fig. 11** Simulation setting of small bubbling fluidized bed.

right, front, and back walls, which are all set to nonslip walls for the gas phase. The Syamlal and O'Brien drag model is used. We stress that the same initial and boundary conditions are used for both CFD-DEM and CFD-TDHS simulations that were conducted in this study. Other simulation parameters are listed in Table 2. Further details of this case can be found in a recently published paper (Lu et al., 2017d).

The instantaneous particle positions colored with their velocities are presented in Fig. 12. The predicted flow patterns obtained with CFD-DEM and CFD-TDHS are reasonably similar. Both are characterized by a large upward-moving bubble in the center and downward flow of particles near the side walls. This fluidization behavior of Geldart D particles in a shallow bed may exhibit slugging for deeper beds, which is typically observed in the fluidization of such coarse particles. For brevity, only one instant screenshot is shown here, while the fluidized bed is simulated for 40 s with 800 saved frames, and the corresponding Video 2 in the online version at

**Table 2** Simulation Parameters in Bubbling Fluidized Bed

Parameter or Property	Value
Particle diameter, $d_p$ (m)	$2.5 \times 10^{-3}$
Particle density, $\rho_p$ (kg/m <sup>3</sup> )	2526
Particle spring constant, $k_n$ (N/m)	$8.0 \times 10^2$
Particle restitution coefficient, $e_n$	0.97
Particle friction coefficient, $\mu$	0.1
Particle restitution coefficient, $e_t$	0.33
Particle wall friction coefficient, $\mu_w$	0.2
Superficial gas velocity, $u_g$ (m/s)	2.4
Domain size, $W \times H \times D$	$40d_p \times 100d_p \times 6d_p$
CFD grid number, $N_w \times N_h \times N_d$	$20 \times 50 \times 3$
Solid time step (s)	$1.0 \times 10^{-5}$ (DEM), $1.0 \times 10^{-4}$ (TDHS)
CFD time step (s)	$1.0 \times 10^{-4}$
Particle number $N_p$	5000

<https://doi.org/10.1016/bs.ache.2017.12.001> is uploaded as supplementary material. Of course, these two methods do not predict the exact same results because particle–particle interactions are handled differently, and a much larger time step is used for CFD–TDHS.

An interesting quantity to measure is the Favre-averaged velocity, or the solids volume flux, which is the time-averaged value of the product of the instantaneous solids velocity and volume fraction. It is compared quantitatively with experimental and DNS data in Fig. 13. The simulation results are averaged from 10 to 40 s with a frequency of 20 Hz, while the experimental data and IBM results are reproduced from the published literature (Tang et al., 2016). At a height of 0.025 m above the gas distributor, the simulated results compare well with both experimental data and DNS simulation results. Both CFD–DEM and CFD–TDHS predict quantitatively the correct trends with an upward flow in the center of the bed and a downward flow near the wall region. At a height of 0.055 m, the simulation still predicts the correct quantitative trends of an upward flow of solids in the center of the bed with an underpredicted downflow of solids near the wall region compared to experimental measurements. This may have been caused by

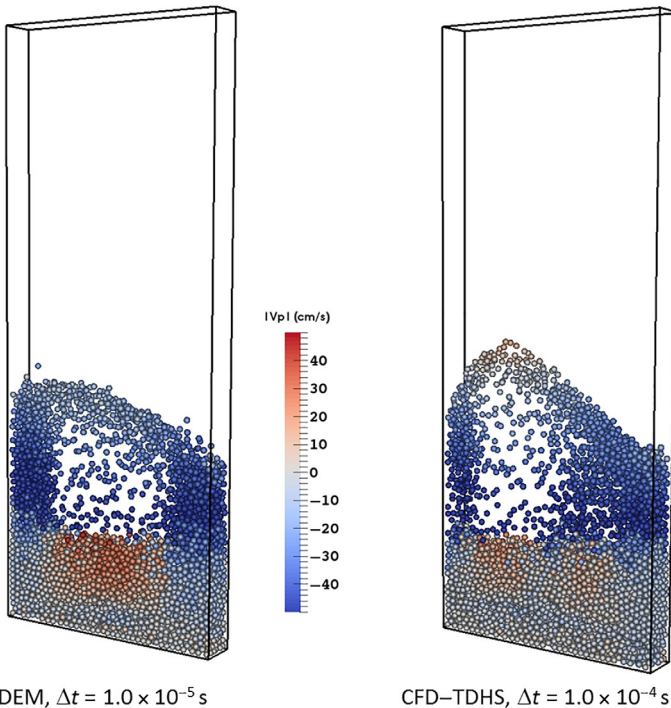


**Fig. 12** Instantaneous particles distribution obtained with CFD-DEM and CFD-TDHS.

inaccurate modelling of particle–wall interactions and near-wall fluid flow field. Nevertheless, the CFD–TDHS predictions are very similar to those obtained with CFD–DEM, which evidently demonstrates that CFD–TDHS is at least as accurate as CFD–DEM. At a height of 0.085 m, all the numerical methods failed to predict the correct quantitative experimentally measured profile of solids Favre velocity. Like the results obtained at a height of 0.055 m, the simulation results at 0.085 m underpredict the negative solids flux experimentally observed near the wall as well as the upward solids flow at the center of the bed. However, the result of CFD–TDHS is still very similar to that obtained with our CFD–DEM, which is also in reasonable agreement with the published DNS data. We should mention here that all the numerical techniques compared here are CFD-based, but we recognize that DNS data are the most accurate because it makes no assumption on any fluid–particle interaction terms as the flow around each particle is fully resolved. All these terms, such as fluid–particle drag force, added mass, and lift forces (not included in this study), are explicitly calculated in DNS without any assumption. Obviously the best accuracy we can hope for our simulation results to achieve is that of DNS. Achieving similar quantitative trends as those

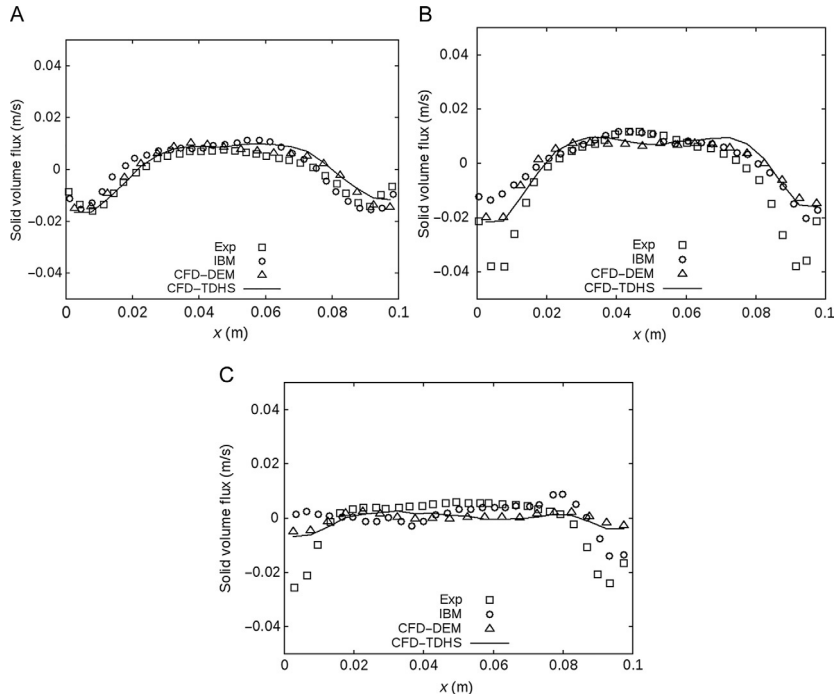


**Fig. 13** Solids volumetric flux profile at different heights simulated with CFD-DEM and CFD-TDHS. (A) Height = 0.025 m, (B) height = 0.055 m, (C) height = 0.085 m. Modified from Lu L, Li T, Benyahia S: An efficient and reliable predictive method for fluidized bed simulation. AIChE J 63, 5320–5334, 2017d, <https://doi.org/10.1002/aic.15832> with permission for the reprinted content. Copyright (2017) Wiley.

obtained with DNS is, therefore, satisfactory even though some quantitative disagreement with experimental measurements persists.

In addition to first-order statistics, we also compared the particles fluctuating energy, also known as granular temperature, which is a second-order statistical quantity of interest. It can be estimated as

$$\Theta = \frac{1}{3} (\Theta_x + \Theta_y + \Theta_z) \quad (98)$$

$$\Theta_x = \frac{1}{N} \sum_{i=1}^N (\nu_x - \bar{\nu}_x)^2 \quad (99)$$

$$\Theta_y = \frac{1}{N} \sum_{i=1}^N (\nu_y - \bar{\nu}_y)^2 \quad (100)$$

$$\Theta_z = \frac{1}{N} \sum_{i=1}^N (\nu_z - \bar{\nu}_z)^2 \quad (101)$$

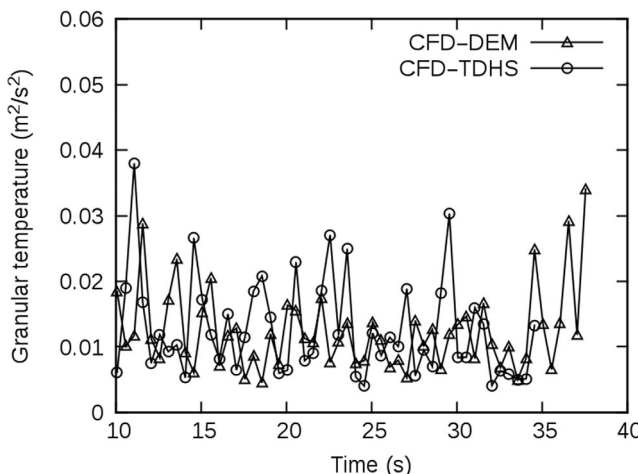


**Fig. 14** Granular temperature profiles predicted with CFD–DEM and CFD–TDHS methods. Modified from Lu L, Li T, Benyahia S: An efficient and reliable predictive method for fluidized bed simulation. *AIChE J* 63, 5320–5334, 2017d, <https://doi.org/10.1002/aic.15832> with permission for the reprinted content. Copyright (2017) Wiley.

To calculate this second-order statistical quantity, first the velocities of all particles in the simulation domain were spatially averaged. Then, the square of the velocity difference between each individual particle and the domain-averaged value was again spatially averaged and plotted against time. As shown in Fig. 14, both the transient behavior of the particle fluctuating energy as well as the time-averaged values were very similar for DEM and the newly developed CFD–TDHS method. Note that this higher statistical quantity of interest was not measured in the published literature for this case; no direct comparison between our current results and experimental/DNS data is possible. Taking the results of DEM as a reference value, the relative error for CFD–TDHS was 6.4%. These quantitative comparisons of DEM and TDHS support the conclusion that these two techniques yield similar low and high-order statistical predictions. This strongly supports the TDHS technique because it gives similar accuracy as DEM but with a much faster (20–60 times faster) execution speed.

### 3.3 Verification Study of Coarse-Grained Soft-Sphere and Hard-Sphere Contact Models

Previous results indicate that the CFD–TDHS predictions are similar to those obtained using CFD–DEM with the benefit of a much larger time step.

However, for large-scale systems, the computation speed is still not fast enough to obtain predictions in a reasonable time frame due to the large number of particles in these systems. To further reduce the computation cost in CFD–DEM and CFD–TDHS, several real particles are lumped into a computational parcel, which tracks fewer parcels and their collisions. In this section, a virtual bubbling fluidized bed is simulated with CFD–DEM, coarse-grained CFD–DEM, and CFD–CGHS methods. Since no experimental data are available for this hypothetical system, we consider this study as a verification exercise of the coarse-grained soft-sphere (DEM) and hard-sphere (TDHS) methods by comparing these coarse methods with the finer CFD–DEM approach that tracks each individual particle instead of computational parcels. The simulation domain is double the width, depth, and height of the small fluidized bed in [Section 3.2](#), and so to keep the same particle volume fraction, the number of particles is increased by eight times (double in all three physical directions). Other parameters such as boundary conditions, gas and particle properties, and CFD grid size are the same as those used in [Section 3.2](#). For simulations with coarse-grained CFD–DEM and CFD–CGHS, the parcel diameter is twice the real particle size, which indicates each computational parcel contains eight real particles.

The instantaneous particle distributions colored with their velocities obtained with three different methods are compared in [Fig. 15](#). The qualitative

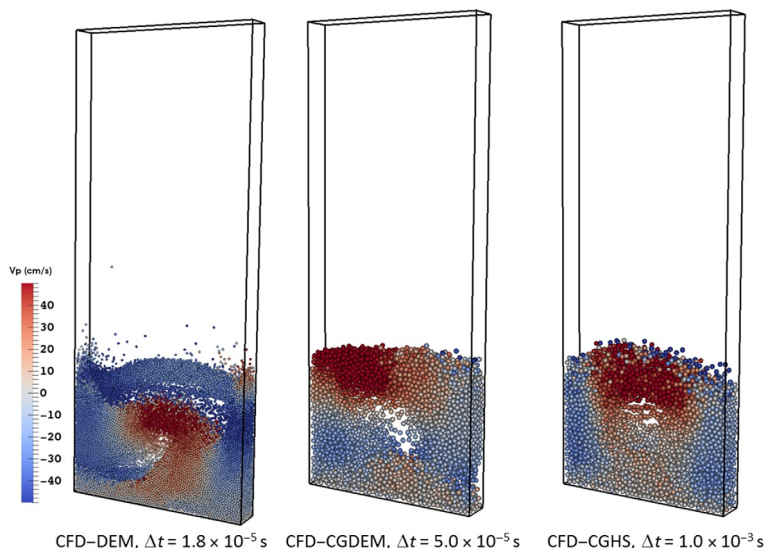


**Fig. 15** Instantaneous particle distribution obtained with CFD–DEM, CFD–CGDEM, and CFD–CGHS.

predictions of gas and solids flow patterns obtained with coarse-grained CFD–DEM and CFD–CGHS compared well with the finer CFD–DEM simulation results. All the simulation results show a large bubble in the center of the pulsing fluidized bed. The dynamic flow patterns in this fluidized bed are recorded in Video 3 in the online version at <https://doi.org/10.1016/bs.ache.2017.12.001> that is uploaded as a supplementary material available for the reader. Similar fluidization behavior can be observed in the animation for all three methods studied here. It is important to note that by lumping eight particles into a computational parcel, the number of computational parcels are reduced by a factor of eight, and that for the coarse-grained CFD–DEM the solids phase time step increases by a factor of about three due to the tracking of larger parcels. For CFD–CGHS, the solids phase time step is further increased by a factor of 20 due to the particle–particle collisions being handled by momentum conservation laws, and, thus, they do not need to be resolved like the soft-sphere collision method.

Macroscopic quantities of interest to engineers, such as solids velocity and solids volume fractions, are quantitatively compared in Fig. 16 for the three methods examined in this section. The simulation results are time-averaged from 20 to 50 s with a frequency of 20 Hz. At a height of 0.05 m above the gas distributor, both CFD–CGDEM and CFD–CGHS predict similar results to those obtained with finer CFD–DEM simulation. As typically observed in bubbling fluidized beds, particles tend to flow upward in the center of the bed where bubbles flow, and downward near the walls of the bed, which creates the large-scale recirculation of solids that is simply due to gas dragging particles against the constant pull of Earth's gravity. At a height of 0.11 m, the coarse methods still predict similar flow patterns as the finer method, with the

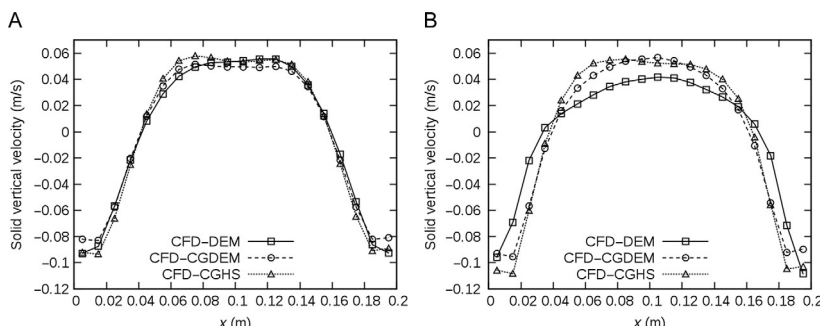


**Fig. 16** Solids vertical velocity profile at different heights simulated with CFD–DEM, coarse-grained CFD–DEM, and CFD–CGHS. (A) Height = 0.05 m, (B) height = 0.11 m.

coarse-grained methods overpredicting the solids velocity both in the center upward flow and near the wall downward flow. This is because, in a coarse-grained system, the particles in a parcel are forced to move together, which reduces the degree of freedom in the system. The energy of the system also changes due to differences in the number of collisions. As with any other coarser approaches, significant gains in computation speed are always accompanied by some loss in accuracy. Carefully balancing speed with acceptable model-induced uncertainty is required by practicing engineers and researchers while using this or any other coarse method.

The solid volume fractions obtained with the three approaches used in this study are quantitatively compared in Fig. 17. At a lower height of 0.05 m, coarse-grained methods slightly underpredict the results obtained with finer CFD-DEM. However, at a height of 0.11 m a reversed phenomenon is observed where the coarse-grained methods now overpredict the results obtained with CFD-DEM. Overall, the larger axial gradients in solids volume fraction exist for the finer CFD-DEM method, which could occur because of a larger energy dissipation due to more frequent particle-particle collisions that increase inhomogeneity in the fluidized bed. Nevertheless, the quantitative differences between the fine and coarser methods are as small as other source of numerical errors, such as the time-averaging period.

As mentioned earlier, it is difficult to declare coarse methods fully verified and declare their use as validated to the practicing engineer or researcher. In general, it is fair to say that when speed is paramount, such as in many industrial applications, and some loss in accuracy can be tolerated, then the use of coarse techniques such as those explored here is fully warranted and must be pursued.

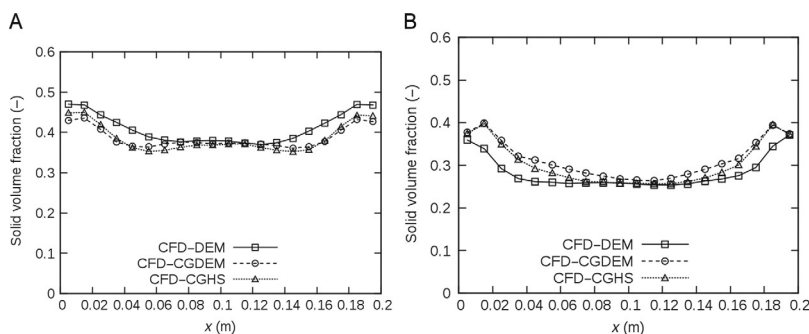


**Fig. 17** Solids volume fractions at different heights simulated with CFD-DEM, coarse-grained CFD-DEM, and CFD-CGHS. (A) Height = 0.05 m, (B) height = 0.11 m.

### 3.4 Validation of Heat Transfer in Coarse-Grained Soft-Sphere Contact Model

To validate the heat transfer model developed in the methods section for coarse-grained CFD-DEM, a gas–solids fluidized bed (where experimental data are available) is simulated in this section. This fluidized bed has been experimentally investigated by Patil et al. (2015), and the physical domain is shown in Fig. 18. In this fluidized bed, glass beads initially at 90°C are fluidized by a cooler nitrogen gas at 20°C. The front plate of the bed is made of sapphire glass, while the back and side walls are made of aluminum. Experimentally, a circular nozzle with a diameter of 1.3 cm is located at the bottom of the bed. In neither the simulation nor the experimental run considered in this study, is gas injected through this nozzle, which is considered simply as a blocked area. In the simulation, however, this area is blocked with a rectangular  $1.14 \text{ cm} \times 1 \text{ cm}^2$  surface. There is an exception for simulation with a statistic weight of 27 (case W27), where the CFD grid is too large to resolve this small rectangular patch. Therefore, to ensure the same fluid flow rate through the bottom inlet, the superficial gas inlet velocity for case W27 is reduced from 1.33 to 1.20 m/s. The BVK drag model, described in the methods section, is used in this simulation. Other simulation

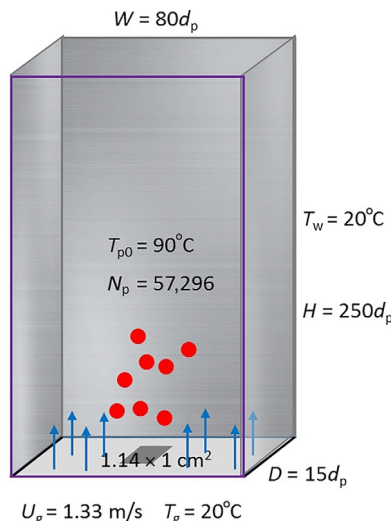


**Fig. 18** Simulation setup for heat transfer bubbling fluidized bed. Modified from Lu L, Morris A, Li T, Benyahia S: Extension of a coarse grained particle method to simulate heat transfer in fluidized beds. Int J Heat Mass Transf 111:723–735, 2017c with permission for the reprinted content. Copyright (2017) Elsevier.

parameters and physical properties are listed in [Tables 3 and 4](#). More simulation details on this case can be found in a recently published paper ([Lu et al., 2017c](#)).

Since the aluminum constituting most of the side walls in this fluidized bed is of high thermal conductivity, a constant wall temperature boundary condition (293 K) is used for all the walls. The cooling line, representing

**Table 3** Simulation Parameters and Physical Properties of Heat Transfer  
**Parameter or Property** **Value**

Parameter or Property	Value
Particle diameter, $d_p$ (m)	$1.0 \times 10^{-3}$
Particle density, $\rho_p$ (kg/m <sup>3</sup> )	2500
Particle spring constant, $k_n$ (N/m)	$1.0 \times 10^2$
Particle restitution coefficient, $e$	0.97
Particle friction coefficient, $\mu$	0.30
Particle heat capacity, $C_p$ (J/kgK)	840
Particle thermal conductivity, $k_p$ (W/mK)	1.40
Aluminum thermal conductivity, $k_{Al}$ (W/mK)	238
Sapphire thermal conductivity, $k_{Al}$ (W/mK)	40
Fluid heat capacity, $C_f$ (J/kgK)	1010
Fluid viscosity, $\mu_f$ (kg/ms)	$2.0 \times 10^{-5}$

**Table 4** Simulation Parameters for CFD–DEM and CFD–CGDEM of Heat Transfer

	CFD–DEM	W8	W27
CFD grids, $N_x \times N_y \times N_z$	$35 \times 110 \times 6$	$35 \times 110 \times 6$	$16 \times 50 \times 3$
CFD time step, $\Delta t$ (s)	$1.0 \times 10^{-4}$	$5.0 \times 10^{-4}$	$5.0 \times 10^{-4}$
Number of CGP, $N_{CGP}$	57,296	7162	2122
Statistic weight, $W$	1	8	27
Solid time step, $\Delta t$ (s)	$1.27 \times 10^{-5}$	$1.44 \times 10^{-5}$	$2.64 \times 10^{-5}$
Gas layer diameter, $\eta_{len}$ (m)	$1.04 \times 10^{-3}$	$2.08 \times 10^{-3}$	$3.12 \times 10^{-3}$
Minimum conduction distance, $s$ (m)	$1.0 \times 10^{-6}$	$2.0 \times 10^{-6}$	$3.0 \times 10^{-6}$
Fluid inlet velocity, $U_f$ (m/s)	1.33	1.33	1.20

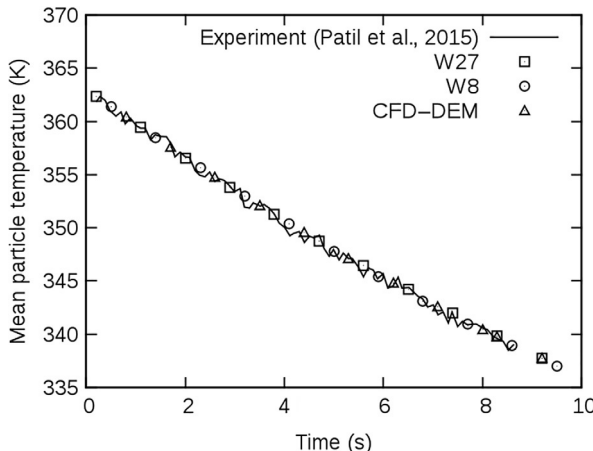


**Fig. 19** Mean particle temperature profile simulated with different  $W$  and constant wall temperature boundary conditions. Modified from Lu L, Morris A, Li T, Benyahia S: Extension of a coarse grained particle method to simulate heat transfer in fluidized beds. *Int J Heat Mass Transf* 111:723–735, 2017c with permission for the reprinted content. Copyright (2017) Elsevier.

the mean temperature of particles, obtained experimentally, by DEM, and by coarse grained DEM with different statistic weight, is compared in Fig. 19. As shown, the mean particle temperature profile simulated with different  $W$  (recall that  $W$  stands for number of real particles in a parcel) compared well with experimental data. This indicates that the constant temperature boundary condition is close to reality. Also, the proposed heat transfer model for coarse-grained CFD–DEM can correctly predict the macroscale temperature transient variations for this particular case study.

To further verify the heat transfer model for coarse-grained CFD–DEM, different heat transfer mechanisms are quantitatively analyzed and compared with the finer method of CFD–DEM. In this fluidized bed, the effect of radiative heat transfer is ignored because the temperature is relatively low. The implementation and validation of heat transfer by radiation is left for future work and is not discussed in this chapter. The heat in particles is only lost by particle–fluid convection, particle–fluid–wall conduction, and particle–wall contact conduction. These different heat transfer mechanisms are quantitatively compared in Fig. 20 using numerical results obtained from CFD–DEM and coarse-grained CFD–DEM simulations. For the most important heat-transfer mechanism (particle–fluid convection term), the CFD–DEM results agree quantitatively well with those using the lower

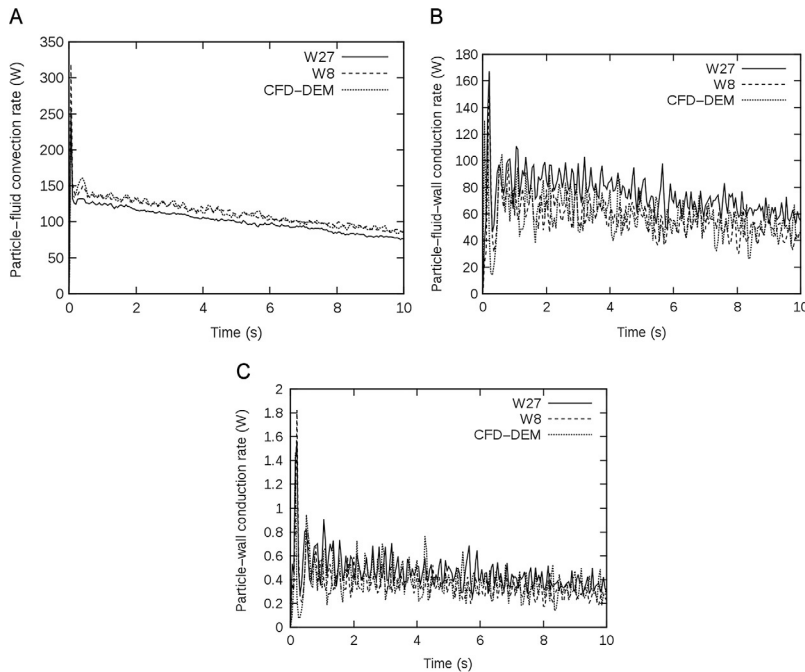


**Fig. 20** Comparison of different heat transfer mechanisms calculated with different  $W$ . (A) particle–fluid convection, (B) particle–fluid–wall conduction, (C) particle–wall contact conduction. Modified from Lu L, Morris A, Li T, Benyahia S: Extension of a coarse grained particle method to simulate heat transfer in fluidized beds. *Int J Heat Mass Transf* 111:723–735, 2017c with permission for the reprinted content. Copyright (2017) Elsevier.

coarsening level (W8), while the results obtained with the most aggressive coarsening level (W27) underpredict the DEM results. Apart from errors inherent to coarse-graining, using coarser CFD grids, as in case W27, may have contributed further to this quantitative disagreement between coarse and finer methods. The rate of particle–fluid convection decreases gradually with time from an initial value of about 150–100 W after 10.0 s of simulation time, which was due to the temperature gradient between fluid and particles decreasing as the particle temperature decreases with time. The second most important heat transfer mechanism in this fluidized bed simulation is due to particle–fluid–wall conduction as indicated in Fig. 20B. For this mechanism, the results obtained with different grain-coarsening levels ( $W$ ) are very similar. This proves the accuracy of our previously proposed particle–fluid–wall conduction model. Similar to the convective heat transfer term, the conductive heat transfer rate decreases

from about 80 to 50 W indicating a decrease in the temperature gradient between particle and wall as time progresses. Finally, for particle–wall conduction, the heat transfer rate is the least important heat transfer mechanism with values less than 1 W. Although it seems that this value is negligible in this fluidized bed case, the results obtained with different statistical weights compared well with those obtained with DEM, indicating the accuracy of our proposed model for particle–wall conduction.

Although this case study and those previously conducted in this chapter are relatively simple because they deal mainly with small-scale fluidized beds, the case studies reveal that the coarse-grained method described in this chapter captures, with reasonable accuracy, both the hydrodynamic and heat transfer in fluidized beds. Next, we will be examining the validity of our proposed models in a pilot-scale fluidized bed where experimental data are available, and then we will explore several large-scale applications with interest to industry, including the heat transfer mechanisms studied here as well as mass transfer between particles and the fluid due to heterogeneous chemical reactions.

### 3.5 Validation of Coarse-Grained Hard-Sphere Model for Pilot-Scale CFB Riser

The new CGHS method developed in this chapter was used to simulate a pilot-scale CFB riser of 0.304 m diameter and 16.8 m height. This fluidized bed was designed and built at the National Energy Technology Laboratory (NETL) in Morgantown, WV, and details of the experimental setup can be found at <https://mfix.netl.doe.gov/challenge-problem-iii-2010/>. This CFB has a large-enough diameter and height to rival most available rigs published in the literature, and has been operating for a couple of decades with sophisticated measuring techniques capable of gathering most data of interest to engineers. For these reasons, its experimental data were selected for a challenge problem that was posed less than a decade ago to modelers around the world challenging them to make similar predictions with their models, thus probing the reliability and maturity of CFD models developed in academia, national labs, and industry. At that time, and without the development of the coarse-grained method, this kind of problem could only be investigated with TFM (Li et al., 2012a). Now, and with the development of CFD–CGHS, this pilot-scale problem can be simulated at the particle level with a computation speed comparable or even faster than TFM. The description of this CFB riser is presented in Fig. 21 showing that the main gas flows uniformly into the riser from the bottom distributor.

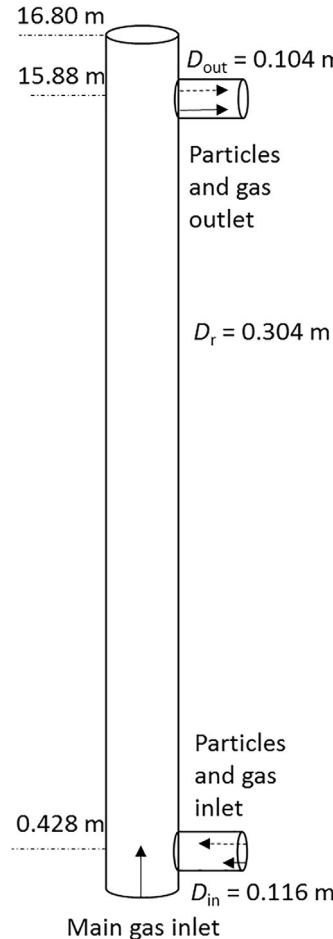


**Fig. 21** Simulation setting of circulating fluidized bed riser.

The particles, along with some aeration gas, flows into the riser at the bottom side “L” valve pipe and exit freely from the “T” type outlet near the top of the riser. The Gidaspow drag model detailed in the methods section is used in this simulation. The detailed physical and simulation parameters are listed in **Table 5**. This case was also simulated in our previous research; other detailed analysis of results can be found in a recent publication ([Lu et al., 2017d](#)).

[Fig. 22](#) shows the time-averaged void fraction (also called voidage) distributions in the riser as well as detailed particle positions near the solids main L-valve inlet. This figure shows a dense region near the walls of the bottom inlet and top outlet regions, as well as a less dense region in the middle

**Table 5** Simulation Parameters of Circulating Fluidized Bed Riser

Parameter or Property	Value
Particle diameter, $d_p$ (m)	$8.02 \times 10^{-4}$
Particle density, $\rho_p$ (kg/m <sup>3</sup> )	863
Particle spring constant, $k_n$ (N/m)	50
Parcel restitution coefficient, $e_n$	0.5, 0.14
Particle friction coefficient, $\mu$	0.6
Particle restitution coefficient, $e_t$	0.3, 0.1
Particle wall friction coefficient, $\mu_w$	0.6
Main inlet gas velocity, $u_g$ (m/s)	6.81
Main inlet gas pressure (Pa)	124 339
Main inlet gas temperature (K)	294
Side inlet gas flow rate, $Q_g$ (m <sup>3</sup> /s)	$2.37 \times 10^{-2}$
Side inlet gas pressure (Pa)	124 339
Side inlet gas temperature (K)	294
Side inlet solid mass flow rate, $M_s$ (kg/s)	14.0
Outlet pressure (Pa)	105 000
CFD grid size, $d_x \times d_y \times d_z$ (m <sup>3</sup> )	$0.016 \times 0.016 \times 0.016$
Solid time step (s)	$5.0 \times 10^{-5}$ , $1.0 \times 10^{-4}$
CFD time step (s)	$5.0 \times 10^{-4}$ , $1.0 \times 10^{-3}$

section of the riser. This “C” type distribution of solids concentration along the height of the riser is similar to that observed in the experiment. Near the bottom solids inlet, the incoming particles are moving toward the left side walls leading to an asymmetric distribution of particles. A similar asymmetric distribution can also be observed near the top region where the particles are moving toward the T-shaped outlet in the right side of the riser. For the middle sections, the distribution is more symmetric because the particles are less influenced by inlet and exit effects. The particles still exhibit a typical core-annulus flow behavior as indicated by a slightly denser region near the walls and more dilute region at the core of the riser. The instant particle distribution at time 40.0 s in the bottom region is also shown in this figure with colors referring to particle velocity. In this region, the incoming particles are

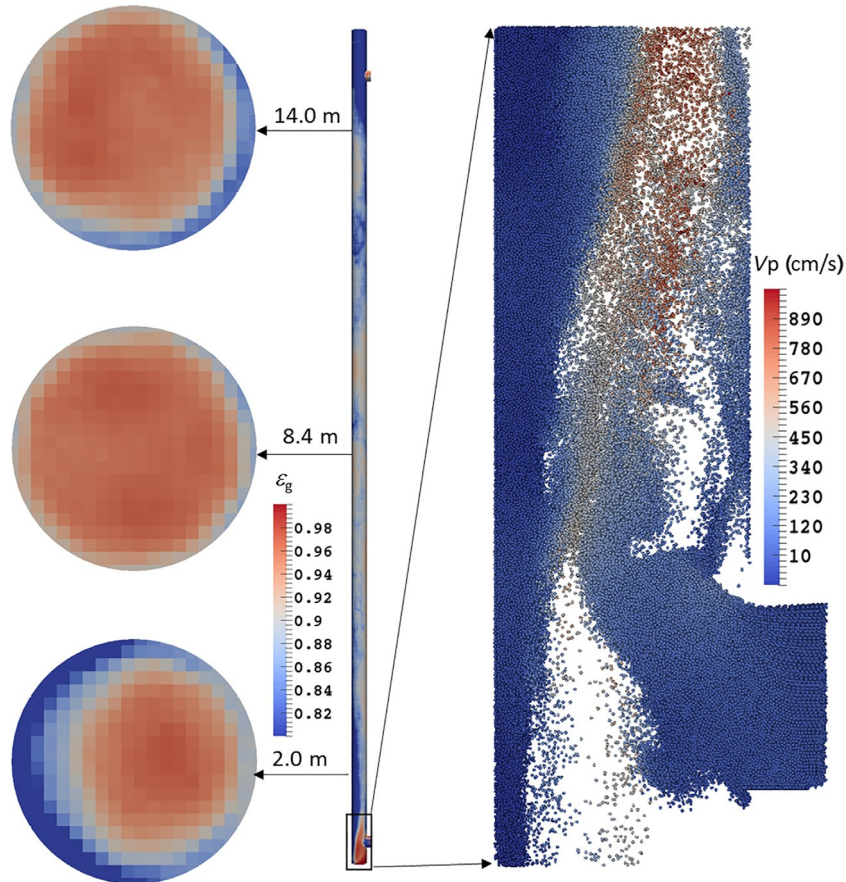


**Fig. 22** Time-averaged voidage distribution and instant particle screenshot.

colliding with the downward particles near the right-side walls and are then dragged upward by the high inlet velocity from the bottom gas inlet distributor. Incoming particles, dense falling clusters of particles, and incoming air must battle their way into the riser in a very short and crowded area at the bottom section of the riser. This complex motion of particles can be observed in Video 4 and 5 in the online version at <https://doi.org/10.1016/bs.ache.2017.12.001> included in the supplemental material.

The predicted radial profiles of time-averaged solids vertical velocity at different heights are compared with experimental measurements in Fig. 23. At a height of 6.23 and 8.88 m above the gas distributor, the fiber optical probe (FO) was used to measure the solids velocities and the high-speed particle image velocimetry (HSPIV) was used only at a height of 8.88 m to

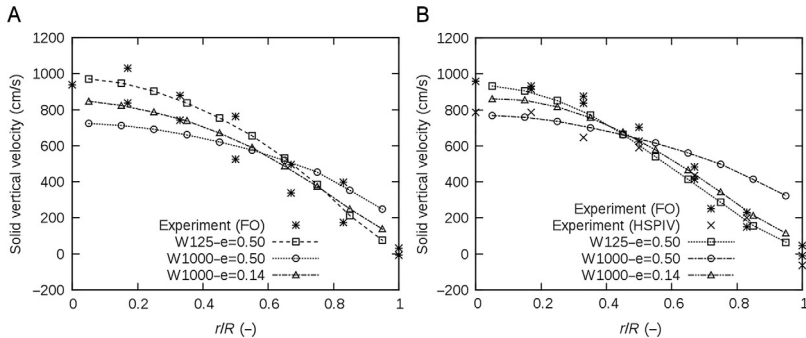


**Fig. 23** Radial profiles of solid vertical velocity at different heights. (A)  $H=6.23\text{ m}$ , (B)  $H=8.88\text{ m}$ .

compare the different measuring techniques and to better assess the experimental measurement errors and uncertainties. Here the raw experiment data are plotted directly for comparison and show that the different experimental techniques capture results that are quantitatively different. This indicates the complexity of gas–solids flow in a riser due to the different length (from particle to large clusters) and timescales that must be captured and which usually interfere with the intrusive probes required to gather measurements in an opaque system. The overall trends of these experimental measurements are, however, qualitatively similar and can be used to partially validate our simulation predictions. At a height of 6.23 m above the gas distributor, the simulation results of W125 are in good agreement with the trends captured by the experimental data and show a large upward velocity at the center of the riser and a smaller, yet still upward, velocity near the wall. However, the results obtained with W1000 for the same restitution coefficient ( $W1000 - e = 0.5$  in Fig. 23A) predict a flatter velocity distribution. These results are largely improved if a lower restitution coefficient ( $e_{cgp} = 0.14$ , calculated according to Eq. (57) with  $e_p = 0.94$ ) is adopted in the simulation. Note that a simple calculation shows the number of computational parcels for this case of W1000 is only 1/8 of the W125 case. The flat profile resulting from a coarser simulation is explained by the lower frequency of collisions occurring as the number of parcels is reduced. At a height of 8.88 m, we notice, as was noted earlier, that the two different measuring technologies reveal quantitatively different results especially in the center region where the influence on the flow field of the FO is more pronounced than in the near-wall region. A simulation result similar to the lower height is observed, showing that simulations with smaller statistic

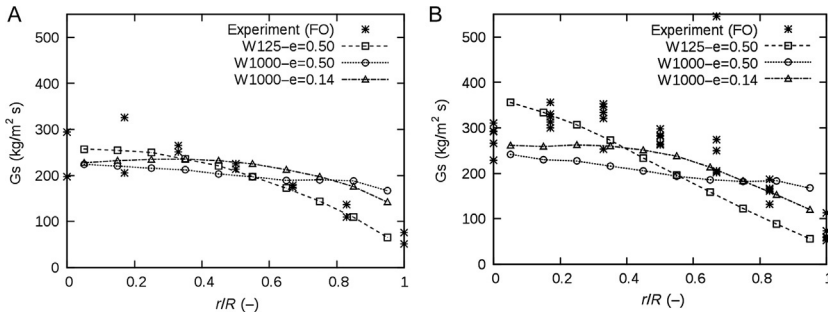


**Fig. 24** Radial profiles of solid flux at different heights. (A)  $H = 6.23\text{ m}$ , (B)  $H = 8.88\text{ m}$ .

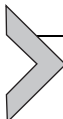
weight predict more accurate results and that reducing the restitution coefficient can help improve the accuracy of the coarse simulation.

Similar to the solids velocity profiles, the predicted radial profiles of time-averaged solids mass flux ( $G_s$ ) at two different heights are compared with the available experimental measurements in Fig. 24. The time-averaged solids mass flux is the time-average of the instantaneous solids velocity by the instantaneous solids bulk density or simply the solids volume fraction since the particles' material density is not changing in this nonreacting flow (Benyahia et al., 2007). It is important to note that the solids flux may not be obtained by the product of time-averaged solids velocity and time-averaged solids bulk density because these two flow variables (velocity and volume fraction) are usually correlated in multiphase flows. This fact is intuitive and also experimentally measurable for riser flows because regions of high solids density are expected to have low or downward solids velocity, and high solids and gas velocity are expected in dilute regions. The existence of this obvious correlation between solids velocity and density makes it incorrect to measure the time-average of these two quantities, then assume the solids flux is equal to their product (Kirbas et al., 2007). Fig. 24 shows that smaller spatial gradients are measured for the solids mass flux than those seen previously for the solids velocity profiles. This indicates that although the solids velocity in the center of the riser is much higher than the near-wall region, the solids volume fraction in the near-wall region is much higher than in the center of the riser as commonly seen for this type of core-annulus flow regime. Again, the trends predicted by our simulation compare well with experimental data, although a great amount of uncertainty exists in the experimental data at a height of 6.23 m due simply to a repeat of experiments. At 8.88 m above the gas distributor, the profile of solids mass flux near the center is slightly underpredicted, especially for the largest

parcel size, without corrected restitution coefficient ( $W1000 - e = 0.5$  in Fig. 24B). Similar to solids velocity predictions, the solids mass flux predictions show some improvement in the captured trends by lowering the solids restitution coefficient.

Generally speaking, the disagreements observed in the results for the solids velocity and mass flux can be explained by uncertainty associated with the experimentally measured solids flux as well as the fact that only the riser is simulated. Including the full CFB loop in our simulation could improve the numerical results, but this addition would introduce complexity in the geometry and would require additional computer resources. We should caution that experimental measurements of the transient solids circulation rate in this particular CFB indicated large-scale variations with large amplitudes, which will be difficult to capture numerically due to limited resources (Li et al., 2014). Other improvements to our simulation results may be obtained by refining the computational mesh for the fluid flow and using subgrid drag models that account for the unresolved effects of particle clusters smaller than the grid size. Although we showed it is possible to obtain improved predictions for large parcels, smaller parcels will always yield more accurate results. We view the use of parcels and their size as a compromise between computation speed and accuracy. The use of parcels inadvertently entrains numerical errors that can be quantified and may be acceptable to some modelers. The good news is that the CFD–CGHS is guaranteed to converge to the most accurate DEM solution as the parcel size is reduced to that of a particle. This means that uncertainties for this method can be quantified by comparing numerical results of the CGHS method with DEM. Obviously, this cannot be done in large-scale industrial reactors where DEM simulations are prohibitively expensive. In smaller systems, however, error estimation has showed that reasonably accurate results can be obtained for coarse-grained methods (Benyahia and Galvin, 2010). Thus, we suggest estimating these uncertainties in several smaller fluidized beds, then extrapolating to larger-scale systems. This is the only analysis missing in this study, and it will be conducted and published in the near future. It is important to note that such a study will involve a tremendous level of effort to estimate uncertainties associated with coarsening for different particulate flow regimes in different geometric scales. Nevertheless, such a study is important because it will provide the practitioner with a basic understanding of the errors associated with the model coarsening assumption for a particular application without having to conduct a Uncertainty quantification analysis from scratch—an endeavor which would be discouraging to most of

us. In the next section, we will tackle the most important application of this coarse-grained method, industrial reactors. This and other methods are basically useless without real-world application to industrially relevant reacting systems. By conducting industrial applications, we hope that industrial practitioners and engineers will adopt and use this new technique, among their current tools, to understand, design, and troubleshoot their industrial reactors.



## 4. APPLICATION OF COARSE-GRAINED HARD SPHERE METHOD TO INDUSTRIAL REACTORS

The steps that we are taking to demonstrate the validity of the CGHS method are like those taken to develop a new reactor following an experimental approach. First, we have shown in this chapter that CGHS is fast and accurate for small-scale fluidized beds, and we then demonstrated the same in a pilot-scale cold-flow CFB. Now we will attempt to apply this method to larger reactors of interest to industry. These steps are necessary because of increased simulation complexity and resource requirements with increased system size. However, the most important reason to follow these steps in our simulations is because of the availability of detailed experimental data. Small fluidized beds tend to be the most instrumented with data made available by researchers in academia or national laboratories who are eager to publish their results. Data in large industrial fluidized beds, however, are much more difficult to obtain, and most data published by industry are made incomplete on purpose by not giving system geometry and/or operating conditions. We conduct industrial-scale simulations because some data are still available in the literature, as we will show in this section. Industrial applications are also important to attract potential users from industry who, we hope, will start using the techniques that we develop to make a more significant impact in real-world applications. Ultimately, we also hope that industry invests more resources on computational tools, such as CFD, to accelerate their development and also to guide such development to more practical applications of interest to engineering practitioners.

Classic chemical engineering processes such as those in oil refining and in petrochemical industrial processes are investigated here. A fluid catalytic cracking (FCC) regenerator unit used to regenerate spent catalyst is simulated in this section. A detailed experimental setup is publicly available for one regenerator process located in China with uniquely rich experimental data that cover flow dynamics, heat transfer for the exothermic reactions,

and chemical concentrations of the products of coke combustion. The Methanol to Olefins (MTO) process that produces feedstocks for the petrochemical industry is also simulated with results compared with available experimental chemical conversion data. The last example that will be covered in this section relates to a rare-earth liquid–solids extraction process where experimental data are not yet available. In this last example, we show how the CFD model proposed in this chapter can be used for scaling up a counter-current fluidized bed process, which truly bridges the scales from laboratory to pilot to industrial size reactors. We hope that these examples will affirm the use of CFD in industry by those who already use it, and attract reluctant industrial practitioners to consider using CFD as an important tool for designing and troubleshooting, in addition to their preexisting arsenal of tools and expertise.

## 4.1 Simulation of a Fluidized Catalytic Cracking Regenerator

FCC is one of the most widely used and oldest conversion processes in refineries. A detailed description of the different FCC processes and their evolution in recent history is given in a previous study ([Avidan and Shinnar, 1990](#)) and only a very limited description of the regenerator process is provided here, for brevity. Through the FCC unit, heavy oils are converted into a variety of higher value light products like gasoline. The chemical reactions happen at the surface of the catalyst. A side effect of these catalytic cracking reactions is the deposited coke on the catalyst surface, which deactivates the catalyst and reduces the quality of the final products. Thus, a regenerator is designed to burn the deposited coke and restore catalytic activity. As shown in [Fig. 25](#), the spent catalyst flows into the regenerator and deposited coke is burned out with air. Then, the regenerated catalyst flows back into the riser. The heat generated by burning coke in the regenerator will be used in the riser reactor to vaporize the heavy oil feed, which is usually fed as droplets dispersed through nozzles with the help of pressurized steam. The FCC system, which consists of the reactor and the regenerator, operates as a CFB where the catalyst is constantly circulating between the reactor and the regenerator. For the reactor part, the interested reader can find in our previous research ([Lu et al., 2017e](#)) coarse-grained simulation results of the flow field and catalyst residence time distributions in a pilot-scale FCC riser. A major assumption is made in this study to decouple the effects of the riser reactor and the catalyst regenerator so the latter can be simulated separately. This assumption is reasonable when the FCC unit is at steady-state

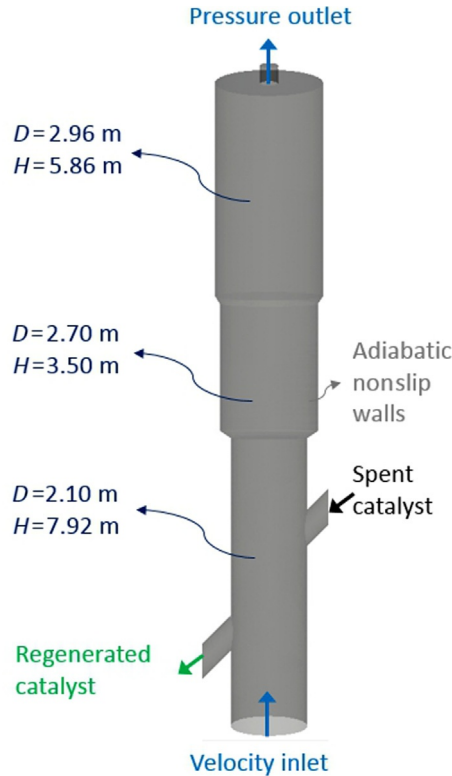


**Fig. 25** Geometry and boundary conditions of simulated regenerator.

operation, where the catalyst circulation rate is relatively constant providing low fluctuations in the regenerator inlet conditions. The case studied here is the only one, to our knowledge, available in the open literature that provides detailed experimental data to be used to further validate the model proposed in this study. The most important aspect of modelling industrial-scale reactors is to provide the computation speed of our proposed CFD–TDHS simulations; engineering practitioners will appreciate the lightning-fast execution speed of the models developed in this study, which are conducted on very accessible computer resources. Thus, the regenerator in this study is simulated at an astonishing speed of 210 s/day using only 64 cores (4 computers with 16 cores each).

#### 4.1.1 Simulation Setup

As shown in Fig. 25, a relatively small industrial FCC regenerator (70 thousand tons per year) is simulated in this study. The catalyst consists of solid

**Table 6** Correlations for the Gas Mixture Properties

Property	Corrections
Density	$\rho_g = P/RT \sum \frac{Y_{gi}}{M_{gi}}$
Viscosity	$\mu_g = 1.672 \times 10^{-6} \sqrt{T} - 1.058 \times 10^{-5}$
Thermal conductivity	$\lambda_g = 5.526 \times 10^{-5} \sqrt{T} + 0.01155$
Heat capacity	$C_g = \sum Y_{gi} C_{gi}$
Molecular weight	$M_g = 1/\sum \frac{Y_{gi}}{M_{gi}}$

particles with a diameter of 60  $\mu\text{m}$  and density of 1500  $\text{kg/m}^3$ . The gas phase is a mixture of oxygen, nitrogen, carbon dioxide, carbon monoxide, and water vapor. The gas-phase properties are calculated using the ideal gas law and summarized in [Table 6](#). The geometry of the regenerator is taken from a previous publication ([Chang et al., 2013](#)) and consists of a cylindrical fluidized bed with a diameter that varies between about 2 and 3 m and a height of more than 17 m. The details of the catalyst inlet and outlet pipelines were not provided in the publication. Also not provided were detailed information of the geometry transition between the main sections of the bed or the design of the top outlet. We estimated the spent catalyst inlet and the regenerated catalyst outlet pipe diameters as 0.7 m. The regenerated catalyst is only allowed to leave the system if the catalyst inventory in the system is greater than 4.95 tons. Effectively, a valve opens to let the catalyst leave the regenerator, but closes as the inventory in the system falls below 4.95 tons. In the simulation, the closing of this “valve” is achieved by setting the catalyst velocity to zero in the cell adjacent to the outlet represented at the bottom left side in [Fig. 25](#).

The boundary conditions are set according to available industrial data. The spent catalyst flows into the regenerator at a rate of 22.7 kg/s with a temperature of 753 K. The carbon mass fraction in the spent catalyst is 0.9% and the hydrogen mass fraction is 0.072%. The inventory in the regenerator is initialized to 4.950 tons. The outlet pressure is set to a constant value of 140 kPa. For the main air inlet, we calculated that the air flows into the regenerator at a constant superficial velocity of 0.495 m/s, at a temperature taken from reference paper set to 573 K, and at a pressure taken from the referenced book ([Lu and Wang, 2002](#)) set to 160 kPa. According to industrial data, the coke content of the regenerated catalyst is about 0.39 wt%, while that of the spent catalyst is about 0.9 wt% with a hydrogen content of 0.072 wt%. In this simulation, we assume the mass ratio of carbon to

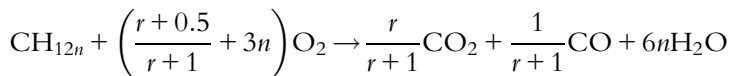
hydrogen of regenerated and spent catalyst to be the same, thus the carbon and hydrogen on the regenerated catalyst is about 0.3611 and 0.0289 wt%, respectively. Based on the spent catalyst flow rate and the carbon conversion rate, the oxygen mass flow rate required to convert that carbon is about 0.4045 kg/s, which translates to an air flow rate of about 1.7435 kg/s. Thus, a mass balance on the coke contents of the catalyst was used to calculate the oxygen/air flow rate, which was then used, along with the set temperature/pressure, to calculate the inlet air gas velocity of 0.495 m/s, based on the ideal gas law. For heat transfer, the walls are considered adiabatic. All boundary conditions used in the simulation are summarized in [Table 7](#), while those unavailable in the literature were estimated to conduct our simulation.

For initial conditions, the regenerator is separated into a dense phase up to a height of 7.9 m, while the top of the reactor consists of an initially empty freeboard. A total mass of 4.95 tons of regenerated catalyst particles are initialized in the dense phase of regenerator. The initial conditions are summarized in [Table 8](#).

As discussed previously, the CGHS method is used to simulate this industrial-scale regenerator with a drag model proposed by [Gao et al. \(2009\)](#). The numerical parameters needed to simulate the fluid flow on a computational grid with Lagrangian coarse-grained particles are summarized in [Table 9](#).

#### 4.1.2 Chemical Reaction Kinetics Model

The coke deposited on the catalyst is burned in the regenerator to recover the catalyst activity. The main chemical reactions are carbon burning and hydrogen combustion. A general scheme of this reaction can be expressed as



where  $r$  denotes the molar ratio of carbon dioxide to carbon monoxide. In this research, we use the reaction rate provided by [Chang et al. \(2013\)](#). For carbon burning, the reaction rate is given as

$$R_C = -\frac{dC}{dt} = k_c P_{\text{O}_2} C_c$$

$$k_c = 2.78 \times 10^8 e^{\frac{-161.2 \times 10^3}{RT}}$$

$$r = 5.28 \times 10^{-3} e^{\frac{34860}{RT}}$$

**Table 7** Boundary Conditions

Term	Simulation Value	Industrial Data
Bottom inlet air velocity (m/s)	0.495	NA (not available)
Bottom inlet air pressure (kPa)	160	160
Bottom inlet air temperature (K)	573	573
Bottom inlet air oxygen mass fraction	0.2320	0.2320
Bottom inlet air carbon dioxide mass fraction	0.0005	0.0005
Bottom inlet air carbon monoxide mass fraction	0.0000	0.0000
Bottom inlet air water vapor mass fraction	0.0000	0.0000
Bottom inlet air nitrogen mass fraction	0.7675	0.7675
Top outlet pressure (kPa)	140	140
Spent catalyst inlet air velocity (m/s)	0.5	NA (not available)
Spent catalyst inlet air pressure (kPa)	140	NA
Spent catalyst inlet air temperature (K)	735	NA
Spent catalyst inlet air oxygen mass fraction	0.0212	NA
Spent catalyst inlet air carbon dioxide mass fraction	0.2617	NA
Spent catalyst inlet air carbon monoxide mass fraction	0.0093	NA
Spent catalyst inlet air water vapor mass fraction	0.0416	NA
Spent catalyst inlet air nitrogen mass fraction	0.6662	NA
Spent catalyst mass flow rate (kg/s)	22.7	22.7
Spent catalyst carbon mass fraction	0.00900	0.00900
Spent catalyst hydrogen mass fraction	0.00072	0.00072
Spent catalyst temperature (K)	753	753
Spent catalyst inlet voidage	0.9	NA
Regenerated catalyst outlet pressure (kPa)	140	NA
Regenerated catalyst outlet solid mass flow rate (kg/s)	22.7	22.7
Walls momentum transfer	Nonslip	NA
Walls heat transfer	Adiabatic	NA
Walls species transfer	Zero flux	NA

**Table 8** Initial Conditions

Term	Simulation Value	Industrial Data
Dense phase air velocity (m/s)	0.00	NA (not available)
Dense phase air pressure (kPa)	140	140
Dense phase air temperature (K)	912	912
Dense phase air oxygen mass fraction	0.0212	NA
Dense phase air carbon dioxide mass fraction	0.2617	NA
Dense phase air carbon monoxide mass fraction	0.0093	NA
Dense phase air water vapor mass fraction	0.0416	NA
Dense phase air nitrogen mass fraction	0.6662	NA
Dense phase catalyst carbon mass fraction	0.003611	NA
Dense phase catalyst hydrogen mass fraction	0.000289	NA
Dense phase catalyst temperature (K)	912	912
Dense phase catalyst volume fraction	0.8794	0.8794
Dilute phase catalyst volume fraction	0.0000	0.0050
Dilute phase air velocity (m/s)	0.0000	NA
Dilute phase air pressure (kPa)	140	140
Dilute phase air temperature (K)	930	930
Dilute phase air oxygen mass fraction	0.0212	NA
Dilute phase air carbon dioxide mass fraction	0.2617	NA
Dilute phase air carbon monoxide mass fraction	0.0093	NA
Dilute phase air water vapor mass fraction	0.0416	NA
Dilute phase air nitrogen mass fraction	0.6662	NA
Dilute phase catalyst carbon mass fraction	0.003611	NA
Dilute phase catalyst hydrogen mass fraction	0.000289	NA

For hydrogen combustion, the reaction rate is given as

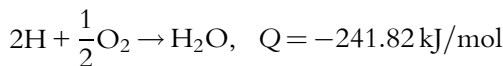
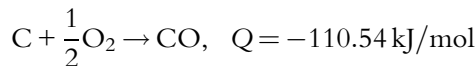
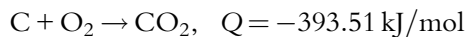
$$R_H = -\frac{dC_H}{dt} = k_H P_{O_2} C_H$$

$$k_H = 4.17 \times 10^8 e^{\frac{-157.569 \times 10^3}{RT}}$$

**Table 9** Numerical Parameters

Term	Simulation Value
Cartesian grid in $x$ direction	15
Cartesian grid in $y$ direction	90
Cartesian grid in $z$ direction	15
Convection term discrete scheme	Superbee
Linear equation solver	BICGS
Hydrodynamic residual	$1.0 \times 10^{-3}$
Temperature residual	$1.0 \times 10^{-3}$
Species residual	$1.0 \times 10^{-3}$
Gas phase time step (s)	Adaptive and no larger than $1.0 \times 10^{-3}$
Solid phase time step (s)	$1.0 \times 10^{-3}$
Coarse grained particle diameter (m)	0.048
Particle-particle restitution coefficient	0.1
Particle-particle spring constant ( $\text{kg}/\text{s}^2$ )	1000
Particle-particle friction coefficient	0.1
Particle-wall restitution coefficient	0.1
Particle-wall spring constant ( $\text{kg}/\text{s}^2$ )	1000
Particle-wall friction coefficient	0.1

The heat of different reactions is provided below



Since the reaction happens on the surface of the catalyst, the heat of the reactions is added as source terms to the particles heat balance. Physically, the heat of reaction is distributed between the catalyst and the gas with unknown proportions. This is not a major issue here because of the high rate of heat

transfer between the particles and gas phase. Also, the simulation results of the temperature distribution show that the temperature difference between the gas phase and particles is less than 2 K. Since the timescale of the coke-burning reaction is very small compared with CFD simulation time steps, the reaction speed is scaled down by about six orders of magnitude to ensure the consumed mass of each species is less than 10% of the last step's value. This is done at the end of an old time step and before any CFD calculation is conducted at the new time step. This simplification avoids the additional computation cost of using a stiff chemistry solver, which employs a very small time step to resolve the chemical reaction process.

#### 4.1.3 Results and Discussion

From the catalyst flow rate and inventory, we estimate the mean residence time to be about 218 s. Here, the simulation was conducted for 1000 s with the last 500 s used for time averaging the results to compare with industrial data. Such a long simulation time for CFD is only achieved because of the main coarsening assumption used in this current modelling approach. Some instantaneous snapshots of the numerical results are provided in this section to better understand the evolution of the gas particles reacting flow system.

##### 4.1.3.1 Hydrodynamics of Fluidized Particles in the Regenerator

The simulation successfully captured the two-phase distribution of catalysts in the regenerator and compared quantitatively well with the available industrial data. This distribution is clearly shown in Fig. 26 where the bed density near the bottom of the regenerator is much larger than the top region. The large oscillation near 8.0 m is due to the diameter of the regenerator increasing from 2.1 to 2.7 m in this region, where the transition is not very smooth. This is intentional in the design of the regenerator where the sudden expansion of the geometry causes the gas and particles to slow down and, thus, lower the entrainment of catalyst into the freeboard. In fact, the simulation results in Fig. 26 indicate no catalyst entrainment in the top freeboard region of the bed. However, the industrial data in this top region do show the existence of a small but measurable quantity of catalyst that was not captured by the simulation due to the assumption of a single particle size used to represent the particle size distribution (PSD). This PSD was not provided by the industrial data and, so, was not considered in the simulation. We must emphasize the fact that small particles, or fines, in a PSD will

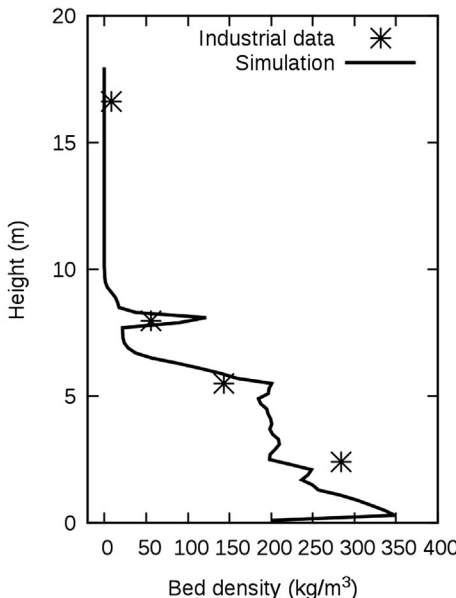


**Fig. 26** Comparison of predicted (averaged from 500 to 1000 s) bed densities with industrial data.

generally be entrained to the freeboard region necessitating the use of cyclones (both primary and secondary). We assume that the lack of fines entrainment in our simulation contributed to some of the discrepancy between industrial data and numerical results.

#### 4.1.3.2 Temperature Profiles and Heat Transfer

Through the burning of coke, the regenerator also acts as a heat exchanger to raise the temperature of the catalyst, thus increasing the cracking reaction speed in the riser. In this industrial operation, the inlet air temperature is about 573 K and increases significantly just after entering the regenerator because of the heat released from burning the coke. [Fig. 27](#) shows the instant gas-phase temperature distribution in the middle plane of the regenerator (recall that the regenerator is a 3D cylindrical system). Initially, the dense phase is set to 912 K according to industrial data (see also [Table 3](#)). Just after this initialization of the temperature field, the temperature of the right side inlet decreased sharply due to the relatively lower temperature of the inlet spent catalyst. The first few snapshots early in the simulation show the initially high temperature set in the freeboard decreasing

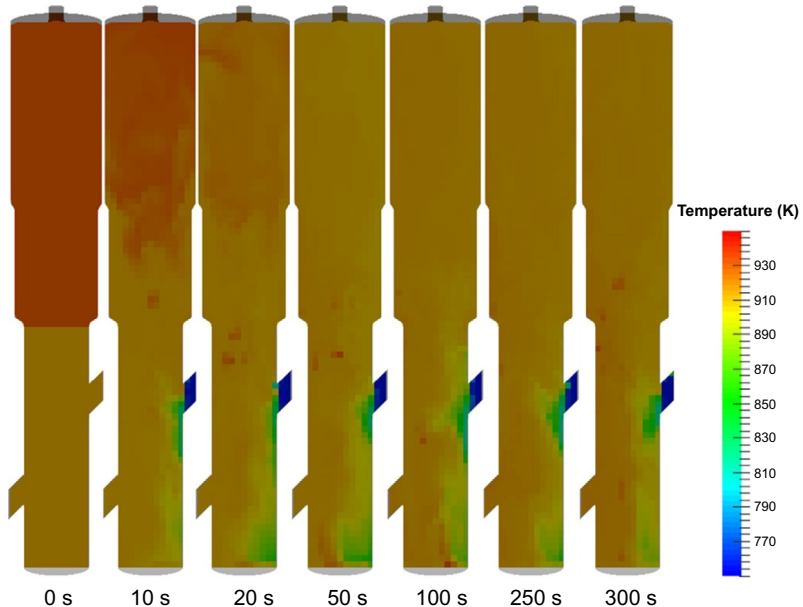


**Fig. 27** Gas temperature distribution in the regenerator.

gradually. After about 100 s of simulation time, the temperature distribution in the regenerator is stabilized, with a lower temperature in the dense bed region at the bottom of the regenerator and a higher temperature in the dilute phase.

The same phenomenon can also be observed when examining the catalyst temperature, as shown in Fig. 28. The spent catalyst flows into the regenerator at a relatively lower temperature of 753 K. After entering the regenerator, most of the spent catalyst flows down to the bottom near the wall, bypassing most of the dense bed material. This is clearly designated in the figure by the blue color of the spent catalyst changing to green as it falls near the same side of the regenerator wall as the catalyst inlet. Near the bottom region, and due to the high oxygen concentration from the main inlet air, the burning reaction rate is much faster and the released heat quickly increases the temperature of these spent catalyst particles. The temperature of the regenerated catalyst exiting the system from the lower left pipe is similar to temperature of the catalyst near the regenerator freeboard, indicating a good overall mixing of catalyst in this fluidized bed regenerator. Fig. 29 shows the time-averaged gas-phase temperature distribution along

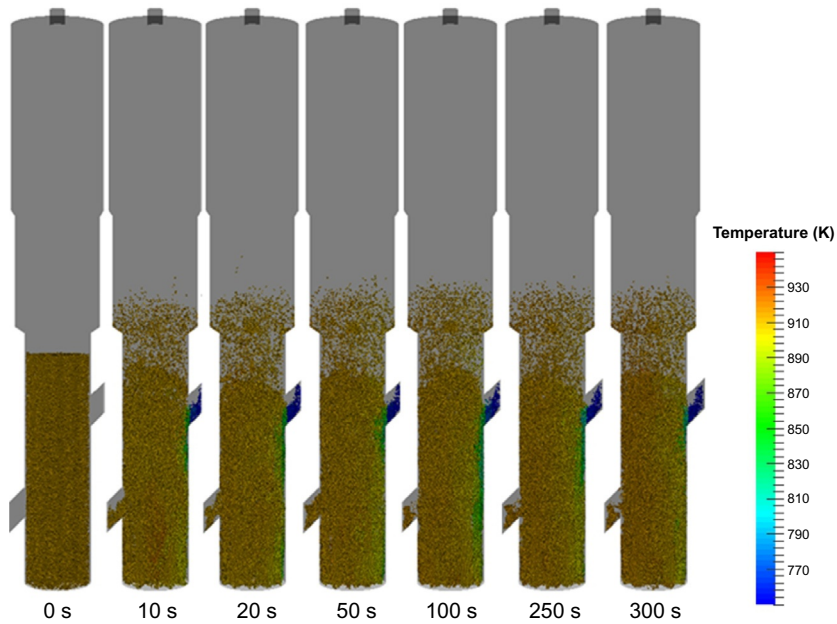


Fig. 28 Catalyst temperature distribution in the regenerator.

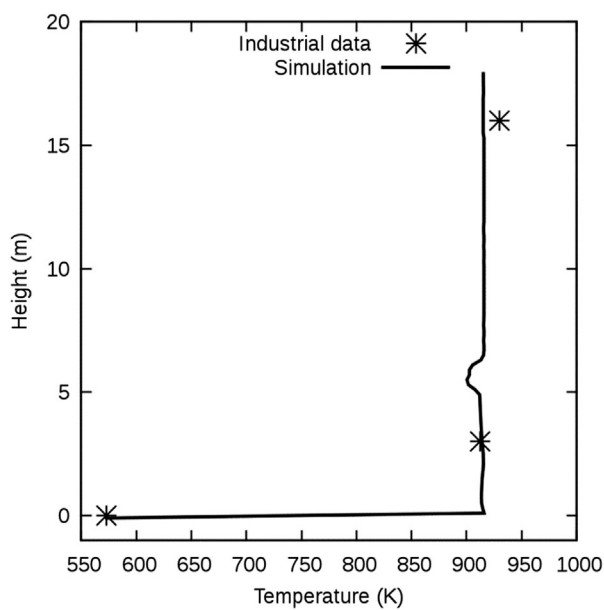


Fig. 29 Comparison of predicted temperature with industrial data.

the axial direction. Furthermore, these time-averaged results were also spatially averaged in the radial direction so that the final numerical data depended only on the height inside the reactor. It is clear that the temperature increases sharply at the bottom of the regenerator due to relatively cold air entering a very hot environment maintained by coke combustion reactions. In the bottom dense phase, the predicted temperature is about 912 K, which is same as industrial data. The small bump in the temperature profile at about the 5 m height is due to relatively cooler spent catalyst feed. At the top dilute phase, the predicted temperature is about 920 K, while the industrial data show about 930 K. Contributing to this difference are many factors, mostly related to the idealization of the model to represent the physical reality, and the most important is the lack of particle entrainment caused by a lack of PSD consideration. The errors in the simulation using a single particle size not only cause discrepancies with the bed density measurements but also, as seen here, with temperature predictions. Nevertheless, the error is only slightly more than 1.0%, which is acceptable for most engineering applications. Thus, it is reasonable to conclude that the simulation captures reasonably well the entire temperature distribution in the regenerator.

#### 4.1.3.3 Species Concentration in the Regenerator

According to industrial data, about 4.95 tons of regenerated catalyst particles are initialized in the dense phase of the regenerator with an initial coke concentration of the catalyst set to 0.39%. This initial concentration of coke can burn quickly and completely if the combustion reactions are not controlled because fresh air with a high concentration of oxygen flows into the regenerator from the main air inlet at the bottom of the reactor. Thus, the reaction kinetics are modified by simply setting the reaction rate to zero if the carbon concentration is less than 0.39%. From an industrial point of view, burning this remaining coke concentration is not possible, because it is buried inside the catalyst and not easily accessible to the highly reacting oxygen. Therefore, simply stopping the reaction at this level of coke concentration is reasonable and practical for the purpose of easily conducting our CFD simulation.

[Fig. 30](#) shows the detailed carbon mass fraction and particle flow field in the regenerator. In the dilute region (as shown in [Fig. 30A](#)), the particle velocity, as indicated by the velocity vectors attached to the parcels, is randomly distributed with a low concentration of carbon; however, some particles with high carbon concentration are still visible in this figure. At the spent catalyst inlet region (as shown in [Fig. 30B](#)), most of the spent

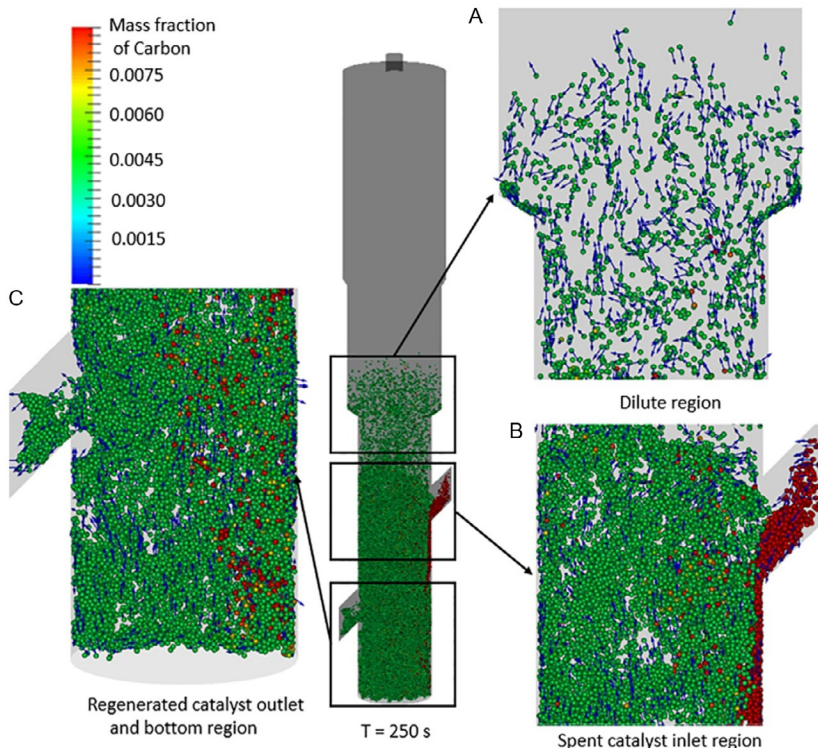


**Fig. 30** Carbon mass fraction and particle flow field in the regenerator.

catalyst particles flow down toward the bottom near the wall, bypassing most of the dense bed material. Still, fewer particles manage to diffuse into the center of the regenerator and flow upward toward the dilute region. This explains why some particles with high carbon concentration are found in the dilute region. At the regenerated catalyst outlet and bottom region (as shown in Fig. 30C), the cross-sectional plot shows bubbles (voids) surrounded by a densely concentrated bed of particles. Particles generally flow down near the walls until reaching the bottom uniform air distributor where a flow reversal occurs. It is clear that most spent catalyst flows down counter-currently on the right side of the wall against the upward flowing gas, then moves cocurrently with the gas at the core of the bed, and finally reverses flow near the top of the bed and flows downward on the left side of the wall to leave the regenerator through the regenerated catalyst outlet. This complex flow behavior is easily seen in the plot by observing changes to velocity vectors attached to the parcels, while the

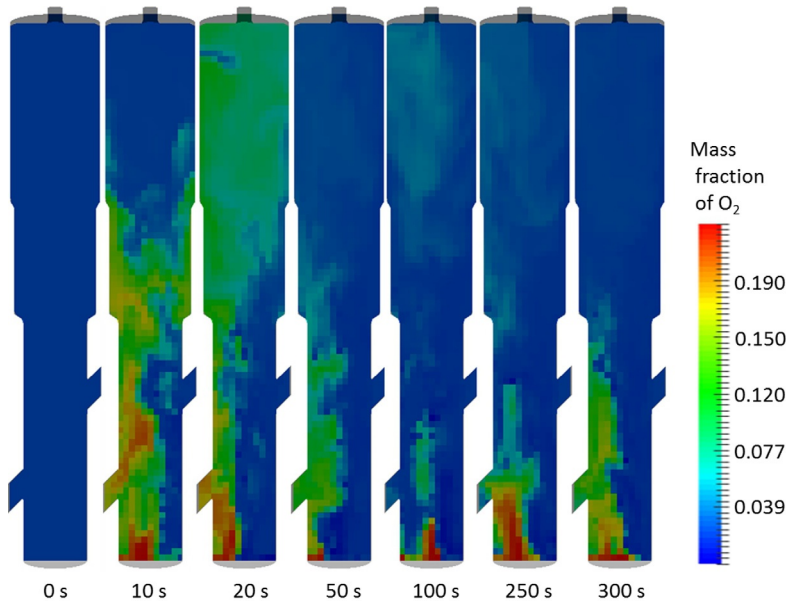


**Fig. 31** Oxygen mass fraction distribution in the regenerator.

carbon concentration acts as a tracer that helps follow the flow of fresh particles in the regenerator.

**Fig. 31** shows the oxygen mass fraction distribution in the regenerator. Initially, the oxygen mass fraction in the dilute phase of the regenerator is set to 0.0212, according to industrial data, near the top outlet. For the dense phase, the industrial data are not available and were initialized to the same value as in the dilute phase. The effect of using this value is relatively unimportant since the residence time of gas phase is only about 20 s, which is much smaller than the total simulation time. At 10 s, the oxygen flows from the bottom air distributor to the top region with the right part of the bottom region depleted of oxygen by carbon burning reaction because of the preferential flow of spent catalyst in that specific region of the reactor. At 20 s, the mass fraction of oxygen in the top dilute region is much higher than initial value because of the inexistence of reacting particles in the free-board region. At 50 s, the mass fraction of oxygen in the top dilute region reduces to a very small value. This is because oxygen, which previously accumulated from the initial conditions, flows out from the top outlet and the newly added oxygen is now consumed at the bottom dense region due to the presence of reactive particles. After 250 s, the system stabilizes and reaches a near steady-state operation.

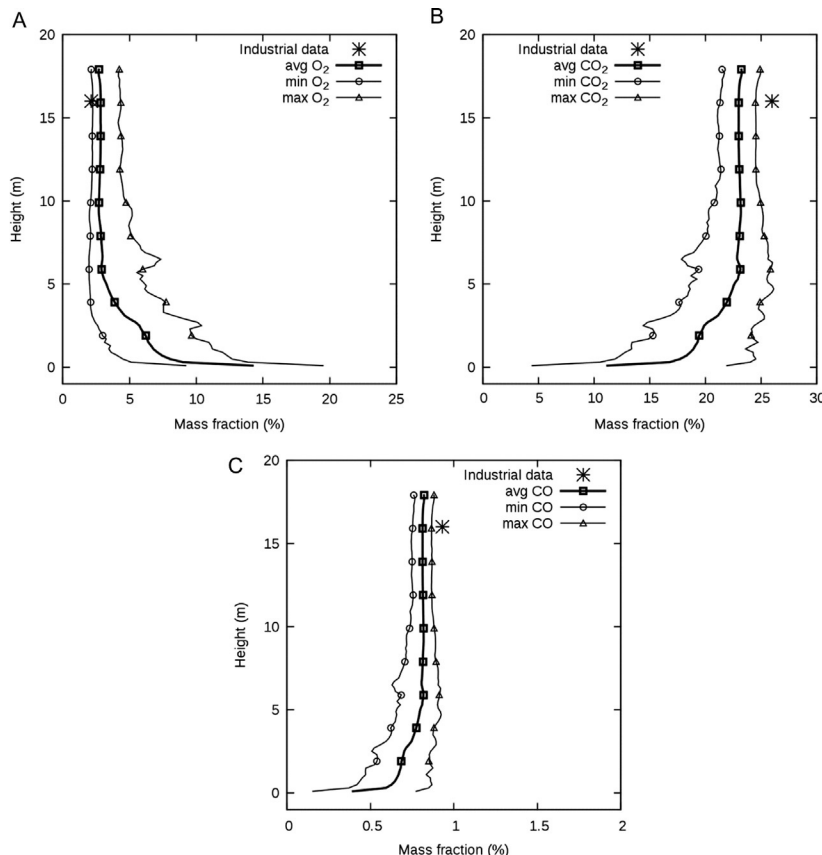


**Fig. 32** Time-averaged oxygen (A), carbon dioxide (B), and carbon monoxide (C) mass fraction distributions along the height of the regenerator.

Fig. 32 shows the time-averaged oxygen, carbon dioxide, and carbon monoxide mass fraction distributions in the regenerator where the numerical data were also space-averaged along all radial positions so that there is a dependence on height only. The data were time-averaged using only the last 500 s of simulation from 500 to 1000 s as previously mentioned. Since it is not known how or where exactly the experimental data were taken, we decided to plot the minimum, maximum, and averaged values of these chemical species mass fractions along the height of the reactor. The predicted values compare well with available industrial data. In the dense region, the oscillation of mass concentration is larger than that in the dilute region. This is because, in the dense region, the fluidized bed is in turbulent fluidization regime, which leads to a highly dynamic flow field. A longer time-averaging period will

reduce such oscillations and usually results in smoother profiles. For carbon dioxide, the predicted value of the mass fraction at the dilute phase is about 23%, while the industrial data are about 26% leading to a relative error of about 11%. For carbon monoxide, the predicted mass fraction value at the dilute phase is about 0.82%, while the industrial data are about 0.93% leading to a relative error of about 12%. Notice that the concentration of carbon dioxide and carbon monoxide mass fractions was not plotted in the same way as oxygen in Fig. 31. This is because of the similarity of these plots where the concentrations of carbon dioxide and carbon monoxide can easily be obtained from that of oxygen by simply reversing the color plots (blue becomes red and vice versa). Thus, we chose not to plot these additional contour profiles for the sake of brevity.

The simulation of the FCC regenerator process shows that our newly developed CFD–TDHS approach can easily simulate this relatively complex reactor. The ease of simulation stems from two important facts: (1) the simulation's extremely fast execution speed, as mentioned earlier, is crucial to obtaining meaningful results in just few days; (2) this method is reasonably accurate even though the simulation is relatively coarse, as indicated by the size of the parcels, compared to our previous small-scale simulations. In fact, the use of numerical parcels that contain a large number of physical particles is the only reason why conducting such simulations is even possible. To obtain more accurate simulation results, the interested researcher can simply lower the coarseness of the simulation by including fewer particles in a parcel. As mentioned previously, the model errors associated with the main assumption of coarsening particles will be systematically studied in the near future.

## 4.2 Simulation of a Methanol to Olefins Reactor

MTO is an autocatalytic reaction that converts coal or natural gas-based methanol to valuable olefins, which are widely used in petrochemicals and relevant downstream processes (Tian et al., 2015). The design of MTO units is similar to the FCC process, where an online catalyst regenerator is operated with a main reactor. The difference is that the MTO reactor is operated under a bubbling or turbulent fluidization regime with a catalyst residence time much larger than the modern FCC system. This leads to a substantial computation cost to simulate the MTO reactor. In this section, a pilot-scale MTO reactor, where experimental data are available, is simulated with CFD–CGHS. To estimate the coke fraction on the catalyst,

the system is first simulated with 0D simulation and then with 3D simulation. While a full 3D simulation tries to mimic the details of the actual system geometry, a 0D simulation is what chemical engineers usually call a perfectly mixed continuous stirred tank reactor where spatial gradients of flow variables (such as velocity, pressure, etc.) are nonexistent. We traditionally use 0D simulations to quickly verify/debug code written for complex chemical reaction kinetics without the addition of complex flow dynamics. Here, however, 0D simulation results can be used to obtain a good initial guess for 3D simulations as well as for comparison with 3D results to assess the effects of the flow dynamics on the reactor's overall performance. As far as the computation speed is concerned, the full 3D simulation runs at about 122s/day using 128 cores (8 computers with 16 cores each), while the simplified 3D simulation (explained in the next section) runs at about 2200s/day using 16 cores on a single computer. As mentioned previously in the FCC regenerator section, the speed of execution of these simulations is this method's main attribute, which we think is key to solving industrial problems.

#### 4.2.1 Simulation Setup

The simulation setup of an MTO reactor is shown in Fig. 33A. The solid arrow lines indicate the flow directions of the gas phase, and the dash arrow lines show the flow directions of the catalyst. In this reactor, the main reactants, consisting of methanol and steam, flow into the reactor from the bottom distributor with a total mass flow rate of 27 kg/h with the mass ratio of methanol to steam set to 2:1. Another stream of steam enters the reactor with a flow rate of 0.12 kg/h from a lift tube connected to the bottom of the reactor. The catalyst is added into the reactor through a pipeline with a flow rate of 8.8 kg/h. These catalytic reactions produce coke deposits on the surface of the catalyst reducing its activity. The spent catalyst is then discharged through a central orifice on the distributor to the lifting tube and then transported to the regenerator. To maintain the same bed height as in the experiments, the inventory of the catalyst in the reactor is set to 9.0 kg and maintained by controlling the spent catalyst discharge rate using the same method discussed previously in the simulation of the FCC regenerator. The actual length of the lifting tube is 3.35 m, while only the top 0.05 m is simulated to save computer time. The EMMS drag model, described in the methods section, has been validated in previous TFM simulation study (Lu et al., 2016b) of the same reactor and is used in this simulation as well. Other simulation parameters are listed in Table 10.

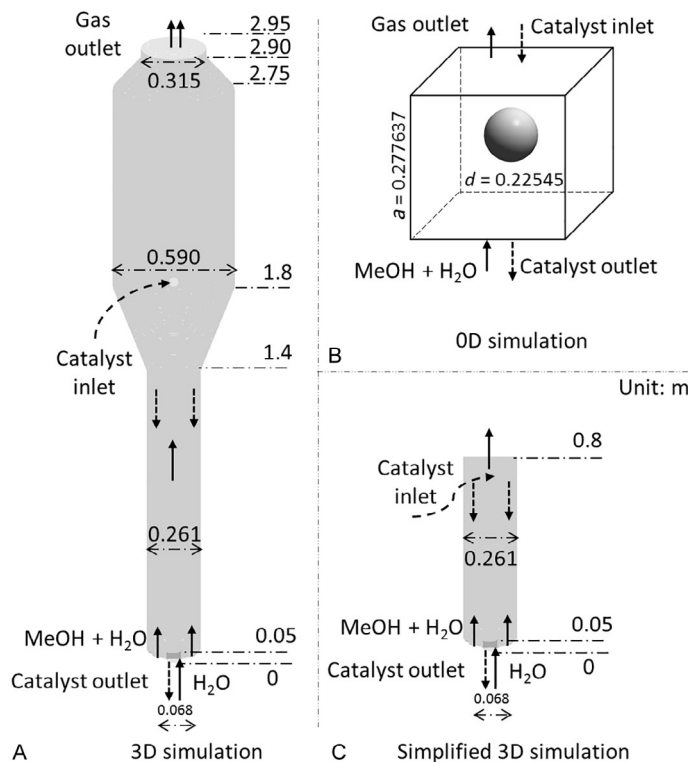


**Fig. 33** Simulation setups of the MTO reactor.

**Table 10** Simulation Parameters of the MTO Reactor

Properties	Values
Particle diameter, $d_p$ (mm)	0.097
Parcel diameter, $d_{CGP}$ (mm)	4.85, 9.7
Particle density, $\rho_p$ ( $\text{kg}/\text{m}^3$ )	1500
Coke mass fraction in inlet catalyst	0.02
Restitution coefficient, $e$	0.1
Friction coefficient, $\mu$	0.1
Spring constant, $k_n$ (N/m)	100
Gas density, $\rho_g$ ( $\text{kg}/\text{m}^3$ )	0.4288
Gas Viscosity, $\mu_g$ (Pas)	$2.43 \times 10^{-5}$
CFD grid size, $d_x, d_y, d_z$ (mm)	20, 20, 20
Gas phase time step (s)	$5 \times 10^{-3}$
Solid phase time step (s)	$1 \times 10^{-4}$

In this reactor, the residence time for the catalyst is more than 1 h, while the gas phase can flow through the reactor in several seconds. To save computational resources, the reactor is initialized with 9.0 kg of catalyst in the bottom region of the bed. With this initial condition, the hydrodynamics of this reactor can reach a stable state within a minute of simulation time; however, the coke deposit on catalyst requires a much longer time due to the slow reaction kinetics of coke production. Thus, and to save computational resources, we first carried out a cold full 3D simulation, shown in Fig. 33A, with a focus only on the hydrodynamics. After that, the volume of the main reaction region and averaged solid volume fraction is estimated based on the bed height obtained from this simulation result. Then, a virtual 0D reactor with only one CFD cell is constructed, as shown in Fig. 33B, and is assumed to be a cube with a length of 0.277637 m (this value will be explained later) where all the solid particles are lumped into a single parcel with a diameter of 0.22545 m. The inlet gas flow rate, catalyst flow rate, and species fractions are same as those used in full 3D simulation. The outlet flow rate is also the same as the inlet flow rate to maintain a constant mass in the reactor. However, the species fractions at the outflow are set to the same value of the only computational cell in this 0D reactor. The gas and particle velocities are set to zero and only the species transfer equations are solved. This 0D simulation can estimate the averaged coke deposit on catalyst quickly and was used previously for this purpose (Lu et al., 2016b). However, this simple 0D simulation cannot provide the coke deposit on different catalyst particles, which is a good metric to measure the mixing state of the catalyst in the reactor. To eliminate some of the major assumptions in the 0D simulation while still maintaining an acceptable computation speed, the reactor is also simulated with a simplified geometry as shown in Fig. 33C. In this simplified 3D simulation, only the bottom part of the main reactor is simulated. Since most of the particles are in this region, the uncertainties introduced through this simplification are very small compared to errors introduced in the 0D simulation. The major advantage lies in the computation speed of this simplified geometry, which will be much faster than the full 3D geometry due to the drastic reduction in the number of CFD cells.

#### 4.2.2 Chemical Reaction Kinetics Model

The lumped reaction kinetics for MTO is used (Lu et al., 2016b). In this reaction model, seven parallel reactions are considered and the formation

**Table 11** MTO Reaction Constant

Components	Rate Constant, $k_i$	Parameter, $\alpha_i$
CH <sub>4</sub>	0.00300	0.0649
C <sub>2</sub> H <sub>4</sub>	0.12463	0.1008
C <sub>3</sub> H <sub>6</sub>	0.16212	0.1996
C <sub>3</sub> H <sub>8</sub>	0.03467	0.4060
C <sub>4</sub> H <sub>8</sub>	0.07910	0.2924
C <sub>5</sub> H <sub>10</sub>	0.04895	0.3495
Coke	0.05859	0.38586

rate of each lump,  $R_i$  ( $i = \text{CH}_4, \text{C}_2\text{H}_4, \text{C}_3\text{H}_6, \text{C}_3\text{H}_8, \text{C}_4\text{H}_8, \text{C}_5\text{H}_{10}$ , and coke) is given by

$$R_i = n_i k_i \varphi_i C_{\text{MeOH}} M_i$$

where  $n_i$  is the stoichiometric number;  $C_{\text{MeOH}}$  is the methanol concentration with a unit of mol/L;  $M$  is the molar weight (g/mol), which for coke is set to 84 g/mol;  $k_i$  is the reaction rate constant (L/g<sub>cat</sub>/s); and  $\varphi_i$  is a deactivation function defined by

$$\varphi_i = \frac{1}{1 + 9e^{2(w_{\text{coke}} - 7.8)}} e^{-\alpha_i w_{\text{coke}}}$$

$w_{\text{coke}}$  is the percentage of coke in the catalyst with a unit of g/100 g<sub>cat</sub>. The rate constant  $k_i$  and  $\alpha_i$  are listed in [Table 11](#).

#### 4.2.3 Results and Discussion

[Fig. 34A](#) shows the time-averaged gas volume fraction in the whole reactor. Most of the particles are in the bottom section of the reactor occupying a height of about 0.4 m from the gas inlet distributor. The top regions of the reactor, including the top sedimentation section, are almost empty. Based on this observation, the volume of the 0D reactor is set to 0.021401 m<sup>3</sup>; in the simplified 3D simulation only a reactor of double this height (0.8 m) is simulated. [Fig. 34B](#) shows the instant particle distribution colored by vertical velocity with a 90% transparency to allow the observation of the flow structures that are otherwise invisible inside this opaque system. This figure indicates a dense region present near the bottom distributor and a relatively dilute turbulent region with clusters and bubbles above that. [Fig. 34C](#) shows the particle flow field, or flow patterns, at the middle plane

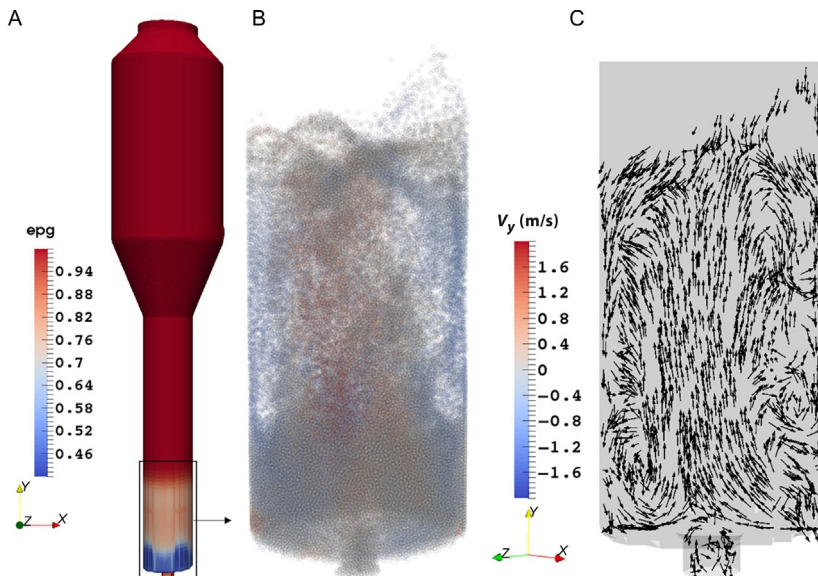


**Fig. 34** Time-averaged void fraction (A), instant particle distribution (B), and flow field (C) in MTO reactor.

along the  $Z$  direction. The general flow patterns of the solids catalyst are as follows: the fresh catalyst is dropped into the top region of the fluidized bed and collides with the upward moving particles and gas. Then, the catalyst is transported to the near-wall region by the agitating effect of bubbles and moves downward to the bottom dense phase. In this dense region, the catalyst contacts the inlet gas and is dragged to the center of the bed. Through the significant agitation effects of bubbles inducing large-scale turbulence, the particles are well mixed, and this explains why we can attempt to use 0D simulation results to cheaply and accurately estimate the coke deposit.

After the initial hydrodynamic investigations presented earlier, the reactor was simulated for 8 h of flow time with chemical reactions using the simplified 0D geometry. Since the coke mass fraction on the regenerated catalyst is 2.0% (from industrial data), the 0D simulation is carried out with initial coke mass fraction of 2.0%. As shown in Fig. 35, the predicted coke accumulation result obtained with the 0D simulation is about 5.6%, which is slightly less than experimental data of about 6.0 wt%. However, the simulation speed in this simplified case is extremely fast, and the computation results are obtained within just few minutes on a single processor. This indicates that the 0D simulation method can be used as a tool to quickly and cheaply estimate equilibrium or steady-state chemical species concentrations

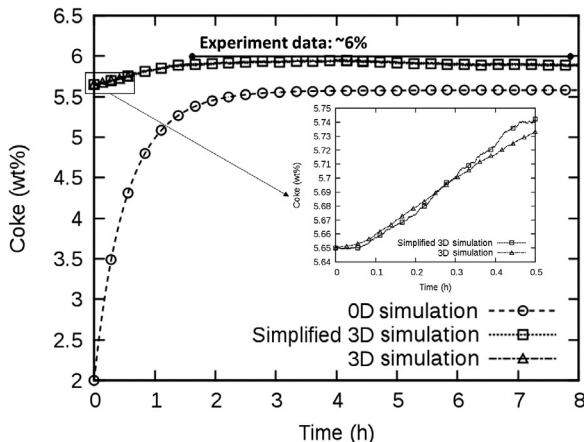


**Fig. 35** Spatial-averaged coke mass fraction in MTO reactor.

in this bubbling fluidized bed. Based on the 0D simulation results, the initial coke mass fraction for 3D simulations is set to 5.65%, which is in the range of the 0D simulation and experimental data. Because of the significant computational requirements, the full 3D simulation is only carried out for 0.5 h, while the simplified 3D simulation is carried out for the full 8 h of total flow time. The results indicate that the simplified 3D simulation predicts a very similar profile to that obtained with the full 3D simulation (at least in the first 0.5 h), indicating that this simplification to the full 3D geometry is reasonable. The predicted coke mass fraction of the simplified 3D simulation is about 5.90%, which is in better agreement with experiment data compared to the 0D simulation.

Apart from the averaged coke mass fraction, the 3D simulation can also reveal detailed coke fraction statistics on the catalyst particles. Fig. 36 compares the coke fraction distributions and cumulative distributions at different simulation flow times. The initial trend shows a coke mass fraction value where a sharp change, or discontinuity, in the cumulative distribution occurs, indicating a large fraction of catalyst with a coke mass fraction equal to this value. After 0.5 h of simulation time, this discontinuity occurs at about 0.4, which represents 40% of newly added regenerated catalyst, since any catalyst with a coke concentration less than 5.65% was freshly added from the inlet rather than initially present in the reactor. As the simulation progresses, the curve becomes smoother, which means that most of the initial catalyst was discharged from the reactor. After 8.0 h of simulation time, even the distribution curve becomes very smooth with a maximum frequency occurring at about 7.5% of the coke concentration.

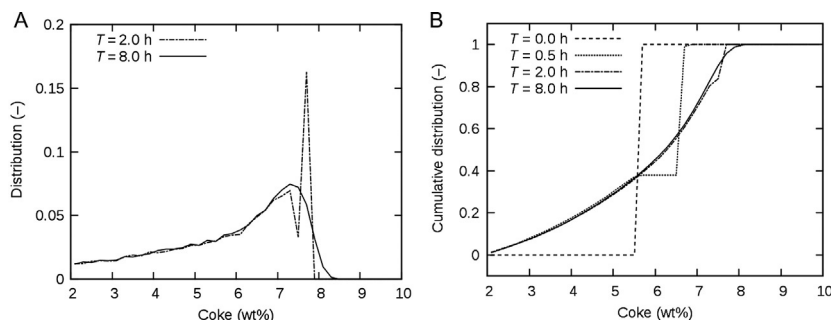


**Fig. 36** Coke mass fraction distributions in the MTO reactor at different times. (A) Coke distribution and (B) coke cumulative distribution.

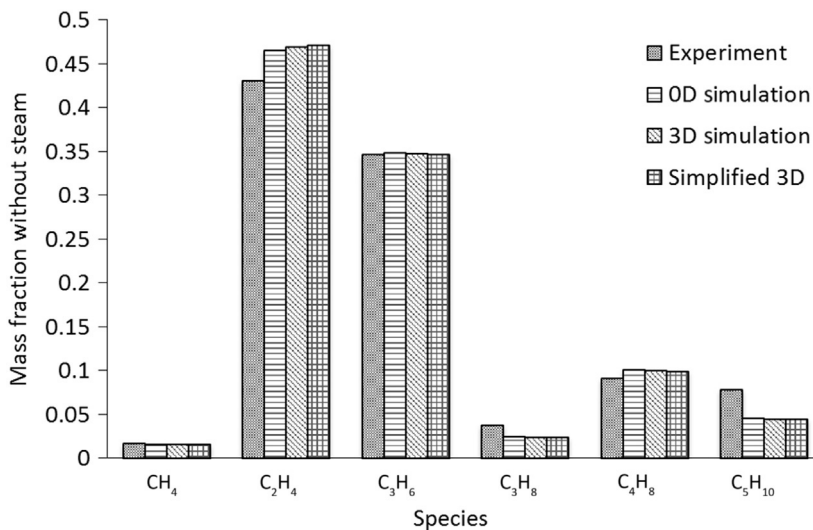


**Fig. 37** Species mass fraction of the MTO process.

The mass fractions of different species in the products measured at the exit of the reactor are compared in Fig. 37. This figure indicates that the simulations using different assumptions can reasonably capture the experimental findings except for a slight over prediction of ethylene and underprediction of  $\text{C}_5\text{H}_{10}$ . The simulated light olefins ( $\text{C}_2\text{H}_4$  and  $\text{C}_3\text{H}_6$ ) account for about 81.2% of the total products, while the experimental results show a value of about 77.6%. This indicates the high selectivity of the catalyst used in MTO reactions.

The simulations of the two industrial reactors for FCC and MTO reactions conducted so far indicate that the CFD–CGHS method is efficient and reliable for these types of gas–solids reactors. Next, we will tackle a different type of multiphase flow reactor that deals with liquid–solids reactions. Unlike previous reactions, this liquid–solids flow involves an aqueous ion exchange reaction that will demonstrate the value of our newly developed technique to the widest possible industrial applications.

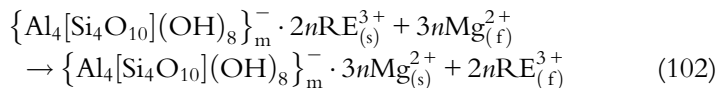
### 4.3 Simulation of a Rare Earth Elements Leaching Reactor

Rare earth elements (REEs) are widely used in high-technology products such as catalysts, lasers, cell phones, medical devices, and other applications. The first step of REE production is extracting the valuable REEs from ores, followed by a solution concentration and crystallization step and other purification steps. The traditional in-situ leaching of ores leads to severe environmental damages. A project we are currently working on involves the extraction of REE from coal by-products, such as clays from coal excavation and ash from coal burning/gasification, to minimize the environmental effects of coal mining and maximize its profits. A new counter-current leaching reactor is virtually designed using CFD to provide an environmentally friendly way to produce REEs. The leaching reaction is basically an ion exchange reaction, and the chemical reaction kinetics used in this research are taken from a published paper ([Xiao et al., 2015](#)). In this section, the implemented chemical reaction model is first validated against published experiment data using a small bubbling fluidized bed. After that, a small lab-scale counter-current reactor is simulated under different operating conditions to optimize REE production. Finally, this laboratory-scale reactor is virtually scaled up to both pilot- and industrial-scale reactors. The computation speed of the simulation conducted for the largest industrial-scale reactor is about 2700 s/day on a single computer node with 16 cores. This proves the ability of this newly developed technique to tackle not only industrial-scale problems but also their optimization using a rigorous CFD approach.

#### 4.3.1 Validation of Chemical Reactions

The leaching process to extract ion exchangeable REE can be carried out with an acidic reagent. For example, solid phase REE is extracted from

REO (rare Earth ore) with magnesium sulfate solutions used as lixiviation agent. The chemical reaction mechanism is as follows ([Xiao et al., 2015](#)):



where s and f are solids and fluid phases, respectively. In this reaction, the aqueous phase cations replace REE sites with the REE extracted from REO and dissolved into an aqueous solution. The REE leaching with the ion exchange reaction can be explained as multiple steps using the shrinking core model. First, the reactive cations in the aqueous solution approach the REO surface by diffusion through a liquid boundary layer surrounding the REO particles. After the ions reach the surface of the REO, they diffuse into the porous solid particle until reaching the REE sites. Here, the ion migration inside the solid phase is called inner diffusion, while outer diffusion occurs just outside the particle surface. Once the cations encounter the REE, the ion exchange reaction occurs and the ammonium ions combine with the hosting minerals. During the ion exchange reaction, the REE core shrinks, while the REO particle maintains its initial spherical shape. We assume in this study that the REO particle shape and density remain constant during the ion exchange due to the low concentration of REE, which is assumed to be in the order of 1000 ppm. Finally, the extracted REE ions diffuse out to the acidic reagent. Here, the multiple step reactions are specified as (1) outer diffusion, (2) inner diffusion of ammonium, and (3) ion exchange reaction. Generally, and also proved by experimental data ([Jun et al., 2010](#); [Xiao et al., 2015](#)), it is known that the reaction speed of ion exchange is faster than the inner diffusion phenomenon during REE extraction. Therefore, it can be safely assumed that the reaction rate is mainly controlled by the diffusion speed of reactive ions. Thus, the inner diffusion controlled shrinking core model was demonstrated to best describe the reaction mechanism by the following equations ([Xiao et al., 2015](#)):

$$1 - \frac{2}{3}\alpha - (1 - \alpha)^{2/3} = kt \quad (103)$$

$$\alpha = 1 - \left( \frac{r_c}{R_p} \right)^3 \quad (104)$$

$$k_{\text{exp}}(\text{1/min}) = \frac{0.011}{R_p(\text{mm})^{1.217}} \exp \left( -\frac{9480}{RT} \right) \quad (105)$$

where  $\alpha$  is the leached fraction,  $k_{\text{exp}}$  is the chemical reaction rate from experimental measurements,  $r_c$  is the radius of the shrinking core,  $R_p$  is the

constant radius of REO particle and  $R$  is the universal gas constant, and  $T$  is the reaction absolute temperature. In this model, the influence of  $\text{Mg}^{2+}$  concentration must be considered and the reaction rate is calculated as

$$k(1/\text{min}) = \frac{C_{\text{Mg}}}{C_{\text{Mg,exp}}} k_{\text{exp}} \quad (106)$$

where  $C_{\text{Mg,exp}}$  and  $C_{\text{Mg}}$  are the  $\text{Mg}^{2+}$  concentration in experiment and simulation, respectively. Since the experiment is carried in a fast stirred 500 mL container with ample  $\text{MgSO}_4$  solution, the system is considered perfectly mixed and the  $\text{Mg}^{2+}$  concentration is assumed constant.

To validate our implementation of the reaction kinetic model in MFIX, the REE extraction process is simulated in a small liquid–solids fluidized bed. The simulation parameters are listed in [Table 12](#). In the experiment ([Xiao et al., 2015](#)), the particle size is in the range of 0.45–0.60 mm. Since the detailed PSD is not given, a single particle size is used in each simulation.

**Table 12** Simulation Parameters of Small Liquid–Solids Fluidized Bed Properties Values

Particle diameter, $d_p$ (mm)	0.45, 0.6
Statistic weight, $W$	250, 500, 1000
Particle density, $\rho_p$ (g/cm <sup>3</sup> )	1.34
REE mass fraction in particle	0.00102
$\text{NH}_4$ mass fraction in particle	0.0
Ash mass fraction in particle	0.99898
Restitution coefficient, $e$	0.7
Friction coefficient, $\mu$	0.1
Liquid density, $\rho_l$ (g/cm <sup>3</sup> )	1.0
Viscosity, $\mu_l$ (g/cm/s)	0.01
REE mass fraction in liquid	0.0
$\text{NH}_4$ mass fraction in liquid	0.002730
$\text{SO}_4$ mass fraction in liquid	0.007346
$\text{H}_2\text{O}$ mass fraction in liquid	0.989924
Fluidized bed dimensions, $L_x$ , $L_y$ , $L_z$ (mm)	80, 320, 80
CFD grid size, $d_x$ , $d_y$ , $d_z$ (mm)	10, 10, 10

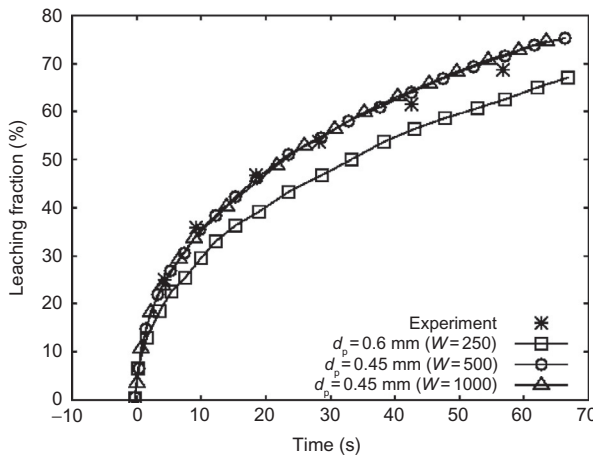


**Fig. 38** Comparison of REE leaching fraction obtained experimentally and with simulation.

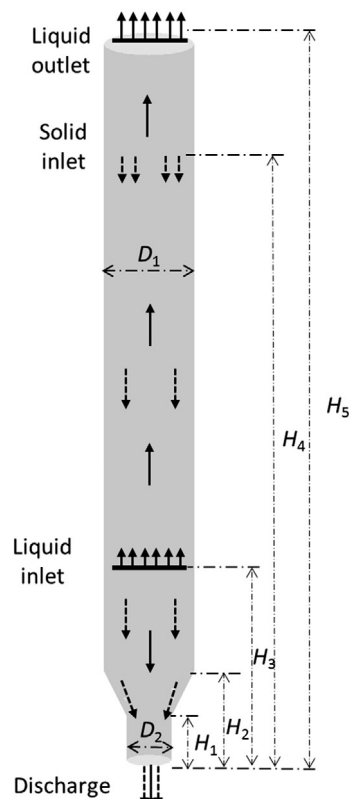
In these simulations, the Wen—Yu drag model, described in the methods section, is used. Also, to investigate the influence of parcel size on simulation results, different statistic weights are adopted in our calculations.

Fig. 38 compares the REE leaching fraction between experimental findings and simulation results using different statistic weights and particle diameters. Although the experimental data are from a continuously stirred three-necked flask, the simulation results compare well with experimental data because a fluidized bed is a fully mixed reactor, especially for a homogeneous liquid–solids flow that is unlike the heterogeneous gas–solids flow systems studied previously in this chapter. The results are also insensitive to different statistic weights considered in this study. This proves that the implemented chemical reaction mechanism can accurately capture the REE leaching reaction. Also, the simulation with a diameter of 0.45 mm compares well with experimental data. This indicates that, in the experiment, most of the particles have a diameter of 0.45 mm.

#### 4.3.2 Simulation of a Small Counter-Current Reactor Under Different Operating Conditions

Recent research (Moldoveanu and Papangelakis, 2016) shows that column leaching provides a more efficient alternative to the batch process and constitutes an important step toward simulating the in-situ leaching of REEs. However, this system is limited by its liquid flow rate through a densely packed bed. Kwaak (1979, 1992) investigated a leaching process in a counter-current

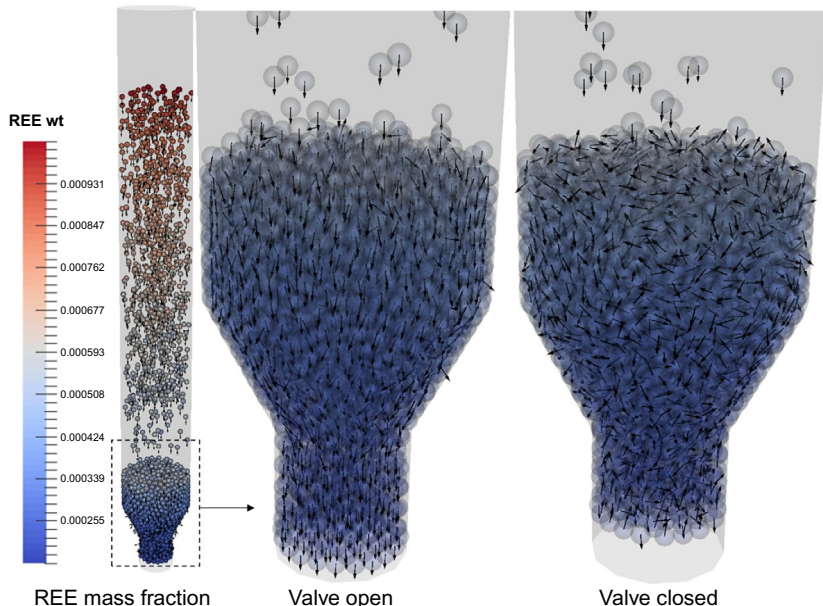
fluidized bed. The particles are added from the top of the reactor and fall counter-currently against a rising stream of liquid into the fluidized leaching section. Fresh leaching liquid enters the system through special sprayers located near the bottom of the reactor. Below the liquid inlet region, the solids are discharged from the bottom with an automatically controlled valve. In our simulation, the inlet flow is simulated with point sources to avoid considering complex inlet designs, and the closing and opening of the valve are controlled by the total number of particles in the reactor, as done in the two industrial cases from the previous sections. A counter-current fluidized bed capable of leaching REEs shown in Fig. 39 was simulated using coarse-grained CFD-DEM with different operating conditions, listed in Table 13. As in the



**Fig. 39** Schematic of counter-current leaching reactor. Modified from Lu L, Yoo K, Benyahia S: Coarse-grained-particle method for simulation of liquid–solids reacting flows. Ind Eng Chem Res 55:10477–10491, 2016a with permission for the reprinted content. Copyright (2016) American Chemical Society.

**Table 13** Simulation Parameters of Counter-Current Leaching Reactor

Case	Base	Recycle50	L36	L36S36
Liquid flow rate, $L$ (kg/h)	72	72	36	36
Solid flow rate, $S$ (kg/h)	18.41	18.41	18.41	36.82
Liquid recycle fraction (%)	20	50	20	20

**Fig. 40** REE mass fraction and particle flow field.

previous simulation, the Wen—Yu drag model is also used here. Other parameters are the same as the previous simulation of fluidized bed in [Table 12](#).

[Fig. 40](#) shows several snapshots of the simulated results and reveals the flow behavior in different sections of this counter-current reactor. It shows that most of the REEs are extracted out as the particles are moving toward the bottom of the reactor. Similar to Kwauk's experimental observation ([Kwauk, 1979, 1992](#)), the reactor has a top dilute region and bottom dense region. When the inventory of particles in the reactor is larger than a user-defined value, the bottom valve will open and the leached particles can be discharged. After this discharge, the valve is closed again by setting the particles' velocities to zero in the adjacent cells to the outlet patch. A complex flow field showing particles agitation is observed when the valve is closed. This helps mix the

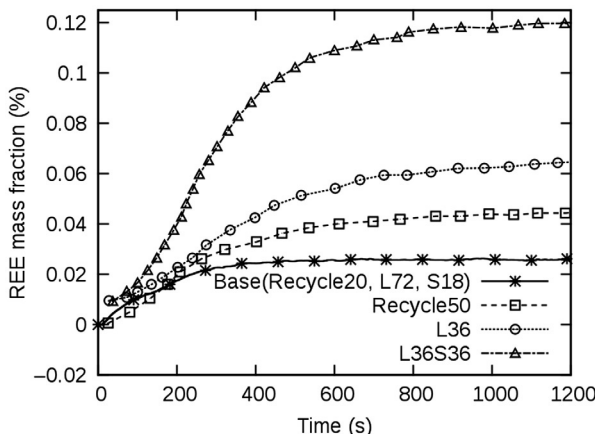


Fig. 41 REE mass fractions in the top outlet liquid under different operating conditions.

particles and is beneficial to REE leaching, which continues even in this bottom section near the outlet.

The REE mass fractions in the top liquid outlet under different operating conditions are compared in Fig. 41. For the base case, 20% of the top outlet liquid stream is recycled into the liquid inlet, and the outlet REE mass fraction reaches a stable profile after about 300s. However, the outlet REE mass fraction is very small, leading to high energy consumption in the following concentration process. Thus, we modified the operating conditions to increase the final REE mass fraction in the outlet liquid stream. First, the recycled fraction is increased to 50%. Under this condition, the mass fraction of REE is increased to more than 0.04%. According to mass balance, there is ample  $Mg^{2+}$  in the liquid; thus, to further increase the REE mass fraction, the liquid solid ratio is reduced by reducing the liquid flow rate and increasing the solid flow rate. Results show that the REE mass fraction can be increased to 0.12%, which is about six times the value of the base case.

#### 4.3.3 Scale-Up of the REE Leaching Reactor

Reactor scale-up is one of the most important tasks for chemical engineers and has been regarded as a major challenge in chemical reaction engineering due to the nonlinear properties of fluid flow, heat transfer, and chemical reactions for single-phase flow reactors. For multiphase flow reactors, however, one should add a little bit of witchcraft (Matsen, 1997 in Knowlton et al., 2005) to make any predictions because these complex reactors seem outside the realm of human understanding. Traditional experiment-based

**Table 14** Geometries of the Counter-Current Leaching Reactor at Different Scales

	<b>Small</b>	<b>Medium</b>	<b>Large</b>
Reactor diameter, $D_1$ (m)	0.08	0.16	0.80
Bottom outlet diameter, $D_2$ (m)	0.04	0.08	0.40
Height, $H_1$ (m)	0.04	0.08	0.16
Height, $H_2$ (m)	0.08	0.16	0.32
Height, $H_3$ (m)	0.10	0.20	0.40
Height, $H_4$ (m)	0.48	1.12	2.24
Height, $H_5$ (m)	0.64	1.28	2.56
Liquid flow rate, $L$ (kg/h)	72	28.8	7200
Solid flow rate, $S$ (kg/h)	18.41	73.64	1841
Solid inventory (kg)	0.409	3.273	163.644
Averaged residence time (s)	80	160	320
Particle diameter (mm)	0.45	0.6	1.2

approaches usually start from cold flow, which focuses on hydrodynamics, and the coupling between mass/heat transfer and hydrodynamics is often neglected. With the help of CFD, reactor scale-up can be accomplished very efficiently by coupling different phenomena, such as reactions, with hydrodynamics. In this part, the small-scale REE leaching reactor studied previously is scaled up in size using CFD–CGHS. The simulation setup is the same as that in [Section 4.3.1](#). The detailed geometries of the reactors at different scales are listed in [Table 14](#).

[Fig. 42](#) shows the snapshots of REE leaching reactors from small to large scales. It graphically compares the scales of the three simulated reactors. In simulation, the reactor is virtually scaled up by 2 and 4 times in the axial direction, and 2 and 10 times in the radial direction. Note that it was not necessary to scale up the reactor height 10 times because the target leaching rate was obtained in a shorter reactor. There is no analytical relationship between reactor size, particle diameter, and performance. For a specified particle diameter, we calculate the residence time in the reactor based on the nonlinear reaction kinetics. Then, based on this residence time, we know the “theoretical” height of the reactor because of a known terminal velocity calculated from the assumed drag law. The actual reactor height

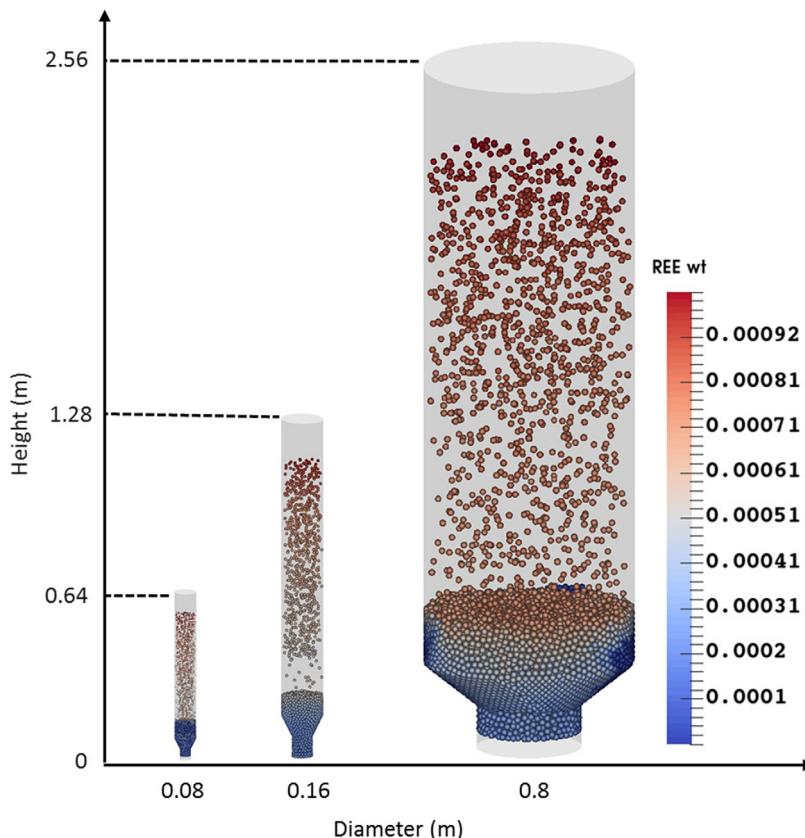


**Fig. 42** Snapshots of REE leaching reactor under different scales. Modified from Lu L, Benyahia S: Thousand-fold speedup of discrete-particle-based computer-aided reactor design and scale-up, Advanced Materials TechConnect Briefs (vol 1):363–366, 2017 with permission for the reprinted content. Copyright (2017) Nano Science and Technology Institute.

is lower because we can allow the particles to stay longer in the dense region of the bottom of the reactor. Postprocessing the simulation results show that the amount of calculated leached REE ions from small to medium to large reactors are 0.36, 1.45, 36.2 kg/day, respectively, based on a targeted 80% extraction efficiency. The distribution of particles shown in Fig. 42 indicates similarities in the particulate dynamics for the three scales of reactors, due to the flow homogeneity that is generally observed in liquid–solids fluidized beds.

From small scale to medium scale, the reactor dimension is doubled in all directions. Thus, the solid and liquid flow rate are increased four times.

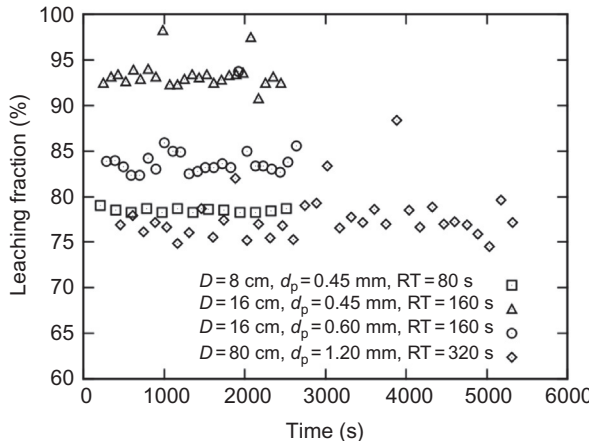
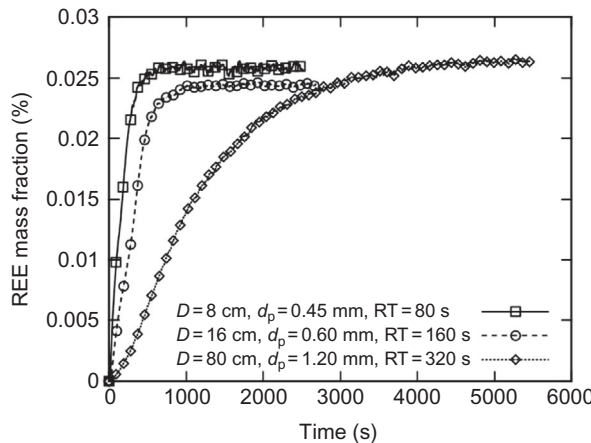


Fig. 43 REE leaching fraction with different scales and particle diameters.

To maintain the same nondimensional dense phase height, the space–time (or averaged residence time) is also doubled. This indicates a large increase in leaching fraction due to the doubled reaction time. As shown in Fig. 43, the leaching rate is increased from about 80% to 93%, which is higher than the targeted leaching fraction of around 80%. Some engineers may be pleased with this result since the performance is better than the target value. However, this outperformance relies on small particle size, which usually requires high energy consumption due to excessive grinding during preparation. Since the leaching reaction rate is directly related to particle size, a larger particle size is also tested. As shown in Fig. 43, for a medium-sized reactor, the particle size can be increased to 0.6 mm and, due to the longer residence time, the leaching fraction is still above 80%. For a large-scale reactor, the particle size is increased to 1.2 mm and the final leaching fraction is about 77%, which is still around the target value. From these simulation results, we can conclude that larger particles can be used for larger reactors. This is highly desirable because using larger particles is more economical due to the energy savings realized by minimized grinding of solid material.

Finally, the REE mass fractions in the top outlet liquid stream under different scales are compared in Fig. 44. A similar REE mass fraction is achieved at the outlet liquid stream at steady-state operation. The only difference among the different scales is the time required to reach this stable state. This is due to the different residence times achieved in the three different reactors. Nevertheless, similar steady operation of these reactors is achieved at the same performance level, even though the particle size increased with



**Fig. 44** REE mass fractions in the top outlet liquid stream under different scales.

increasing reactor size. Keeping the same particle diameter for all three reactors would increase the performances of the largest reactor, as previously mentioned.

As with some previous studies described in this chapter, one aspect of these REE simulations is the long simulation time achieved as indicated, for example, in Fig. 44 where thousands of simulation seconds were conducted in the large-scale reactor. The ability to conduct long simulations is something new with discrete particle models and is possible only because of the different assumptions of coarsening detailed in this study. Thus, we finally note in this chapter the ability of the CGHS technique to simulate large-scale reactors for longer time periods under different conditions, leading to scale-up and optimization analysis of multiphase flow reactors used in many industries, as shown in Sections 3 and 4.



## 5. CONCLUDING REMARKS AND PERSPECTIVES

This chapter provides a detailed description of a coarse discrete particle method with a time-driven hard sphere model developed here for the purpose of industrial-scale multiphase flow reactor simulations. The coarse particle flow dynamics, as well as details of heat transfer with the fluid and other particles/walls, was also provided along with several examples of heterogeneous chemical reactions and mass transfer with the fluid. A brief description of the coupling of this coarse particle method with the fluid and the CFD aspect was also provided in this chapter to give the reader a near-complete

picture of the modelling capabilities of the CFD–CGHS method, its development, and usability. The V&V aspect of this method was provided by simulating simplified systems (settling of granular material) and small-scale fluidized bed systems where experimental data and/or numerical data are published and available. The verification step relies heavily on comparison with numerical data obtained by using finer modelling approaches that do not make the coarsening assumptions adopted in this study. Meanwhile, the validation step relies on comparison of our simulation results with available experimental data, most of which are available in small- or laboratory-scale fluidized beds. We extend the validation studies by examining a few industrial-scale reactors where experimental data are also provided in the open literature. We finished this chapter by providing a case where the CFD–CGHS model was used to scale up an REE liquid extraction with process optimization to maximize the REE concentration in the outlet stream. Tackling these large-scale reactors serves a dual purpose of providing a sense of validity of the proposed approach as well as a sense of usefulness and applicability to a wide-range of chemical and energy industries, to name just a few. Thus, by writing this chapter, we hope to increase the usability of CFD methods and help extend their range of validity and also to pinpoint inherent limitations in these methods. It is also our hope that these limitations will encourage more CFD development by academia and industry to ultimately achieve better predictability at the lowest cost possible.

The limitations of CFD and its application to industrial-scale problems are associated with two aspects tackled in this chapter: the complexity of the models and the speed of execution. Extremely complex models are inherently difficult to use and discouraging to apply to practical case studies. Also, slow-to-execute computational models are only practical for small-scale studies and may be too costly to run on today's computers or even supercomputers for industrial-scale problems. For this purpose, we propose the use of simple models with simple to understand assumptions that can produce reasonably accurate results at a speed acceptable to most industrial practitioners. For this purpose, we demonstrated that simulating large-scale reactors can be achieved in just a few days of wall-clock time using minimal computer resources that most research groups possess. Also, because large-scale reactors are often associated with large residence time for particles, the ability to run simulations for thousands of seconds was demonstrated. The speed of the industrial-scale simulations conducted in this study proves the ability of this newly developed technique to tackle not only industrial-scale problems but also their optimization using a rigorous CFD approach.

instead of traditional chemical process software based on oversimplification of the complex flow dynamics in multiphase flow reactors. This provides the design engineer with an alternative tool to most process optimization software, which are traditionally based on simple heat and mass balances on oversimplified reactor models that usually ignore Newton's second law of motion, i.e., momentum conservation. That said, our intention is not to undermine the usefulness of process design and optimization tools that can simulate an entire plant instead of just a unit operation (fluidized bed) as proposed in this chapter. Given the current computational resources, we are still far from simulating the whole plant with the current CFD approach, therefore increasing simulation speed should be paramount to modelers and simulation tool developers. Increasing the MFIX computation speed to increase its fluid solver speed is a low hanging fruit. A simple simulation of a 3D single-phase jet flow with Re number of  $2.78 \times 10^4$  proves that the execution speed of the MFIX fluid flow solver is extremely slow. Hence Fig. 45 indicates that the speed of the MFIX fluid solver can be increased significantly by adopting different flow solving algorithms, such as PISO instead of SIMPLE (Barton, 1998; Chow and Cheung, 1997). The PISO algorithm is much faster than SIMPLE because it uses large underrelaxation factors and time steps. Other unpublished findings, the details of which are not provided here for brevity, show the increase in simulation speed due to the linear equation solver, from that used in MFIX to the algebraic multigrid solver used in a different CFD code. With these tweaks to the flow and linear equation solver, it will be possible to achieve much faster results that will appeal even more to industrial users. For example, previous simulation using OpenFOAM coupled with GPU-accelerated coarse-grained CFD-DEM can simulate a pilot-scale CFB riser at almost real-time in 2D (Ge et al., 2015; Lu et al., 2016c). With this speed, the user can make online adjustments to the operating parameters, like superficial gas velocity, and the corresponding hydrodynamics can be observed directly through the display program as shown in Fig. 46.

The most important remaining work not covered in this chapter (to be conducted soon) is a systematic study to determine the accuracy vs speed of the coarsening assumption. Basically, we want to answer the question of how much uncertainty do we introduce in our simulation by assuming a certain parcel size. We should note that this type of uncertainty is related to model assumptions and not input or discretization errors. We simply assume that CFD-DEM results are the most accurate and any deviation is due to model coarsening by adopting parcels instead of real particles. For this

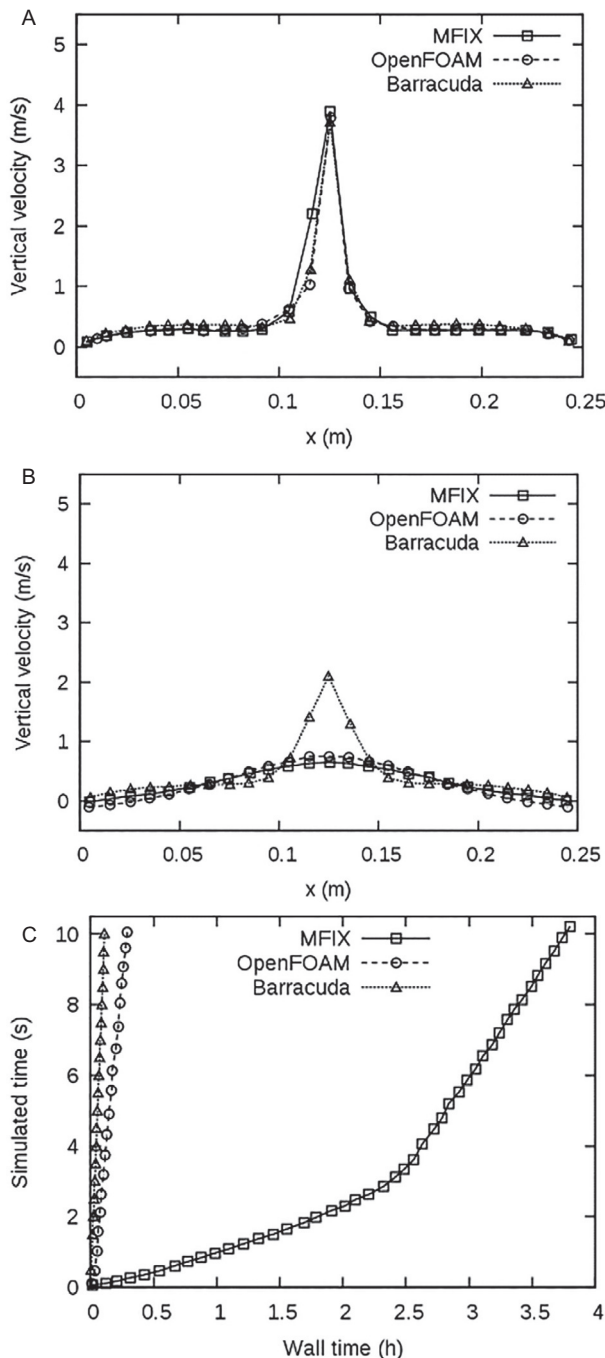


**Fig. 45** Single-phase jet flow simulation with a laminar (A) and turbulent (B) models simulated with three CFD codes along with their simulation time (C) conducted on the same single-processor.

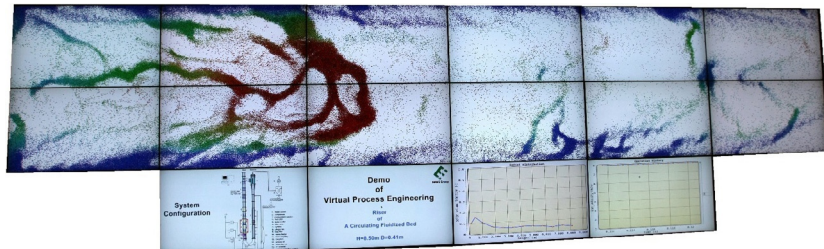


**Fig. 46** Interactive simulation of a pilot-scale CFB riser using OpenFOAM coupled with GPU-accelerated coarse-grained CFD-DEM (Ge et al., 2015; Lu et al., 2016c). Modified from a photograph of the computer virtual experiment at Institute of Process Engineering, Chinese Academy of Sciences.

purpose, we plan to study the effect of using different parcel sizes on different system geometries and flow rates. The different geometries will explore the effect of system size (or total number of particles) on the coarsening errors. The different flow rates will answer the basics question of quantifying this uncertainty for different flow regimes, such as bubbling, transport, etc. Answering these questions will give the simulation engineer an idea of what level of uncertainty is associated with a certain level of coarsening for his or her application. Apart from what was pursued in this chapter, another application will be pursued in the near future that relates to particles with changing properties, such as PSD, that has many applications in crystallization of a solute as well as polymerization reactors used in the pharmaceutical and chemical industry, respectively. The power of discrete particle methods is that the change of PSD or any other property of the particles is straightforward to code and apply as long as crystallization or polymerization growth rates are known *a priori* from other studies. Unlike the continuum model or TFM, discrete methods do not require the additional burden of modelling PSD changes through population balance equations. Unlike population balance equations, discrete methods provide continuous size and other property distributions. In addition, if binning the PSD is required for comparison with experimental data, then this will be just a straightforward postprocessing step. As mentioned earlier, the lack of additional model complexity is one of the most attractive aspects of discrete methods. Another important development effort that was not covered in this chapter but should be conducted in the future is the radiative heat transfer. Radiation is important for combustion and high temperature applications for many industries and will be investigated and implemented in the future.

Finally, we encourage readers to download the videos associated with this work because it is difficult to explain all the interesting results that were

obtained by simply looking at graphical representation of time-averaged results. We include several animations of our numerical results so that readers have the same experience as we did when looking at and analyzing these results. We also believe that good quality videos (from both simulation and experiments) are very useful educational tools that help students and practitioners understand the often opaque inside of their fluidized bed reactor. Supplementary data to this article can be found online at <https://doi.org/10.1016/bs.ache.2017.12.001>.

## ACKNOWLEDGMENTS

This research was supported in part by an appointment to the National Energy Technology Laboratory Research Participation Program, sponsored by the US Department of Energy and administered by the Oak Ridge Institute for Science and Education. The authors would like to thank the support from Multiphase Flow Science team at National Energy Technology Laboratory. The first author, L.L., would also like to thank Institute of Process Engineering, Chinese Academy of Sciences for supporting his PhD study which has been a major basis for this research.

## DISCLAIMER

This report was prepared as an account of work sponsored by an agency of the United States Government. Neither the United States Government nor any agency thereof, nor any of their employees, makes any warranty, express or implied, or assumes any legal liability or responsibility for the accuracy, completeness, or usefulness of any information, apparatus, product, or process disclosed, or represents that its use would not infringe privately owned rights. Reference herein to any specific commercial product, process, or service by trade name, trademark, manufacturer, or otherwise does not necessarily constitute or imply its endorsement, recommendation, or favoring by the United States Government or any agency thereof. The views and opinions of authors expressed herein do not necessarily state or reflect those of the United States Government or any agency thereof.

## REFERENCES

- Andrews MJ, O'Rourke PJ: The multiphase particle-in-cell (MP-PIC) method for dense particulate flows, *Int J Multiphase Flow* 22:379–402, 1996.
- Avidan AA, Shinnar R: Development of catalytic cracking technology. A lesson in chemical reactor design, *Ind Eng Chem Res* 29:931–942, 1990.
- Barton IE: Comparison of SIMPLE-and PISO-type algorithms for transient flows, *Int J Numer Methods Fluids* 26:459–483, 1998.
- Batchelor GK, Brien RW: Thermal or electrical conduction through a granular material, *Proc R Soc Lond A Math Phys Sci* 355:313, 1977.
- Beetstra R, van der Hoef MA, Kuipers JAM: Drag force of intermediate Reynolds number flow past mono- and bidisperse arrays of spheres, *AIChEJ* 53:489–501, 2007.
- Benyahia S, Galvin JE: Estimation of numerical errors related to some basic assumptions in discrete particle methods, *Ind Eng Chem Res* 49:10588–10605, 2010.
- Benyahia S, Syamlal M, O'Brien TJ: Extension of Hill–Koch–Ladd drag correlation over all ranges of Reynolds number and solids volume fraction, *Powder Technol* 162:166–174, 2006.

- Benyahia S, Syamlal M, O'Brien TJ: Study of the ability of multiphase continuum models to predict core-annulus flow, *AIChE J* 53:2549–2568, 2007.
- Buist KA, Seelen LJH, Deen NG, Padding JT, Kuipers JAM: On an efficient hybrid soft and hard sphere collision integration scheme for DEM, *Chem Eng Sci* 153:363–373, 2016.
- Chang J, Wang G, Lan X, Gao J, Zhang K: Computational investigation of a turbulent fluidized-bed FCC regenerator, *Ind Eng Chem Res* 52:4000–4010, 2013.
- Chow WK, Cheung YL: Comparison of the algorithms PISO and simpler for solving pressure-velocity linked equations in simulating compartmental fire, *Numer Heat Transf A Appl* 31:87–112, 1997.
- De Wilde J, Richards G, Benyahia S: Qualitative numerical study of simultaneous high-G-intensified gas–solids contact, separation and segregation in a bi-disperse rotating fluidized bed in a vortex chamber, *Adv Powder Technol* 27:1453–1463, 2016.
- Fogler HS: *Elements of chemical reaction engineering*, New Jersey, 2009, Prentice-Hall International.
- Gao J, Lan X, Fan Y, et al: CFD modeling and validation of the turbulent fluidized bed of FCC particles, *AIChE J* 55:1680–1694, 2009.
- Garg R, Galvin J, Li T, Pannala S: Documentation of open-source MFIX-DEM software for gas–solids flows, 2012a: From URL, [https://mfix.netl.doe.gov/download/mfix/mfix\\_current\\_documentation/dem\\_doc\\_2012-1.pdf](https://mfix.netl.doe.gov/download/mfix/mfix_current_documentation/dem_doc_2012-1.pdf), 2012a.
- Garg R, Galvin J, Li T, Pannala S: Open-source MFIX-DEM software for gas–solids flows: part I—verification studies, *Powder Technol* 220:122–137, 2012b.
- Garzó V, Duffy JW, Hrenya CM: Enskog theory for polydisperse granular mixtures. I. Navier-Stokes order transport, *Phys Rev E Stat Nonlin Soft Matter Phys* 76:031303, 2007.
- Ge W, Li J: Physical mapping of fluidization regimes—the EMMS approach, *Chem Eng Sci* 57:3993–4004, 2002.
- Ge W, Lu L, Liu S, Xu J, Chen F, Li J: Multiscale discrete supercomputing—a game changer for process simulation? *Chem Eng Technol* 38:575–584, 2015.
- Ge W, Wang L, Xu J, et al: Discrete simulation of granular and particle-fluid flows: from fundamental study to engineering application, *Rev Chem Eng* 33(6):551–623, 2017.
- Gidaspow D: *Multiphase flow and fluidization: continuum and kinetic theory descriptions*, 1994, Academic Press.
- Grace J, Sun G: Influence of particle size distribution on the performance of fluidized bed reactors, *Can J Chem Eng* 69:1126–1134, 1991.
- Grace JR, Taghipour F: Verification and validation of CFD models and dynamic similarity for fluidized beds, *Powder Technol* 139:99–110, 2004.
- Gunn DJ: Transfer of heat or mass to particles in fixed and fluidised beds, *Int J Heat Mass Transf* 21:467–476, 1978.
- Helland E, Occelli R, Tadrist L: Numerical study of cluster and particle rebound effects in a circulating fluidised bed, *Chem Eng Sci* 60:27–40, 2005.
- Hoomans BPB, Kuipers JAM, Briels WJ, van Swaaij WPM: Discrete particle simulation of bubble and slug formation in a two-dimensional gas-fluidised bed: a hard-sphere approach, *Chem Eng Sci* 51:99–118, 1996.
- Igci Y, Andrews AT, Sundaresan S, Pannala S, O'Brien T: Filtered two-fluid models for fluidized gas-particle suspensions, *AIChE J* 54:1431–1448, 2008.
- Jackson R: *The dynamics of fluidized particles*, 2000, Cambridge University Press.
- Jun T, Jingqun Y, Ruan C, Guohua R, Mintao J, Kexian O: Kinetics on leaching rare earth from the weathered crust elution-deposited rare earth ores with ammonium sulfate solution, *Hydrometallurgy* 101:166–170, 2010.
- Kirbas G, Kim SW, Bi X, Lim J, Grace JR: In Berruti F, Bi X, Pugsley T, editors: *Radial distribution of local concentration weighted particle velocities in high density circulating fluidized beds*, 12th International conference on fluidization, 2007, pp 71–78.

- Knowlton T, Karri S, Issangya A: Scale-up of fluidized-bed hydrodynamics, *Powder Technol* 150:72–77, 2005.
- Kunii D, Levenspiel O: *Fluidization engineering*, Newton, MA, 1991, Butterworth-Heinemann.
- Kwauk M: *Fluidized leaching and washing*, (in chinese), Beijing, 1979, Science Press.
- Kwauk M: *Fluidization—idealized and bubbleless, with applications*, New York, 1992, Ellis Horwood.
- Li J, Kwauk M: *Particle-fluid two-phase flow: the energy-minimization multi-scale method*, Beijing, 1994, Metallurgical Industry Press.
- Li T, Dietiker J-F, Shahnam M: MFIX simulation of NETL/PSRI challenge problem of circulating fluidized bed, *Chem Eng Sci* 84:746–760, 2012a.
- Li T, Garg R, Galvin J, Pannala S: Open-source MFIX-DEM software for gas–solids flows: part II—validation studies, *Powder Technol* 220:138–150, 2012b.
- Li T, Dietiker J-F, Shadle L: Comparison of full-loop and riser-only simulations for a pilot-scale circulating fluidized bed riser, *Chem Eng Sci* 120:10–21, 2014.
- Lu C, Wang Z: *Fluid catalytic cracking technology*, Beijing, 2002, China Petrochemical Press.
- Lu L, Xu J, Ge W, Yue Y, Liu X, Li J: EMMS-based discrete particle method (EMMS-DPM) for simulation of gas–solid flows, *Chem Eng Sci* 120:67–87, 2014.
- Lu L, Yoo K, Benyahia S: Coarse-grained-particle method for simulation of liquid–solids reacting flows, *Ind Eng Chem Res* 55:10477–10491, 2016a.
- Lu B, Luo H, Li H, et al: Speeding up the modeling of MTO fluidized bed reactor with integration of CRE and CFD, *Chem Eng Sci* 143:341–350, 2016b.
- Lu L, Xu J, Ge W, et al: Computer virtual experiment on fluidized beds using a coarse-grained discrete particle method—EMMS-DPM, *Chem Eng Sci* 155:314–337, 2016c.
- Lu L, Gopalan B, Benyahia S: Assessment of different discrete particle methods ability to predict gas–particle flow in a small-scale fluidized bed, *Ind Eng Chem Res* 2017(56):7865–7876, 2017a.
- Lu L, Konan A, Benyahia S: Influence of grid resolution, parcel size and drag models on bubbling fluidized bed simulation, *Chem Eng J* 326:627–639, 2017b.
- Lu L, Morris A, Li T, Benyahia S: Extension of a coarse grained particle method to simulate heat transfer in fluidized beds, *Int J Heat Mass Transf* 111:723–735, 2017c.
- Lu L, Li T, Benyahia S: An efficient and reliable predictive method for fluidized bed simulation, *AIChE J* 63:5320–5334, 2017d. <https://doi.org/10.1002/aic.15832>.
- Lu L, Gao X, Li T, Benyahia S: Numerical investigation of the ability of salt tracers to represent the residence time distribution of fluidized catalytic cracking particles, *Ind Eng Chem Res* 56:13642–13653, 2017e.
- Merrow EW, Phillips KE, Myers CW: *Understanding cost growth and performance shortfalls in pioneer process plants*, Santa Monica, CA, 1981, Rand Corp.
- Moldoveanu GA, Papangelakis VG: An overview of rare-earth recovery by ion-exchange leaching from ion-adsorption clays of various origins, *Mineral Mag* 80:63, 2016.
- Ouyang J, Li J: Particle-motion-resolved discrete model for simulating gas–solid fluidization, *Chem Eng Sci* 54:2077–2083, 1999.
- Patankar NA, Joseph DD: Modeling and numerical simulation of particulate flows by the Eulerian–Lagrangian approach, *Int J Multiphase Flow* 27:1659–1684, 2001.
- Patil AV, Peters EAJF, Kuipers JAM: Comparison of CFD–DEM heat transfer simulations with infrared/visual measurements, *Chem Eng J* 277:388–401, 2015.
- Radl S, Sundaresan S: A drag model for filtered Euler–Lagrange simulations of clustered gas–particle suspensions, *Chem Eng Sci* 117:416–425, 2014.
- Radl S, Radeke C, Khinast JG, Sundaresan S: In *Parcel-based approach for the simulation of gas-particle flows*, 8th International conference on CFD in oil & gas. Trondheim, 2011, Metallurgical and Process Industries.

- Richard P, Nicodemi M, Delannay R, Ribiere P, Bideau D: Slow relaxation and compaction of granular systems, *Nat Mater* 4:121–128, 2005.
- Rong D, Horio M: In DEM simulation of char combustion in a fluidized bed, Second International conference on CFD in the minerals and process industries. Melbourne, Australia, 1999, CSIRO, pp 65–70.
- Sakai M, Koshizuka S: Large-scale discrete element modeling in pneumatic conveying, *Chem Eng Sci* 64:533–539, 2009.
- Sakano M, Yaso T, Nakanishi H: Numerical simulation of two-dimensional fluidized bed using discrete element method with imaginary sphere model, *Jpn J Multiphase Flow* 14:66–73, 2000.
- Shaffer F, Gopalan B, Breault RW, et al: High speed imaging of particle flow fields in CFB risers, *Powder Technol* 242:86–99, 2013.
- Shi Z, Wang W, Li J: A bubble-based EMMS model for gas–solid bubbling fluidization, *Chem Eng Sci* 66:5541–5555, 2011.
- Syamlal M, Benyahia S: High-resolution methods for preserving the sum of mass fractions: improved  $\chi$ -scheme and an alternative, *Int J Numer Methods Fluids* 73:750–764, 2013.
- Syamlal M, O'Brien T: *Derivation of a drag coefficient from velocity-voidage correlation*, Morgantown, West Virginia, 1987, US Department of Energy, Office of Fossil Energy, National Energy Technology Laboratory. April.
- Tang Y, Lau YM, Deen NG, Peters EAJF, Kuipers JAM: Direct numerical simulations and experiments of a pseudo-2D gas-fluidized bed, *Chem Eng Sci* 143:166–180, 2016.
- Tebianian S, Dubrawski K, Ellis N, et al: Comparison of particle velocity measurement techniques in a fluidized bed operating in the square-nosed slugging flow regime, *Powder Technol* 296:45–52, 2016.
- Thakur SC, Ooi JY, Ahmadian H: Scaling of discrete element model parameters for cohesionless and cohesive solid, *Powder Technol* 293:130–137, 2016.
- Tian P, Wei Y, Ye M, Liu Z: Methanol to olefins (MTO): from fundamentals to commercialization, *ACS Catal* 5:1922–1938, 2015.
- Tsuji Y, Kawaguchi T, Tanaka T: Discrete particle simulation of two-dimensional fluidized bed, *Powder Technol* 77:79–87, 1993.
- Wang W, Li J: Simulation of gas–solid two-phase flow by a multi-scale CFD approach—of the EMMS model to the sub-grid level, *Chem Eng Sci* 62:208–231, 2007.
- Wang J, Ge W, Li J: Eulerian simulation of heterogeneous gas–solid flows in CFB risers: EMMS-based sub-grid scale model with a revised cluster description, *Chem Eng Sci* 63:1553–1571, 2008.
- Wen CY, Yu YH: In *Mechanics of fluidization*, Chemical engineering progress symposium. 1966, pp 100–113.
- Xiao Y, Chen Y, Feng Z, et al: Leaching characteristics of ion-adsorption type rare earths ore with magnesium sulfate, *Trans Nonferrous Met Soc Chin* 25:3784–3790, 2015.
- Xu BH, Yu AB: Numerical simulation of the gas–solid flow in a fluidized bed by combining discrete particle method with computational fluid dynamics, *Chem Eng Sci* 52:2785–2809, 1997.
- Xu J, Qi HB, Fang XJ, et al: Quasi-real-time simulation of rotating drum using discrete element method with parallel GPU computing, *Particuology* 9:446–450, 2011.
- Yang N, Wang W, Ge W, Li J: CFD simulation of concurrent-up gas–solid flow in circulating fluidized beds with structure-dependent drag coefficient, *Chem Eng J* 96:71–80, 2003.
- Zhou ZY, Yu AB, Zulli P: Particle scale study of heat transfer in packed and bubbling fluidized beds, *AIChE J* 55:868–884, 2009.
- Zhou ZY, Yu AB, Zulli P: A new computational method for studying heat transfer in fluid bed reactors, *Powder Technol* 197:102–110, 2010.